Effects of Interfaces on Properties of Cladding Materials for Advanced Nuclear Reactors

by

Xing Wang

A dissertation submitted in partial fulfillment of
the requirement of the degree of

Doctor of Philosophy
(Nuclear Engineering and Engineering Physics)

at the
UNIVERSITY OF WISCONSIN-MADISON
2016

Date of final oral examination: August 16, 2016
The dissertation is approved by the following members of the Final Oral Committee:

Izabela A Szlufarska,	**Professor,**	**Materials Science and Engineering Physics**
Paul Voyles,	**Professor,**	**Materials Science**
Dane Morgan,	**Professor,**	**Materials Science and Engineering Physics**
John Perepezko,	**Professor,**	**Materials Science**
Kumar Sridharan,	**Professor,**	**Engineering Physics and Materials Science**

Abstract

A diverse energy portfolio is essential for the stability, affordability and security of energy supply. As the largest carbon emission-free electricity source (>70% in 2015), nuclear power will keep playing an important role in meeting the energy demand of future generations. Fuel cladding is the reactor's primary safety barrier, which prevents the radioactive fission fragments from escaping the fuel into the coolant. The development of advanced nuclear reactors requires fundamental improvement in the properties of cladding materials, which include increased strength at higher temperature, as well as superior corrosion and radiation damage resistance. Many of the above properties are controlled by interfaces. For instance, internal interfaces (e.g. grain boundaries and stacking faults) can act as defect sinks and external interfaces (e.g. surface of metal and oxide) are the places where oxidation and corrosion take place. It is therefore critical to understand the complicated effects of interfaces on these properties in order to design advanced fuel claddings.

This thesis focuses on two kinds of cladding materials, silicon carbide (SiC) and zirconium (Zr). SiC is a promising structure material for Generation IV nuclear reactors. Advanced transmission electron microscopy and multiscale materials simulations have been combined to investigate the defects-grain boundaries interactions in SiC. At low irradiation temperature, the accumulated defect concentration with increasing dose can lead to lattice distortion and finally cause the crystalline-to-amorphous transition. High-resolution transmission electron microscopy (HRETM) reveals a novel feature of highly curved boundaries between amorphous phase and crystalline phase. Based on this feature and our coarse-grained morphology modeling, cascade overlap has been demonstrated as the governing mechanism of radiation-induced amorphization for heavy ion (e.g. Kr^+) irradiation, which is different from the

mechanisms for electron and neutron irradiation. It is suggested that the effects of microstructures of SiC on the amorphization process are coupled with the different amorphization mechanisms of different irradiation species, which can help explain the experimental findings that grain refinement leads to either improved or decreased resistance to radiation-induced amorphization of SiC. HRTEM analyses also show the amorphization rate near grain boundaries is accelerated when compared to grain interiors. Combined with *ab initio*-informed rate theory calculations, the presence of the interstitial starvation mechanism near grain boundaries has been demonstrated for the first time. As a competing effect to defect sinks, interstitial starvation leads to vacancies built up near defect sinks and reduces the radiation resistance of nanocrystalline SiC. At high irradiation temperature, defect diffusion and reaction are fast enough so irradiation can no longer lead to amorphization in SiC. However, the unbalanced flux of composition elements to defect sinks may lead to radiation-induced segregation (RIS) near interfaces like grain boundary. Using scanning transmission electron microscopy (STEM) and electron energy loss spectroscopy (EELS), the RIS in SiC under different irradiation temperature has been investigated. We have not only found the grain boundaries in chemical vapor deposited SiC are intrinsically C depleted, but also discovered that the irradiation can substantially decrease C concentration at grain boundaries at elevated temperature. The C-depleted grain boundaries may substantially affect the materials' resistance to corrosion and radiation damage. In addition, grain boundaries can act as diffusion channels for radioactive fission products (e.g. Ag), so RIS may also affect the diffusion process of the fission products. Since the final C concentration profile near grain boundary is a result of various synergetic processes (including defect reaction and migration) taking place both in grain interiors

and at grain boundaries, characterizing RIS will provide an efficient benchmark to test the current knowledge on defect kinetics in SiC.

Zr alloys are the most widely used cladding materials in current water-cooled reactors. Density functional theory calculations have been applied to discover the effects of surface strain on the oxidation process. The interplay between surface strain and interaction between oxygen adsorbates determines the relative stabilities of different binding sites. The binding energy calculations indicate that the compressive strain at the Zr/oxide interface provides a thermodynamic driving force for oxygen diffusing into deeper Zr layers while the tensile strain facilitates the process of binding oxygen to Zr surface. A continuum model that predicts the time-dependent hydrogen pickup fractions has also been developed in this thesis. Using only one fitting parameter, the hydrogen gas partial pressure at the oxide surface, a very good agreement is obtained between the predicted and previously measured hydrogen pickup fractions. The calculation results support the hypothesis that hydrogen diffusion through the dense oxide layer is the rate-limiting step for hydrogen pickup. The limitations and possible improvement of current model are also discussed.

Table of Contents

Acknowledgements

I would like to express my sincere appreciation to my advisor Professor Izabela Szlufarska. This thesis could not be completed without her tremendous encouragement, brilliant guidance and incredible patience. Her enthusiasm in science inspires me to go deep into the questions and her acute awareness of science leads me to go through the puzzles. She always gives the full support to students to pursue their curiosity in different research topics and other deserved fields, which I think is critical to the success of the students in their long term career development. She sets an example to me on how to be a good advisor.

I am also grateful to my co-advisor Professor Paul Voyles, who introduced me to the field of transmission electron microscopy and gave me innumerable helpful suggestions. Whenever I faced a technical challenge, he always encouraged me to think from the positive side. I benefited a lot from this way of optimistic thinking, which is actually also the first step to solve various challenges in one's life.

I want to thank Professor Dane Morgan, who served as co-PI or PI for most of my research projects. His insightful feedback helped me keep the big pictures in mind and focus on the really challenging and meaningful questions. I want to thank Professor Kumar Sridharan for all the helpful discussions during our BES meetings. My acknowledgement also goes to Professor John Perepezko, who taught me the course *advanced materials phase transformation*. The course is very difficult but also extremely helpful to my research. I would like to acknowledge all my committee members for taking time out of their busy schedules to serve my dissertation committee.

I would like to thank all the former and current members of the Computational Materials Group and Electron Microscopy group. I feel so lucky to get the chance to work with so many talented, diligent and cooperative colleagues.

List of Figures

List of Tables

List of Terminology

APT	Atom probe tomography
ATF	Accident-tolerant fuel
CNT	Carbon nano tube
CVD	Chemical vapor deposition
DFT	Density functional theory
EDS	Energy dispersive X-ray spectroscopy
EELS	Electron energy loss spectroscopy
GB	Grain boundary
GGA	Generalized gradient approximation
HRTEM	High-resolution transmission electron microscopy
LDA	Local density approximation
LPCVD	Low pressure chemical vapor deposition
MD	Molecular dynamics
RIA	Radiation-induced amorphization
RIS	Radiation-induced segregation
SADP	Selected area diffraction pattern
SD	Standard deviation
SiC	Silicon Carbide
SRIM	Stopping power and range of ions in matters
STEM	Scanning transmission electron microscopy
TEM	Transmission electron microscopy
VASP	Vienna *Ab Initio* Simulation Package

1. Introduction and motivation

1.1 Challenge to cladding materials for advanced nuclear energy system

Cladding of nuclear fuel is the outer layer of the fuel rods, separating the coolant and fuel materials (e.g. uranium oxide). The fission reaction of uranium atoms produces radioactive fragments that emit neutrons, γ rays, α and β partials and can be harmful to human health. Therefore fuel cladding is the reactor's primary safety barrier, which prevents the fission fragments from escaping the fuel into the coolant [1–3]. The safe operation of nuclear energy systems is strongly dependent on the performance of cladding materials, which are exposed to exceptionally harsh environment due to the combination of intense radiation damage, corrosive coolant, long service time, high temperature and pressure [1].

The major degradation mechanisms of cladding materials can be divided into two categories, i.e. radiation-induced degradation and corrosion-induced degradation. Radiation-induced degradation in material properties originates from neutron-atom elastic collisions that generate displacement cascades and the following microstructure defects, such as vacancies clusters, interstitial type dislocation loops and second phase precipitates [4]. These defects might produce changes in the mechanical, chemical and physical properties of cladding materials. At low temperature (below 0.4 of melting temperature), the defect clusters can act as obstacles to dislocation motion, leading to radiation hardening and reducing the ductility [4,5]. For some covalent materials, the accumulated defect concentration with increasing dose can also lead to lattice distortion and finally the crystalline-to-amorphous transition [6–8]. Amorphization can substantially decrease the hardness, strength, as well thermal conductivity of the material [6,9,10]. At the intermediate temperature (0.4-0.6 of melting temperature), due to the different diffusivities of interstitials and vacancies of the constitution elements, an net defect flux moves

towards defect sinks and change the local chemistry in regions near surface, grain boundaries, dislocations and phase boundaries. This phenomenon is called radiation-induced segregation (RIS) [11]. RIS can lead to localized degradation of corrosion or mechanical properties, such as grain boundary embrittlement [12,13]. Additionally, at the same temperature range, void swelling from vacancy accumulation can create undesirable volumetric expansion, while radiation-induced creep and growth can produce dimensional expansion along directions of high stress or specific crystallographic directions [14]. Radiation also enhances creep in metals as irradiation-produced vacancies provide the means of dislocation climb around stable precipitates [15]. Generally speaking, radiation-induced embrittlement defines the constraint for minimum service temperature of cladding materials, while thermal creep defines the constraint for maximum service temperature.

Corrosion is usually defined as the chemical or electrical reactions between a material with its environment that convert the material into a more stable form such as oxide and hydroxide. Although supposedly highly corrosion-resistant alloys have been used, such as nickel based alloys, stainless steels and zirconium (Zr) alloys, nuclear power plant have suffered various failures through corrosion since the 1970s [16]. For example, by picking up oxygen from the reactor water, Zr alloys can oxide to form zirconia, which causes the clad thinning as the zirconia peels off and eventually the clad rupture [17]. During the oxidation process, hydrogen from the water and Zr corrosion reactions can permeate through the protective oxide layers, diffuses and accumulates in Zr metal, potentially reaching or surpassing the hydrogen solubility limit of the Zr alloy [18]. This process is called hydrogen pickup and it can lead to the formation of brittle hydrides that can significantly reduce the ductility of Zr alloys [19,18]. Typically corrosion is an issue for metal components in the nuclear plant. However, recent study suggests

that silicon carbide (SiC), as a promising ceramic cladding material, also suffers from serious oxidation problem in 360 degree C supercritical water[20], although some other studies show contradictory results [21,22]. According to ref [20], the grain boundaries of the SiC dissolved preferentially during the early stage of corrosion and the grains became thinner and detached from the surface, thereby leading to an acceleration of the weight loss. To design corrosion-resistant cladding materials, it is important to get a thorough understanding of the detailed corrosion mechanisms and also develop models that can predict the corrosion behaviors within acceptable accuracy.

The extreme condition in the nuclear reactor core sets high standards for selecting cladding materials. Obviously the cladding materials should be resistant to radiation damage and corrosion. In addition, the cladding materials should be transparent to neutron in order to minimize the neutron loss. They should also present an acceptable service temperature, as well as high thermal conductivities in order to increase the thermal efficiency of the reactor. The cost and availability of the materials play important roles in determining the economics of the fuel rod. A balance of all these factors will yield the optimum cladding performance [3]. The unique properties of Zr (low neutron absorption cross-section, good mechanical properties, high service temperature and corrosion and radiation resistance) make it an ideal cladding material [23]. By mid of 1960s, Zr alloys were already the main fuel cladding materials in both light water and heavy water reactors [3]. However, the development of Generation IV nuclear reactors creates even more extreme conditions for in-core structural materials, since the operation temperature is expected to increase to 1000 °C and the radiation damage can be as large as 150 dpa (displacement per atom) [1]. As a comparison, the highest cladding temperature in current light water reactor is about 360 °C and the maximum dose for cladding is 70 dpa. More chemically

aggressive coolants, such as molten salt and sodium will be applied in these advanced nuclear energy systems. Therefore Zr alloys are no longer appropriate cladding materials. In addition, under several accident scenarios, such as the station blackout events in Fukushima Daichi power plant and lost-of-coolant accident, the decay heat quickly drives the fuel temperature upward. The increase in temperature causes the Zr alloy cladding to burst at 700 – 1100 °C and produce hydrogen rapidly [22]. To provide larger safety margins for current light water reactors, recently there are campaigns worldwide to seek designs of accident tolerant fuel (ATF). High-performance stainless steels (FeCrAl), SiC composite, refractory alloys and Zr alloy with coatings are promising candidate for advanced claddings [24]. Among all the choices, SiC stands out due to its low thermal neutron absorption cross-section, chemical inertness and good oxidation resistance in air and steam up to temperatures of at least 1600 °C [6].

1.2 Interface engineering for cladding material design

Development of advanced nuclear systems requires fundamental improvements in the properties of cladding materials, which include increased strength at higher temperature, as well as superior corrosion and radiation damage resistance. Many of the above properties are controlled by interfaces. For instance, internal interfaces (e.g., grain boundaries and stacking faults) can act as defect sinks and external interfaces (e.g., surfaces of metals/oxides and interface boundary) are the places where oxidation and corrosion take place. By introducing interphase boundaries, tuning grain sizes or adding surface coatings, a number of encouraging results on properties improvement in nuclear materials have been reported. For example, So et al. fabricated Al composite with homogeneously distributed carbon nanotubes (CNTs) by spark plasma sintering and hot extrusion. Compare to Al, this composite shows improved tensile strength without reduction of tensile ductility, and reduced pore generation and radiation

embrittlement after irradiation to 72 dpa [25]. Similarly, by synthesizing bulk nano-layered Cu-Nb composites containing interfaces with controlled sink efficiencies, Han et al. designed the material which shows nearly void free after irradiation while pure Cu nanocrystalline films irradiated at the same condition have obvious large voids [26]. The nano-layered composite also maintains the ultrahigh hardness (4.13 ± 0.4 GPa), tensile strength (1 GPa) and excellent thermal stability as its single component counterpart. For ceramic claddings, nanocrystalline SiC has shown not only increased strength, but also higher dose to amorphization than single crystalline SiC under electron irradiations [27]. To decrease the diffusion of radioactive trace elements, TiN thin files were coated on HT9 steel claddings. Transmission electron microscope (TEM) analysis of Ce/TiN/HT9 samples annealed at 600 degree C for 12 hours showed no Ce diffusing into the TiN layer, indicating the coating is an effective barrier to fuel-cladding interactions [28].

The success of applying interface engineering to materials design relies on thorough understandings of mechanisms of defect-interface interactions and subsequent complex degradation processes. Arbitrarily adding or modifying interfaces may not necessarily lead to improved properties. For example, as shown in ref. [26], the radiation resistance of nano-layered Ni-Cu are optimized when the number of Cu{112}<110>//Nb{112}<111> interface is maximized, because atomistic simulations show that this type of interface has the lowest interfacial energy than the other interfaces. Another example is that the same nanocrystalline SiC showed worse radiation resistance under heave ion irradiation [29] but increased resistance under electron irradiation. The seemingly contradictory results were proven to be due to the coupling effects between microstructures and different amorphization mechanisms of different irradiation species [8].

Understanding the complex mechanism for defect-interface interaction and the following material degradation is challenging as it often contain synergetic processes at quite different time scales and length scales. The combination of high resolution (scanning) transmission electron microscopy ((S)TEM) analysis and multiscale simulations provide a unique approach to address these challenges. On the experimental side, with the development of aberration-corrected STEM and advanced post processing algorithms, the image spatial resolution can reach sub-Angstrom and the precision can reach sub-picometer [30]. This unprecedented resolution and precision make it possible to directly compare defect features generated from experimental observations with atomistic simulations. On the simulation side, the innovations in simulation techniques enable us to model complicated materials processes involving collective phenomena that occur over a wide range of time and length scales [31]. The cross validation between the advanced microscopy and multiscale simulations would be an invaluable tool to understand the defect-interface interactions starting from atomic level. The knowledge gained from this validation can then provide accurate and reliable parameters for mesoscale and microscale simulations, which deal with time scale up to seconds or days and length scale up to meters.

1.3 Thesis overview

This thesis aims at combining advanced (S)TEM analysis with multiscale simulations to investigate the interactions between defect and interfaces in nuclear cladding materials. Chapter 2 and 3 are focusing on SiC. In chapter 3, the radiation-induced amorphization (RIA) under heavy ion irradiation and the effect of grain boundaries (GB) during the RIA were investigated. Based on high resolution TEM images and *ab initio* informed rate theory calculations, the presence of interstitial starvation phenomenon was demonstrated experimentally for the first time. The highly curved crystalline/amorphous boundaries also provided evidence that supports the

cascade overlap as the dominant amorphization mechanism. In chapter 4, using STEM/EELS with ultra-high spatial resolution and stability, we were able to characterize the composition changes near GB in SiC irradiated at various temperature. The results showed that C firstly segregated to GB at low temperature but then became depleted at GB at high temperature due to the activated C interstitial diffusion along GB to stronger sinks like surfaces. It is the first time that RIS of constitution elements is found in ceramic materials. The temperature-depended trend of RIS was also explained by our rate-theory calculations.

Chapter 4 and 5 focus on Zr and Zr alloys. In chapter 5, density functional theory (DFT) was applied to study the stain effects on the oxygen adsorption on Zr surface. The calculation revealed the competing effects between surface strain and adsorbate repulsive interactions on determining the relative stability of different binding sites. Chapter 6 developed a continuum model that predicted the time dependent H pickup ration for various Zr alloys. Although only simple diffusion process of H through water/oxide/metal interfaces were solved in the model, a very good agreement between simulation and experiment results were obtained.

Finally possible future research directions are briefly introduced in chapter 6.

Bibliography

[1]   S.J. Zinkle, G.S. Was, Acta Mater. 61 (2013) 735.

[2]   T. Allen, J. Busby, M. Meyer, D. Petti, Mater. Today 13 (2010) 14.

[3]   C.R.F. Azevedo, Eng. Fail. Anal. 18 (2011) 1943.

[4]   G.S. Was, Fundamentals of Radiation Materials Science: Metals and Alloys, Springer, New York, 2007.

[5]   K. Farrell, R.T. King, Metall. Trans. 4 (1973) 1223.

[6]   L.L. Snead, T. Nozawa, Y. Katoh, T.-S. Byun, S. Kondo, D.A. Petti, J. Nucl. Mater. 371 (2007) 329.

[7]   Y. Katoh, L.L. Snead, I. Szlufarska, W.J. Weber, Curr. Opin. Solid State Mater. Sci. 16 (2012) 143.

[8]   X. Wang, L. Jamison, K. Sridharan, D. Morgan, P.M. Voyles, I. Szlufarska, Acta Mater. 99 (2015) 7.

[9]   J. Cabrero, F. Audubert, R. Pailler, A. Kusiak, J.L. Battaglia, P. Weisbecker, J. Nucl. Mater. 396 (2010) 202.

[10] M. Ishimaru, I.-T. Bae, A. Hirata, Y. Hirotsu, J.A. Valdez, K.E. Sickafus, Phys. Rev. B 72 (2005) 024116.

[11] H. Wiedersich, P.R. Okamoto, N.Q. Lam, J. Nucl. Mater. 83 (1979) 98.

[12] N. Sakaguchi, S. Watanabe, H. Takahashi, R.. Faulkner, J. Nucl. Mater. 329-333 (2004) 1166.

[13] S. Watanabe, J. Satou, N. Sakaguchi, H. Takahashi, C. Namba, J. Nucl. Mater. 239 (1996) 200.

[14] S.J. Zinkle, J.T. Busby, Mater. Today 12 (2009) 12.

[15] D.R. Olander, Naturwissenschaften 67 (1980) 61.

[16] F. Cattant, D. Crusset, D. Féron, Mater. Today 11 (2008) 32.

[17] B. Cox, J. Nucl. Mater. 336 (2005) 331.

[18] K. Videm, Nucl. Eng. Des. 21 (1972) 200.

[19] A.T. Motta, L.Q. Chen, Jom 64 (2012) 1403.

[20] J.Y. Park, I.H. Kim, Y. Il Jung, H.G. Kim, D.J. Park, W.J. Kim, J. Nucl. Mater. 443 (2013) 603.

[21] T. Allen, M. Lance, H. Meyer, L. Walker, 318 (2007) 315.

[22] B.A. Pint, K.A. Terrani, M.P. Brady, T. Cheng, J.R. Keiser, J. Nucl. Mater. 440 (2013) 420.

[23] B. Cox, Adv. Corros. Sci. Technol. (1976) 173.

[24] S.J. Zinkle, K.A. Terrani, J.C. Gehin, L.J. Ott, L.L. Snead, J. Nucl. Mater. 448 (2014) 374.

[25] K.P. So, D. Chen, A. Kushima, M. Li, S. Kim, Y. Yang, Z. Wang, J.G. Park, Y.H. Lee, R.I. Gonzalez, M. Kiwi, E.M. Bringa, S. Lin, J. Li, Nano Energy (2016) 319.

[26] W. Han, M.J. Demkowicz, N.A. Mara, E. Fu, S. Sinha, A.D. Rollett, Y. Wang, J.S. Carpenter, I.J. Beyerlein, A. Misra, Adv. Mater. 25 (2013) 6975.

[27] Y. Zhang, M. Ishimaru, T. Varga, T. Oda, C. Hardiman, H. Xue, Y. Katoh, S. Shannon, W.J. Weber, Phys. Chem. Chem. Phys. 14 (2012) 13429.

[28] I. Kim, F. Khatkhatay, L. Jiao, G. Swadener, J.I. Cole, J. Gan, H. Wang, J. Nucl. Mater. 429 (2012) 143.

[29] L. Jamison, K. Sridharan, S. Shannon, I. Szlufarska, J. Mater. Res. 29 (2014) 2871.

[30] A.B. Yankovich, B. Berkels, W. Dahmen, P. Binev, S.I. Sanchez, S.A. Bradley, A. Li, I. Szlufarska, P.M. Voyles, Nat. Commun. 5 (2014) 4155.

[31]   S. Yip, M.P. Short, Nat. Mater. 12 (2013) 774.

2. Radiation-induced amorphization in silicon carbide and the effects of grain boundary

2.1 Background and motivation

Silicon carbide (SiC) has attracted considerable attention in the nuclear industry because of its outstanding properties, such as high-temperature stability, chemical inertness, high thermal conductivity and low neutron absorption cross-section [1]. In order to meet the reliability requirements during long-term service in a nuclear reactor, a material must be highly resistant to radiation damage. This is because radiation creates numerous point defects and defect clusters that accumulate and lead to the degradation of the material properties [2]. One of the responses of SiC to irradiation is radiation-induced amorphization (RIA) [3]. RIA reduces the hardness, elastic modulus and thermal conductivity of SiC and is accompanied by swelling of the material [4-6].

The mechanism for RIA in SiC has been extensively studied by both experimental and theoretical approaches [7-13]. Amorphization can proceed either homogeneously or heterogeneously [3]. In homogeneous amorphization, point defects accumulate progressively in the system until crystalline order is lost. This process is sometimes modeled as involving point defects raising the energy of the system until a critical energy density is reached, at which point the system transforms to a more stable amorphous state spontaneously [14]. For heterogeneous amorphization, several possible mechanisms have been proposed, including cascade overlap, direct impact/defect stimulated growth (DI/DS) at crystalline/amorphous (c/a) boundaries and a nucleation and growth model. The cascade overlap model assumes that irradiation produces regions of high defect concentration, i.e., displacement cascades, and the overlap of these cascades leads to localized amorphization. In contrast, in the DI/DS model, local disordered regions are formed directly by the incident particles and further growth at c/a interfaces is

stimulated by the diffusion of generated defects. The amorphous phase may also nucleate and grow near extended defects, such as dislocations and grain boundaries. Experimentally, the amorphization fraction of SiC by ion irradiation has been measured as a function of irradiation dose [7-10]. The amorphization fraction – irradiation dose curve has a sigmoidal-like shape, which is consistent with all three mechanisms mentioned above. Molecular dynamics (MD) simulations have revealed that the completely amorphous state can be reached after generating a number of 10 keV Si or C atom recoils in a SiC crystal, which implies that an overlap of the displacement cascades may lead to the final c-a transition [12, 15]. However, MD simulations also found the formation of nanoscale amorphous domains after a direct impact of 50 keV Au ions with SiC, suggesting that direct amorphization is also a possible mechanism for heavier irradiation ions [13].

Despite many studies dedicated to this topic, a complete understanding of the microscopic mechanism governing the c-a transition remains elusive, as the detailed amorphization process is likely to depend on the irradiation species, their energy, the sample temperature and the nano/microstructure of the SiC. Moreover, these effects are not necessarily independent of each other. Of particular interest is to understand how the specific amorphization mechanism is affected by the presence of grain boundaries (GBs). This interest is driven by recent efforts devoted to improving radiation tolerance by refining the grain size of SiC to the nanometer regime [16-21]. Nanocrystalline (nc) materials have a high volume fraction of GBs, which act as sinks for point defects generated during irradiation [22]. As a result one can expect nc materials to be more efficient at annealing radiation-induced damage. Indeed experiments found that nc SiC showed a higher dose to amorphization than single crystal SiC irradiated with high energy electron and Si ions [16, 17]. Interestingly, however, reduction in radiation

resistance of SiC due to grain refinement was also reported based on several irradiation experiments using 1 MeV Si, 2 MeV Au and 1 MeV Kr ions [18, 20, 21]. What is particularly puzzling is that the same low pressure chemical vapor deposited (LPCVD) nc SiC was used in Refs. [16] and [17] (showing improved resistance to amorphization) and in Ref. [21] (showing a decreased resistance). It appears that the answer to the question whether nc covalent ceramics have superior or inferior resistance depends not only on the nano/microstructural features (GBs, stacking faults, dislocation density, etc.), but also on the irradiation type. A summary of experimental results on the effects of radiation type and temperature on RIA in SiC can be found in Ref. [21]. The seemingly contradictory effects of grain refinement on resistance to amorphization reported in the literature also imply that GBs may play multiple roles in amorphization and general radiation damage process. Understanding the complex nature of RIA is important for utilizing nano-engineering to design materials with superior radiation resistance.

High-resolution transmission electron microscopy (HRTEM) provides insight into the role of GBs in RIA, since HRTEM can be used for direct observation of the evolution of nano/microstructural features during irradiation. For instance, Ishimaru *et al.* used *in situ* HRTEM to observe structural changes during electron irradiation of 3C-SiC with nanolayered planar defects [23]. It was shown that after receiving the same dose, GBs were highly damaged and disordered while the intragranular regions on both sides of the GB maintained crystalline order. This result suggested that irradiation-induced defects were preferentially trapped at GBs, driving amorphization in that region. For ion irradiation, Snead *et al.* analyzed the shape and orientation of the amorphized areas in single crystal 3C-SiC implanted with 0.56 MeV Si$^+$ [24]. Amorphous islands (or amorphous pockets), typically 10 nm in width and more than 30 nm in length, were formed in the region beyond the damage peak where the sample was only partially

amorphized. These pockets had an elongated shape with the major axis aligned parallel to the surface of the specimen, regardless of the direction of the incident ion. The authors hypothesized that the orientation preference was either due to the strain field introduced by the amorphization or the free surface of the sample. However, the effects of microstructure (e.g., GBs) during the ion irradiation were not investigated.

In this chapter, we use HRTEM to investigate the morphology of amorphous regions in polycrystalline 3C-SiC irradiated with Kr ions and to determine the role that GBs play in RIA. An unusual morphology with a very fine structure of highly curved c/a boundaries is found in the partially amorphized sample. To understand how such morphology can arise, we have developed a coarse-grained model for damage evolution, which reproduces the experimental observations based on the combined effects of cascade overlap and the two-dimensional projection inherent to HRETM. By comparing the c/a morphologies at GBs and within the grain interiors, the complex effects of GBs on the amorphization process are investigated. Our analysis is enabled by development of a new algorithm for automatic identification of the amorphous regions in HRTEM images. Our analysis demonstrates the existence of the "interstitial starvation" in SiC, which proposes that preferential annihilation of interstitials at the GBs leaves behind excess vacancies that lead to amorphization. This mechanism was previously only postulated to occur in SiC based on simulations [25]. The influence of the dual role of GBs as sinks for point defects and as a source for interstitial starvation on the radiation resistant of nanocrystalline material is also discussed.

2.2 Experiment

2.2.1 Sample preparation

To obtain partially amorphous SiC samples, *in-situ* Kr^{2+} irradiation was conducted using the IVEM-Tandem facility at the Argonne National Laboratory. The TEM samples were prepared from polycrystalline CVD 3C-SiC sourced from Rohm & Hass with grain sizes ranging from 1 μm to 5 μm. The ion beam energy was 1 MeV and the flux was 6.25×10^{11} ions/cm²s. The irradiation temperature was measured by a thermocouple within the heated specimen stage and the temperature was controlled at 100 °C, which is below the RIA critical temperature in SiC. During irradiation, selected area electron diffraction patterns (SADP) of the sample were recorded periodically and were used to determine the degree of crystallinity of the sample (in Fig. 2.1). The sample was regarded as fully amorphous when diffraction spots disappeared and only diffuse rings remained. The irradiation fluence for complete amorphization was 1.30×10^{15} ions/cm², corresponding to a dose of 1.35 dpa (displacement per atom). Another sample was then irradiated to half of the dose to amorphization (0.675 dpa) and therefore was considered partially amorphous. SRIM ("Stopping power and Range of Ions in Matter") code was used to calculate the number of displacements per incident Kr ion as a function of specimen depth, and the average displacement number within the sample thickness was used to convert the fluence to dose in dpa [26]. Detailed settings for SRIM calculation are described in section 3.1. For additional thinning, the partially amorphous sample was ion milled on both sides with Fischione 1050 set at 600 V for 15 minutes after the irradiation. Detailed procedures for sample preparation and irradiation experiment can be found in Refs. [17] and [21]. The sample preparation was completed by my colleague Dr. Laura Jamison while she was a graduate student at UW-Madison in 2013.
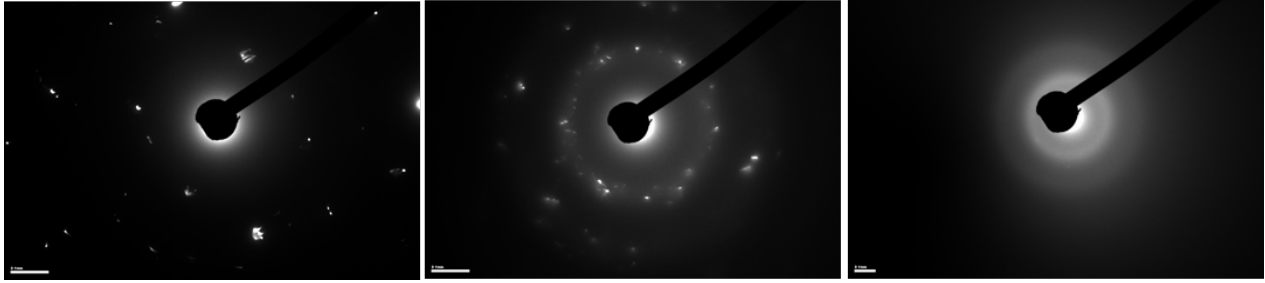
Figure 2.1 SADP of sample with 0%, 50%, and 100% of DTA

2.2.2 High resolution transmission electron microscopy

HRTEM is an image mode of the transmission electron microscope that can provide direct imaging of the atomic structure of the sample. The contrast of HRTEM comes from the interference in the image plane of the electron wave with itself so it is phase contrast. To see the atomic columns, the crystal should be aligned in specific directions that one low index zone plane is perpendicular to the electron beam. For general GBs (as compared to low angle tilt grain boundary or twin), there is no specific orientation relationship between the two grains on both sides. Therefore it is usually impossible to make two grains in the right directions for HRTEM simultaneously. However, it is possible to align the samples that the electron beam is close to the zone axis of low index planes of both grains. In this case, lattice fringes, instead of atomic column will be seen in HRTEM.

Another challenge for tilting is that HRTEM requires samples are thin enough (under 300 kV electron, thickness is less than 200 nm). SiC usually bents at the thin edge of the wedge polished sample. Therefore even one grain is tilted to the corrected position based on the diffraction from thick part, it may not be in zone at the thin edge, which HRTEM image should be taken. One feasible method is to use black bend contour in bright field image as an index of close-to-zone axis. As tiling angles continuously, the bend contour slides across the grain. As

long as the bent contours join at the grain boundary, it is very likely that the joining place satisfy the condition that both grains are very close to in-zone direction.

Ex-situ HRTEM images were taken using FEI Tecnai F30 microscope operated at 300 kV using the twin pole piece and with objective aperture radius of 47.3 mrad. Fig. 2.2 shows typical HRTEM images of an unirradiated sample and a sample that received half of the dose to amorphization. The insets show the corresponding SADP. For the unirradiated sample, the HRTEM image has clearly visible columns of atoms (or lattice fringes) in the entire area of the image and the SADP shows only sharp crystalline diffraction spots. In the image of the partially amorphous sample, amorphous domains of mottled contrast are mixed with crystalline domains with periodic lattice fringes and the SADP contains diffuse rings indicative of amorphous material in addition to crystalline spots.
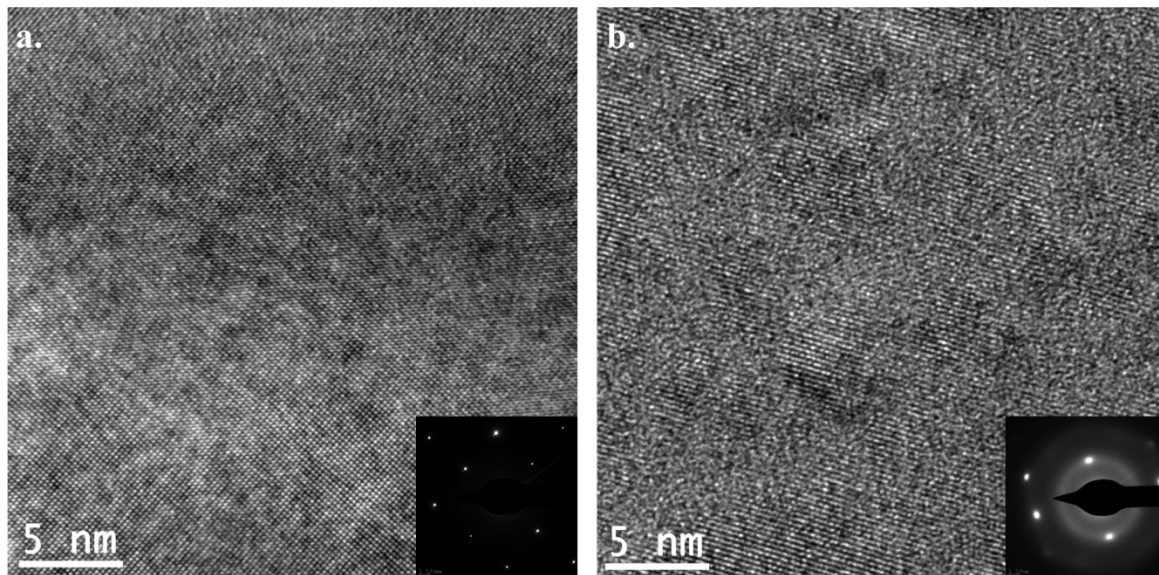
Figure 2.2 HRTEM images of (a) unirradiated 3C-SiC sample (b) sample received half of the dose to amorphization. Insets at the right corner of each image represent selected area diffraction patterns (SADP) for the perspective sample.

2.2.3 Algorithm for automatically identifying amorphous domains

In order to quantify the c/a fractions and boundaries, we have developed an automated analysis method that is free from observer bias to distinguish consistently the amorphous and crystalline regions in all HRTEM images. The procedure consists of three steps, which are illustrated in Figs. 2.3 – 2.5, respectively. In Step I, we Fourier filter the image, retain only the crystalline spots in the Fourier transform and then do the inverse Fourier transform (Fig. 2.3). The goal of this Fourier filtering step is to preserve the intensity of the crystalline part of the image while eliminating the intensity of the amorphous part. In Step II, we calculate the local standard deviation of the filtered intensity. The filtered image is divided into small squares and the intensity standard deviation of each small square is calculated. The standard deviation value is then interpreted as an index for the crystallinity. For a square located in an amorphous region, the distribution of pixel intensity is unimodal (Fig. 2.4b) and the standard deviation is low. However, for a square in a crystalline area with lattice fringes, the intensity distribution is bimodal because lattice fringes consist of both bright and dark strips (Fig. 2.4c) and therefore the standard deviation is high. It is worth noting that the square must be large enough to cover at least one dark and one bright lattice fringe otherwise the brightness distribution of the crystalline square will not be bimodal. We used squares 11 pixels to 14 pixels (corresponding to 2.5 to 3.2 Å) on a side, depending on the magnification and the lattice spacing of the HRTEM images. In step III, we select a standard deviation threshold (SD_{th}) that distinguishes crystalline and amorphous regions. This is achieved by fitting the histogram of standard deviation values to the sum of two Gaussian functions, one for the amorphous contribution and the other for the crystalline contribution, using Nelder-Mead non-linear iterative fitting method. For all the HRTEM images in the following discussion, the χ^2 test shows the histogram of standard

deviation values satisfies the fitted distribution at a 2.5% significance level and the adjusted R^2 of the fit is above 99%. Fig. 2.5 shows an example standard deviation fit. The standard deviation threshold is defined as $SD_{th} = SD_1 + \eta_{th} \times (SD_2 - SD_1)$, where SD_1 and SD_2 is the peak position of amorphous and crystalline Gaussians respectively. η_{th} is an adjustable parameter between 0 and 1, so $SD_1 < SD_{th} < SD_2$. Image squares with $SD > SD_{th}$ are labeled crystalline while squares with $SD < SD_{th}$ are labeled amorphous. We choose $\eta_{th}=0.8$ as it gives the best match between the c/a morphology generated by the processing code and human judgment applied to the HRTEM images. The same η_{th} value is used for processing of all images. Varying η_{th} from 0.7 to 0.9 results in variation of the amorphization fraction of the images by about 9%, but it does not change the trend of degrees of amorphization between different images, or the general features of the c/a morphology on which our conclusions are based. The Matlab code for this image processing can be find the appendix of this chapter.
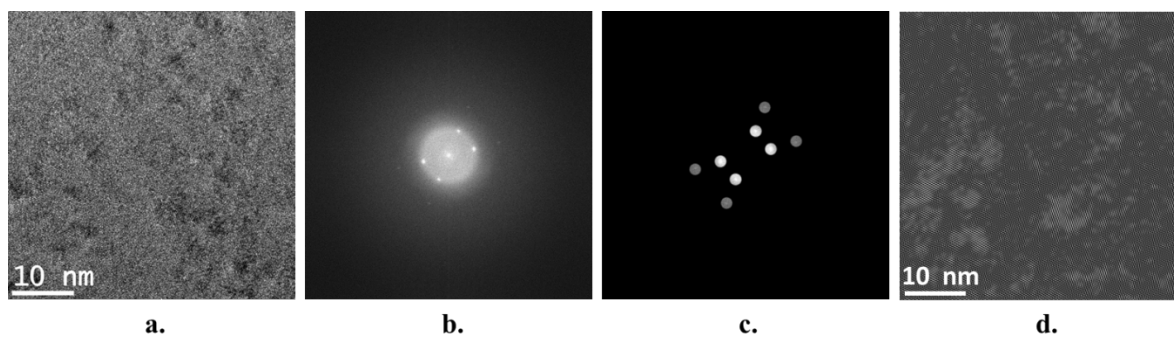
Figure 2.3 *Fourier filtering of the HRTEM images: (a) Original image, (b) FFT, (c) Crystalline spots preserved by using a mask, (d) inverse FFT.*
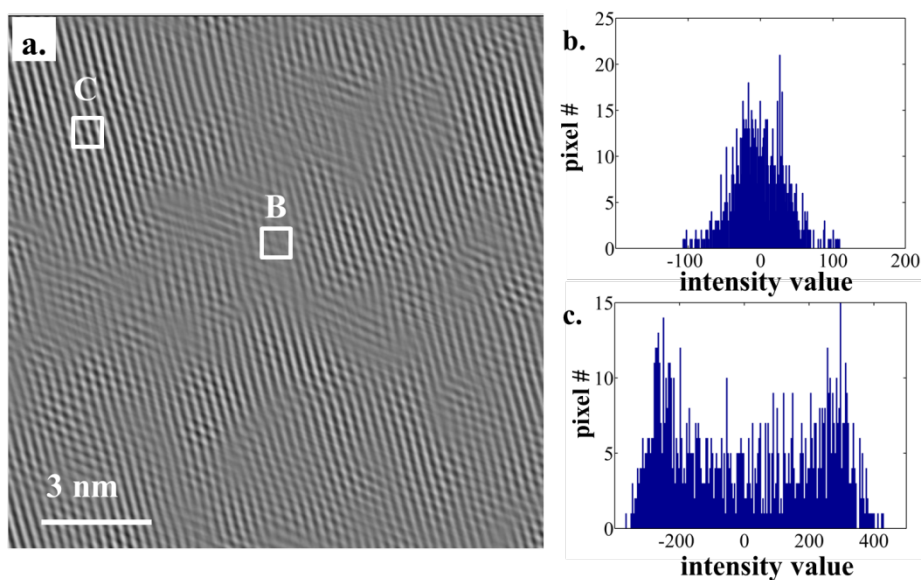
Figure 2.4*(a) Part of the Fourier filtered image (Fig. 2d) showing the positions of an amorphous square (labeled B) and a crystalline square (labeled C). Intensity histogram of (b) the amorphous square B and (c) the crystalline square C.*
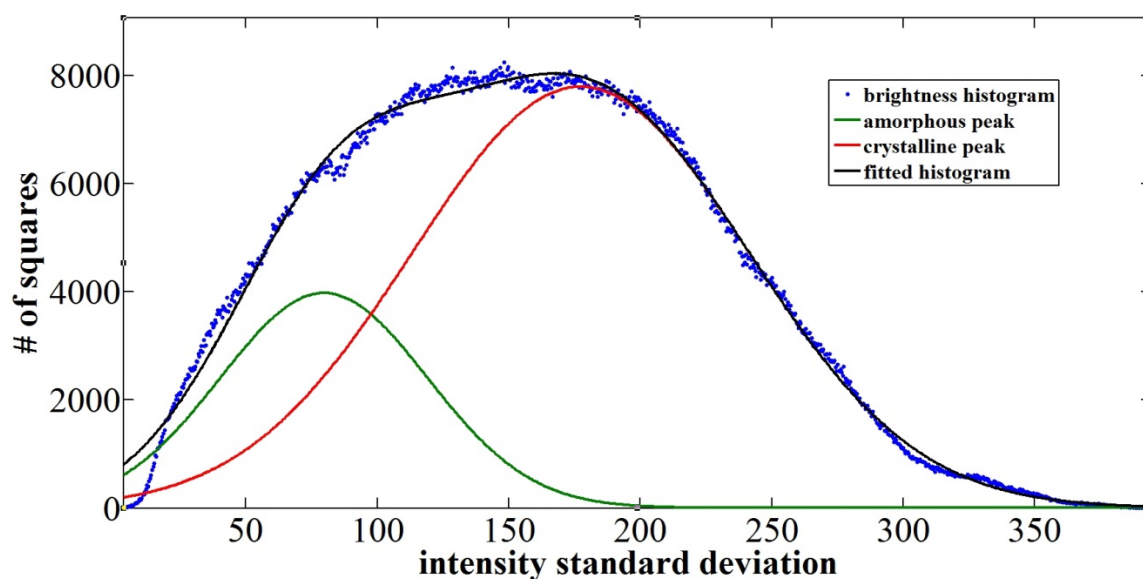
Figure 2.5 *Histogram of intensity standard deviation values of small squares. Blue dots are experimental values. Green line is the fitted amorphous Gaussian and red line is the fitted crystalline Gaussian. Black line is the sum of two Gaussians.*

To validate the method, one original HRTEM image of the partially amorphous SiC sample is compared with its processed image showing the c/a morphology in Fig. 2.6. In the HRTEM image (Fig. 2.6a), the c/a boundary determined by eye is shown by the white dashed lines. In the processed image (Fig. 2.6b), the white domains are identified as crystalline by the algorithm and the black domains are identified as amorphous. The two morphologies are generally consistent with each other with only a few small discrepancies.
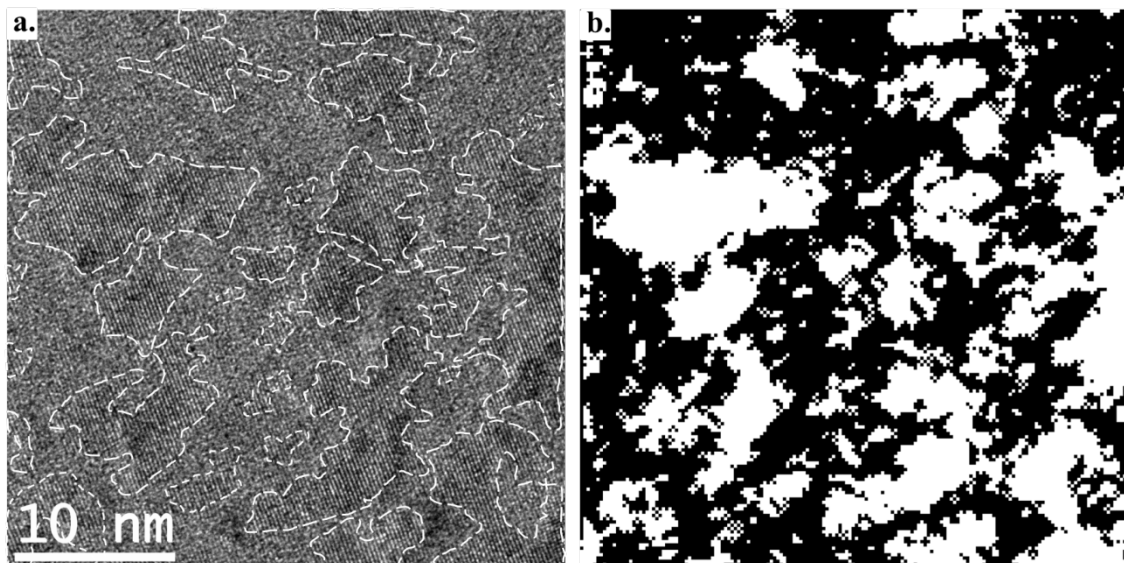
Figure 2.6 *Comparison of c/a morphologies in (a) the original HRTEM image with hand-drawn boundaries and (b) the image after processing. In (a) the c/a boundaries are shown as white dashed lines. In (b) white and black domains are crystalline and amorphous regions, respectively. The two images have the same magnification.*

2.2.4 Characteristic morphology of crystalline/amorphous zone boundaries

The morphology of the c/a domains offers clues to the mechanisms that govern amorphization. We analyzed a number of HRTEM images taken both near to and away from GBs. Fig. 2.7a shows a low magnification bright field image illustrating the types of locations where the HRTEM images were obtained. The black bands within the grains are bend contours. The discontinuity of the bands indicates different crystallographic orientations on both sides of

the white dotted lines, which is a GB. SADPs show the beam direction **b** is near [011] for the grain on the left (Fig. 2.7b) and near [1$\bar{1}\bar{2}$] for the grain on the right (Fig. 2.7c). The positions where HRTEM images were taken are marked with white squares. To avoid any influence by the GB, the image positions within the grain are at least 100 nm away from the GB. Fig. 2.8 shows three typical HRTEM images and the corresponding c/a morphologies determined using the automated procedure. One dramatic feature of the morphologies is the irregular shape of the amorphous regions surrounded by winding, highly curved c/a boundaries. Taken at face value, this "dendritic" morphology is surprising. From the perspective of thermodynamics, the c/a boundaries contribute excess interfacial energy to the system, so their total areas should be minimized in order to lower the system energy. This minimization would result in rounded shapes of amorphous domains with smooth, low curvature c/a boundaries (similar to the large amorphous pockets observed in SiC by Snead *et al.*[24]), not the structure shown in Fig. 2.8.
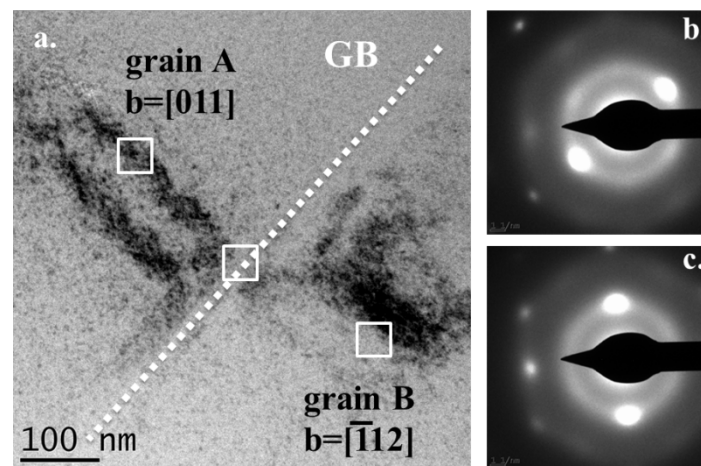
Figure 2.7 *(a) Bright field image showing locations of the HRTEM images (marked as squares) with respect to a GB (marked as dotted line). Vector **b** indicates the nearest low-index zone of each grain. (b) SADP of grain A and (c) SADP of grain B.*

Grain A   **GB**   **Grain B**

10 nm   **10 nm**   **10 nm**

a.   b.   c.

d.   e.   f.
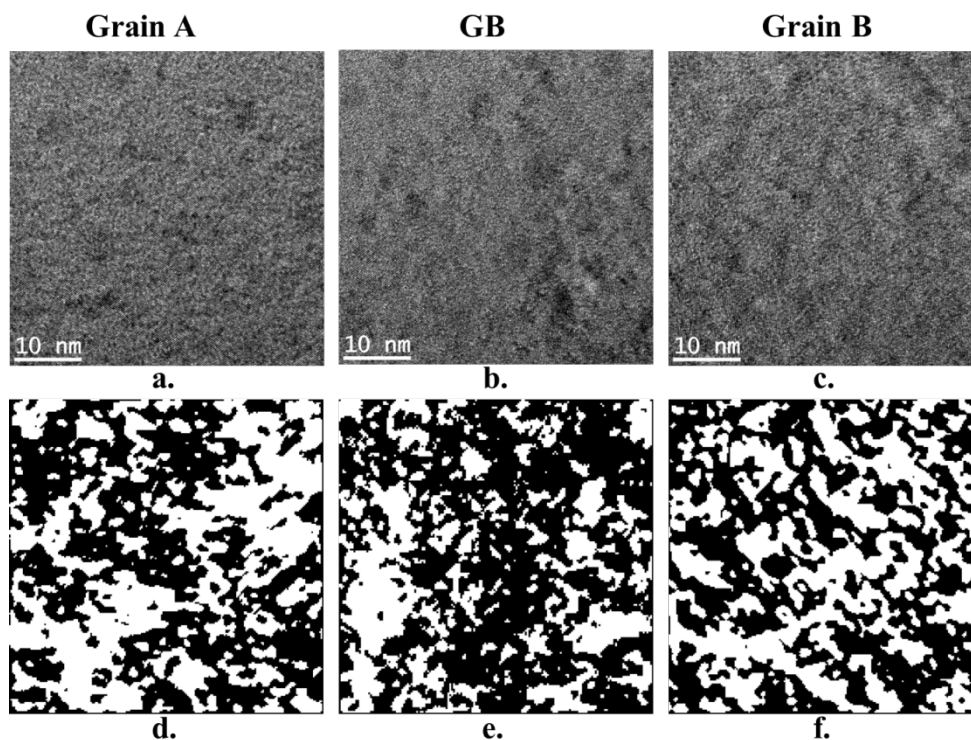
Figure 2.8 *(a-c) Original HRTEM images. (d-f) Corresponding images of the c/a morphologies from automated processing. In (d-f), white and black domains are crystalline and amorphous regions, respectively. All panels have the same magnification. These images correspond to the regions designated by white squares in Fig. 2.7.*

2.3 Simulation

2.3.1 Coarse-grained model for highly curved boundary morphology

The apparent morphology in Fig. 2.8 is a result of cascade overlap and the two-dimensional projection inherent to HRTEM, which we have demonstrated using a coarse-grained model of the amorphous pocket morphological evolution informed by SRIM and atomistic simulations. SRIM software is used to determine the number of primary knock-on atoms (PKAs) and their energies during irradiation with 1 MeV Kr ions. SRIM is a Monte Carlo simulation toolkit describing the collision process of ions with a target material [26]. In our calculation, the sample thickness is set to 50 nm, based on electron energy loss spectroscopy (EELS)

measurement of the TEM sample. According to the experimental Kr ion fluence (6.5×10^{14} ions/cm^2), 14,412 incident Kr ions impact a 47 nm × 47 nm region (the size of HRTEM image in Fig. 2.8). The displacement energy of Si and C is set to 35 eV and 21 eV, respectively [14, 16]. SRIM simulations indicate that all Kr ions pass through the sample with only a small amount of energy deposited. This result is not particularly surprising since the range of 1 MeV Kr^{2+} in SiC (the distance traveled by the incident ion before it loses all its kinetic energy to the host material) is about 3.8 µm, which is much larger than the 50 nm sample thickness. Table 2.1 lists the number and energy distributions of generated PKAs. It can be seen that the majority of PKAs have very low kinetic energy (< 1 keV) and less than 1% PKAs have energy larger than 50 keV.

Table 2.1 Number and energy distribution of PKAs generated by 1 MeV Kr2+ in a 50 nm-thick SiC

PKA energy	PKA number	Fraction of PKAs
In total	333,764	100.00%
0 keV - 1 keV	274,786	82.33%
1 keV - 10 keV	46,796	14.02%
10 keV - 50 keV	9,134	2.74%
> 50 keV	3,048	0.91%

These generated PKAs further collide with atoms in SiC and create displacement cascades. This process has been extensively studied by MD simulations [11, 27, 28]. According to such simulations, low energy PKAs (a few keV or less) are only able to create a few isolated point defects [27]. Medium range energies of PKAs (tens of keV) usually create a so-called collision cascade, which consists of clusters of vacancies, interstitials and antisite defects with a spatial range on the order of nanometers [28]. For PKAs with higher energy (e.g., 50 keV), simulations reported multiple branches of the cascades, each similar in size to cascades in the

medium energy range of PKAs [11]. As discussed in the introduction, MD simulations of Gao *et al.* found that the irradiated region became completely amorphous after the overlap of 112 cascades of 10 KeV Si or C PKAs [12]. In addition, the direct amorphization mechanism seems to be only important for heavy ions since no such directly amorphized region was found within the cascade of 50 keV Si PKA [13]., the possibility of direct amorphization is not included in our model.

These findings from SRIM and MD simulations are incorporated into a coarse-grain model simulating the evolution of the amorphous domains. In this model, the SiC sample is represented by a three dimensional (3D) square lattice of 217×217×230 points separated 2.18 Å apart, so the density of lattice points is equal to the atomic density of SiC and the dimension of the matrix is the same as the dimension shown in the HRTEM images (47nm×47nm×50nm). As the exact relation between the PKA energy and the resulting cascade size is currently unknown in SiC, we take the size of a displacement cascade created by a 10 keV PKA as a unit and assume that the effective number of unit cascades for a given PKA is proportional to its energy. For example, a 20 keV PKA creates two unit cascades while a 5 keV PKA creates half of the unit cascade. Therefore the total PKAs during the Kr^{2+} irradiation would create $7.89×10^4$ unit cascades in the sample. Here only cascades that have PKA energies larger than 1 keV are counted. Even though the low energy PKAs account for a substantial fraction in total PKA population, they only generate a few point defects each. These point defects form a homogeneous background, which is not expected to contribute to the heterogeneous morphological features of the c/a boundary. Based on Gao *et al.*'s simulations [28], the affected region of a 10 keV displacement cascade (one unit) is approximated as an ellipsoid with semi-

principle axes a=b=2.6nm and c=5.2 nm, where the c axis is parallel to the incident direction of Kr ions.

Cascade overlap is simulated by introducing elliptical cascades into the SiC matrix at random positions. A lattice point in the 3D matrix is considered to belong to an amorphous region after more than 112 cascades take place at that point. After irradiation, the sample matrix is projected onto the plane perpendicular to the incident beam as in HRTEM. An important parameter in making a projected image is the minimum amorphous volume fraction, x_{am}, in the 3D structure that is necessary for the 2D domains to appear as "amorphous" in the HRTEM images. Based on a series of image calculations using multislice method, Miller *et al.* [29] found that a sample could be up to thirty percent amorphous before the lattice periodicity in the HRTEM image was disrupted, and that a complete loss of lattice fringes occurred when the crystalline volume fraction dropped below twenty percent. Based on these findings, we choose x_{am}=80%. Fig. 2.9 shows the process for simulating the morphology using the coarsen-grained model.
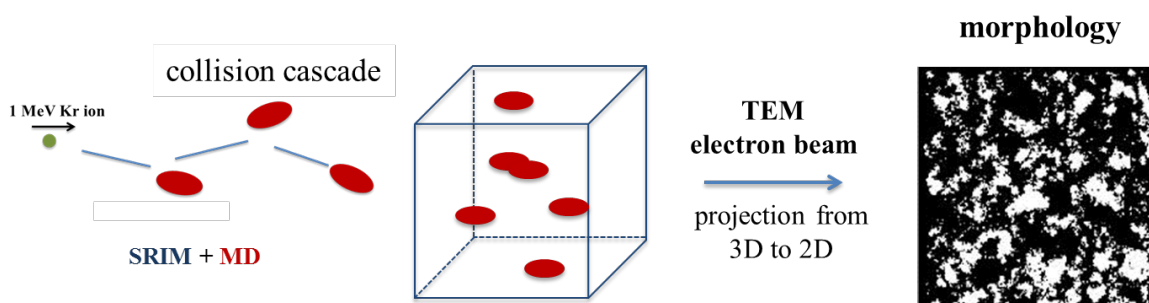
Figure 2.9 *Illustration of the coarsen-grained simulation for c/a boundary morphology*

Fig. 2.10 shows the final morphology generated for samples irradiated with Kr^{2+} up to half of the dose to amorphization (0.675 dpa). The irregular shape of amorphous regions and the winding c/a boundaries in the simulated morphologies agree well with the experimental results

shown in Fig. 2.6 and Fig. 2.8. Variation of x_{am} between 70% to 90% only affects the area ratio of amorphous to crystalline regions, not the qualitative features of the c/a boundaries. These simulations show that cascade overlap is the governing mechanism for amorphization under Kr^{2+} irradiation. Combined with 2D projection, cascade overlap is responsible for the observed dendrite-like c/a morphology. With this understanding, we investigated previously published HRTEM images of irradiated SiC and found similar morphologies in images reported by Cabrero *et al.* of the partially amorphous region just before the damage peak in 3C SiC irradiated by 76 MeV Kr ions [5]. Although the nature and origins of the morphologies were not discussed in that reference, we believe they are due to similar processes as seen in the present work. In fact, at the depth where their HRTEM image was taken (about 8 μm from the irradiated surface), the electronic interactions and nuclear interactions between incident ions and target materials are about the same. Interestingly, according to SRIM calculation, it means that the kinetic energy of the Kr ions has decreased to about 1 MeV at that depth, which is comparable to the Kr energy used in our study.
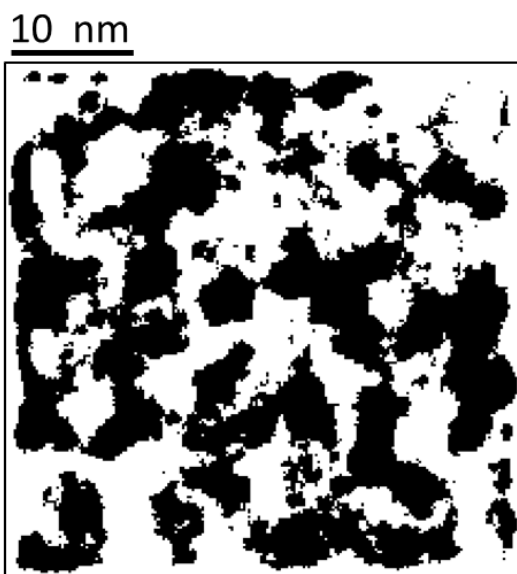
Figure 2.10 *c/a morphology simulated using a coarse-grained model. White and black colors represent crystalline and amorphous regions, respectively. Simulations correspond to experimental conditions of 1 MeV Kr^{2+} irradiation with fluence=6.5×10^{14} ions/cm^2.*

2.3.2 Intertitle starvation and rate theory model

Comparison of the c/a morphology at the GBs (Figs. 2.8b and 2.8e) and within grain interiors (Figs. 2.8a, 2.8c, 2.8d, and 2.8f) shows qualitatively that the amorphous domains are concentrated near the GB into a band of higher amorphization fraction. More quantitatively, the area fractions of amorphous domains in HRTEM images near and far from four different GBs are summarized in Table 2.2. The first and third columns contain values from images on both sides of the GB, and the second column shows the amorphization fraction from images that contain a GB. For locations 3 and 4, three images were taken at nearby positions for the same grain or GB, so the table reports the mean and standard deviation of amorphization fractions for the three images. Images containing a GB always have a higher amorphization fraction than those within the grain interiors, implying that GBs increase the rate of amorphization in their vicinity. This phenomenon can be seen more clearly from the local amorphization fraction of narrow strips parallel to the GB. Fig. 2.10 shows the amorphization fraction within a 3 nm wide strip, Φ_{am}, as a function of the strip's position in each HRTEM image. In Fig. 2.10b, the peak value of Φ_{am} is nearly 80% right at the GB and Φ_{am} gradually decreases on both sides. Similar data for the grain interior shows no such peak or gradient (Figs. 2.10a and 2.10c). The Φ_{am} profiles indicate that the enhancing effect of GBs on the amorphization process is highly localized. At approximately 15 − 25 nm away from GB, Φ_{am} has already decreased close to the average amorphization fractions of grain interiors on both sides. It should be emphasized that the "amorphization fraction" here refers to area fraction of amorphous domains, not the volume

amorphization fraction in a 3D sample. As demonstrated in Ref. [29], the relationship between area fraction and volume fraction is monotonic but not linear. In addition, the exact area fraction value also depends on the criterion defining the "amorphous domains" (e.g., the parameter η_{th}). Therefore it would be difficult to determine quantitatively the volume amorphization fraction simply based on the 2D projections. However, the key point is that all the images from different locations on the sample show the same trend, as long as the same image processing method is applied. Therefore the local enhancement of amorphization by a GB is a real phenomenon, rather than an artifact introduced by the image processing.

Table 2.2 *Comparison of the areal amorphization fraction in HRTEM images with and without GB. Uncertainties for location 3 and 4 are the standard deviation over three nearby images.*

	grain A	GB	grain B	grain orientation
Location 1	53%	64%	52%	$[011] // [1\bar{1}\bar{2}]$
Location 2	55%	66%	59%	$[011] // [011]$
Location 3	53±1%	62±2%	51±1%	$[011] // [011]$
Location 4	51±1%	62±1%	50±5%	$[\bar{1}11] // [1\bar{1}\bar{2}]$
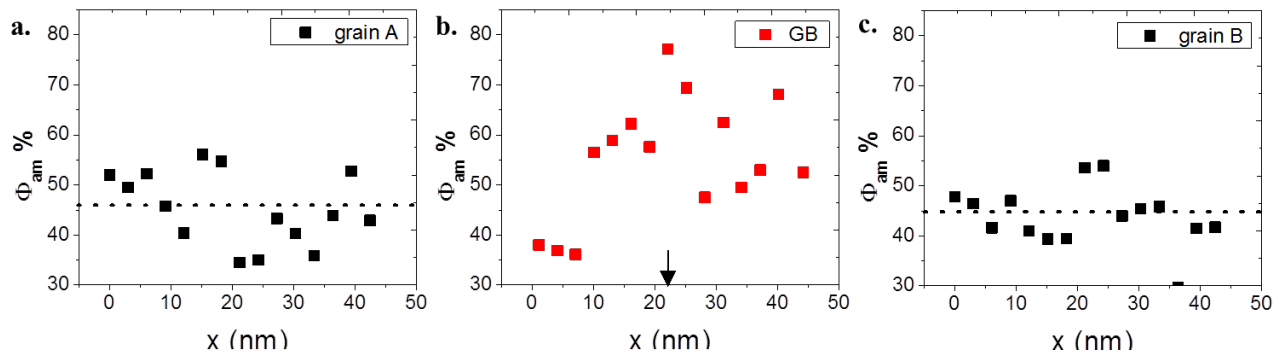
***Figure 2.11** Local amorphous area fraction (Φ_{am}) in 3 nm strips as a function of the strip position (x) in HRTEM images. The position of the GB in (b) is marked by an arrow. Horizontal dotted lines in (a) and (c) indicate the average amorphization ratio in HRTEM images of grain A and B.*

The locally enhanced amorphization due to GBs seems contradictory given that GBs typically act as defect sinks. In fact, depleted zones of defects are often observed near GBs in metals [30]. There are several possible explanations for the unexpected effect of the GBs. First, the GBs might increase the defect production rate/survival efficiency and therefore more defects would appear near GBs. This effect has been studied by MD simulations of radiation damage in SiC bicrystals with both low angle and high angle GBs [31, 32]. It was found that defect production in GB regions was increased because the local disorder lowered the threshold displacement energies. However, the GB width (estimated to be about 4.92 Å in Ref. [31]) is much narrower than the affected region shown in our HRTEM images (about 15-25 nm). For defect production in crystalline regions adjacent to GBs, it was demonstrated that the defect production was largely unaffected by the presence of a GB and was independent of the GB type. Therefore the first hypothesis cannot explain the locally enhanced amorphization near GBs. A second possibility is that the amorphous phase might nucleate at the GBs and then grow into the grain. If this mechanism was dominant, a continuous amorphous band extending from the GB plane into grains on both sides of the GB would be expected. However, such bands are not found in the HRTEM images. Instead, amorphous domains can be seen as more networked along the GB as shown in Fig. 2.8e. Also, the amorphization fraction gradually decreases from the highest value at the GB to a lower value in the grain interior (Fig. 2.10b). Thus the nucleation and growth of the amorphous phase at the GBs cannot explain the locally enhanced amorphization.

The third possible explanation is interstitial starvation, which results from the high-energy barrier for recombination of C Frenkel pairs and the different diffusivities of self-interstitials and vacancies [25]. After initial intracascade recombination, the surviving radiation-induced interstitials and vacancies can be annihilated either by migrating to defect sinks, or by defect recombination. According to *ab initio* calculations [25, 33], the barrier for a C interstitial and vacancy to recombine is as high as 0.90 eV. Therefore this recombination reaction is not activated in our irradiation experiment and annihilation at defect sinks (e.g., GBs) becomes the dominant process in healing C point defects. Meanwhile, the migration barrier for C interstitials is much smaller (0.60 eV) than for C vacancies (3.66 eV). GBs are sinks for mobile C interstitials but not for immobile vacancies at the experimental temperature of 100 °C. The imbalance between the annihilation of C vacancies and interstitials results in an excess of vacancies near GBs. The excess vacancies accumulate as the irradiation continues and drive the regions adjacent to the GBs into the amorphous phase. The gradient of the vacancy density causes a gradient in the amorphization fraction as a function of distance from the GB. The interstitial starvation mechanism has been theoretically predicted by rate theory calculations in SiC [25], and a similar effect in Si was also observed experimentally by Atwater *et al.* [34]. However, to our best knowledge, no experimental evidence for interstitial starvation phenomenon has been previously reported in SiC.

A simplified rate theory calculation is conducted here to demonstrate that interstitial starvation explains the Φ_{am} peak and gradient we observe. The one-dimension rate theory model is described by [25]

$$\frac{dc_i(x,t)}{dt} = D_i \nabla^2 c_i(x,t) + G - Rc_i(x,t)c_v(x,t) \tag{2.1}$$

$$\frac{dc_v(x,t)}{dt} = D_v \nabla^2 c_v(x,t) + G - Rc_i(x,t)c_v(x,t) \tag{2.2}$$

Here subscripts *i* and *v* stand for interstitial and vacancy, respectively, and $c(x,t)$ is the defect concentration at irradiation time *t* at position *x* in the grain. Four kinds of point defect, interstitials and vacancies of Si and C, are considered so there are four partial differential equations in total. *G* stands for defect generation rate, which is defined as

$$G = \Gamma \eta \alpha_n \tag{2.3}$$

Γ is the dose rate, which is 6.48×10^{-4} dpa/s in the *in-situ* Kr^{2+} irradiation. η is the intracascade recombination rate (set to 0.8) and a_n is the generation fraction of defect of type *n*. *R* stands for the reaction rate of vacancy-interstitial recombination, which has the general form [35, 36]

$$R = 4\pi r_c (D_i + D_v) \, for \, E_m \gg E_r \tag{2.4}$$

$$R = 4\pi r_c (D_i + D_v) \exp\left(\frac{E_m^{fast} - E_r}{k_B T}\right) for \, E_m \approx or < E_r \tag{2.5}$$

In equations (2.4) and (2.5) r_c is the recombination reaction radius, E_r is the reaction energy barrier, E_m is the migration barrier and E_m^{fast} is the migration barrier for the faster defect of the two defects participating in the recombination reaction. The parameter values used in this calculation are summarized in Table 2.3, all of which are taken from Refs. [25] and [33]. To be consistent with experimental conditions, the grain size is assumed to be 1 μm and the irradiation is performed over 1040 seconds (which corresponds to 0.675 dpa). As boundary conditions, the defect concentrations at GBs are set equal to zero throughout the entire calculation. The initial interstitial and vacancy concentrations are assumed to be zero as well. We use the excess energy ΔE as a function of the calculated defect concentration to estimate of the degree of amorphization. ΔE is the sum of extra energy contributions from all four kinds of point defects to the system

$$\Delta E = \sum \Delta E_x c_x \tag{2.6}$$

In equation (2.6), ΔE_x is the energy gained by introducing one point defect and x stands for interstitial or vacancy of either C or Si. The values of ΔE_x are obtained from Ref. [25] and summarized in Table 2.3. In the model the sample is regarded as completely amorphous when ΔE equals the energy difference between the amorphous and crystalline phase (ΔE_{am}). We choose $\Delta E_{am} = 0.6$ eV/atom based on previous MD simulations [37].

Table 2.3 *Parameter values used in the rate theory calculations (from Ref. [25, 36]). "I" stands for interstitial and "V" stands for vacancy.*

	D / cm^2/s	E_m/eV	ΔE_x/eV	a_n	E_r/eV	r_c/nm
Si, I	2.08×10^{-14}	0.83	8.745			
Si, V	2.70×10^{-36}	2.40	4.966	0.075	0.03	0.63
C, I	1.09×10^{-12}	0.60	6.953			
C, V	2.47×10^{-53}	3.66	4.193	0.435	0.90	0.21

Fig. 2.11 shows ΔE as a function of position in a 1 µm grain. In the middle region of the grain, ΔE is low (less than 0.1 eV) because of the mutual recombination of interstitials and vacancies. ΔE increases sharply close to GBs since a significant fraction of interstitials diffuse to the GB and leave behind copious unrecombined vacancies. As shown in the inset of Fig. 2.11, the conditions $\Delta E = \Delta E_{am}$ is met at about 6 nm from a GB, and $\Delta E = 0.5 \Delta E_{am}$ occurs at about 22 nm. The distribution of ΔE implies that interstitial starvation could produce an affected region tens of nanometers wide, similar to the width observed in our experiments (Fig. 2.10b). It is worth pointing out that the high-energy barrier for C Frenkel pair recombination ($E_r = 0.90$ eV) plays a critical role in determining the size of the affected region. If we assume there is no barrier

for the recombination, then $\Delta E = 0.5 \Delta E_{am}$ would occur at the distance of only about 0.3 nm from a GB, which means that without recombination barriers there would be no interstitial starvation. One should of course keep in mind that the exact size of the affected region by interstitial starvation may change due to the uncertainties of the parameters in the model (defect diffusivity, reaction barriers, etc.) and in the experiments. Nevertheless this calculation shows that interstitial starvation can produce effects on the scale of the experimentally observed peak and gradient of amorphization fraction near a GB.
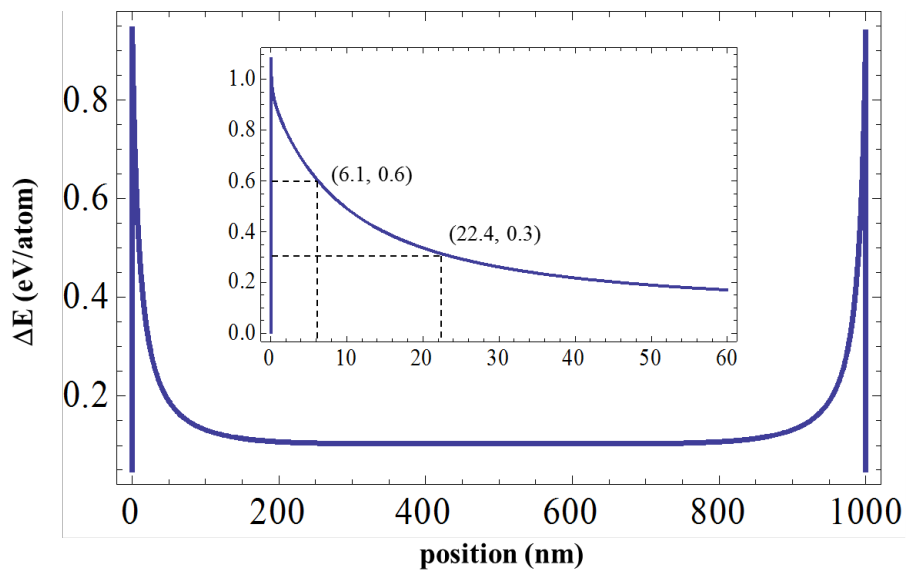
Figure 2.12 *Excess energy ΔE as a function of position within a 1 μm grain. GBs are located at x=0 nm and 1000nm. In the inset we show a magnification of the left part of the curve in order to clearly show the position where ΔE=ΔE_am=0.6 eV/atom and ΔE=0.5ΔE_am = 0.3 eV/atom.*

2.4 Discussion and Conclusion

Understanding gained from our study has important implications for the question regarding whether refining the grain size to nanometer scale will improve the resistance of SiC to RIA. Previous experiments found that the same nc SiC exhibited a superior resistance compared to microcrystalline or single crystal SiC when irradiated with 1.25 MeV electrons and 2 MeV Si

ions, but inferior resistance when irradiated with 1 MeV Kr ions [16, 17, 21]. Current explanations for the performance discrepancy are mostly focused on the material microstructures. Increased resistance to RIA has been attributed to the higher volume fraction of GBs acting as defect sinks. Decreased resistance to RIA has been attributed to the high GB fraction increasing the free energy of the material, which makes the system less stable and more susceptible to amorphization. Although these arguments are perhaps valid, they are insufficient to explain the different behaviors of the same nanocrystalline materials under different irradiation conditions. The coupling between different amorphization mechanisms and the material microstructures demonstrated here helps shed light on this mystery. Due to their light mass, electrons are only able to generate isolated Frenkel pairs. These point defects migrate, accumulate and finally lead to amorphization. For this type of amorphization process, defect annihilation at GBs becomes more efficient when the grain size is smaller (because of a larger volume fraction of GBs) and this is the dominant factor in improving the material resistance. However, as revealed by the HRTEM images and morphology simulations in this study, cascade overlap is the governing amorphization mechanism for heavy ion irradiation, such as Kr. Within the highly disordered region, or displacement cascade, there are both point defects and a large number of defect clusters. These defect clusters are very stable and much less mobile than point defects, which make it difficult for the clusters to be annihilated at GBs. Light ions, like Si, are less effective in transferring kinetic energy to PKAs due to their lower mass. As mentioned earlier, low energy PKAs tend to produce dispersed point defects rather than concentrated displacement cascades, so amorphization by light ions may be driven more by defect accumulation, which is similar to the case for electrons. In addition to the different amorphization mechanisms, interstitial starvation may also play a substantial role in determining

the RIA resistance of nc SiC by enhancing the local amorphization process near GB. This effect is probably negligible for materials with large grains (because it is limited to the regime of about 20 nm on either side of the GB), but it would become significantly more important when the grain size is refined. GBs suppress RIA (increase resistance) because they act as sinks for point defects, but also facilitate the amorphization process because of the interstitial starvation. A balance of the two competing effects could lead to an intermediate grain size that maximizes the radiation resistance of SiC.

In summary, the amorphization mechanism in SiC with Kr ion irradiation is investigated by both HRTEM and coarse-grained simulation methods. It is demonstrated that the unique morphology of the partially amorphous sample results from the overlap of displacement cascades, which is the governing amorphization mechanism under heavy ion irradiation. The different amorphization mechanisms may help explain different behaviors of nc SiC irradiated with different irradiation species. By comparing local amorphization fractions near GBs and in grain interior, the interstitial starvation phenomenon is identified, which might become a considerable deteriorating effect for nanocrystalline SiC when the grain size is small enough.

Appendix

      Below is the Matlab code for processing the original HRTEM image to get the

crystalline/amorphous morphology.

```matlab
% Code for processing HRTEM image to get crystalline/amorphous
morphology
% The peakfit.m function is from
http://terpconnect.umd.edu/~toh/spectrum/InteractivePeakFitter.htm


%PART I: Input parameters and names

No_images=1;     % How many images the code will process
dim=2048;        % The pixel number of TEM image 2048*2048
square_size=8;   % The size of small squares in pixels
no_square=256;   % (No. of small squares are needed)^1/2
std_vector=zeros(no_square*no_square,1);
local_image=zeros(square_size,square_size);

app='done_';
name1='ifft_420K_BF.tif'; % image name before the processing
save_name1=[app name1];    % image name after the processing

name_matrix={name1}; % Can add more image names if more than one
images are processed
save_name_matrix={save_name1}; % Can add more names if more than one
images are processed

hist_bin_num=125; % No. of bins in the histogram of local standard
deviation value. Tunable parameter

output='result_std_local';  % name of output file containing local SD
value
filename=strcat(output,'.txt');
fid=fopen(filename,'wt');


%PART II: Segment the HRTEM image, calculate local intensity standard
%deviation (SD) values, get threshold SD between crystalline and
amophouse squares

for i=1:No_images
    image_matrix=imread(name_matrix{i});  % Read in image for
processing
    pic_matrix=zeros(dim,dim);                 % Matrix to store the
processed image
    crystal=0.0;                               % No. of crystalline squares
in the entire image
    std_ser_no=0;          % Serial No. of squares: 1 - no_square^2
```

```matlab
    for A=1:no_square
        for B=1:no_square
            std_ser_no=std_ser_no+1;
            x_low=(A-1)*square_size+1;      % define the square X,Y
boundary in the image
            x_high=A*square_size;
            y_low=(B-1)*square_size+1;
            y_high=B*square_size;
            local_image=image_matrix(x_low:x_high,y_low:y_high); %
Segment local image from the original HRTEM image
            std_vector(std_ser_no)=std2(local_image);            %
Calculate local intensity SD of the square

        end
    end
            [std_num, std_position]=hist(std_vector,hist_bin_num); %
Get the histogram of all the SD values
            std_position_double=double(std_position);            %
convert the integer historgram to floating number
            peakinfo=peakfit([std_position_double;std_num],0,0,2); %
peakfit fit the histogram to two gussians
            separation=peakinfo(3)+0.8*(peakinfo(4)-peakinfo(3));   %0.8
is tunable parameter, peakinfo(3)&(4) are the centers of two Gaussian
profiles

    local_image=zeros(square_size,square_size);


%PART III: Use the threshold SD value (separation) to tell whether the
local square is crystalline or amorphous

    for A=1:no_square
        for B=1:no_square
            x_low=(A-1)*square_size+1;           % Define the square
X,Y boundary in the image
            x_high=A*square_size;
            y_low=(B-1)*square_size+1;
            y_high=B*square_size;

            local_image=image_matrix(x_low:x_high,y_low:y_high);

            if std2(local_image)>separation     % if SD value >
threshold, then the square is crystalline
                pic_matrix(x_low:x_high,y_low:y_high)=1.0;
                crystal=crystal+square_size*square_size;
            else                                 % if SD value <
threshold, then the square is amorphous
                pic_matrix(x_low:x_high,y_low:y_high)=0.0;
            end

        end
```

```matlab
    end


    figure, imshow(pic_matrix);    % Output the processed morphology
to pic_matrix
    imwrite(pic_matrix,save_name_matrix{i},'tiff');
    amorph_ratio=1-(crystal)/(dim*dim);    % calculate the
amorphization ratio of this image
    fprintf(fid,'%20s %s %6.4f\n',name_matrix{i},'amorphous ratio
is',amorph_ratio); % Output the amorphization ratio
end
```

Bibliography

[1] L.L. Snead, T. Nozawa, Y. Katoh, T.S. Byun, S. Kondo, D.A. Petti, Handbook of SiC properties for fuel performance modeling, J Nucl Mater, 371 (2007) 329-377.

[2] Y. Katoh, L.L. Snead, I. Szlufarska, W.J. Weber, Radiation effects in SiC for nuclear structural applications, Curr Opin Solid St M, 16 (2012) 143-152.

[3] W.J. Weber, Models and mechanisms of irradiation-induced amorphization in ceramics, Nucl Instrum Meth B, 166 (2000) 98-106.

[4] V.I. Ivashchenko, P.E.A. Turchi, V.I. Shevchenko, Simulations of the mechanical properties of crystalline, nanocrystalline, and amorphous SiC and Si, Phys Rev B, 75 (2007) 085209.

[5] J. Cabrero, F. Audubert, R. Pailler, A. Kusiak, J.L. Battaglia, P. Weisbecker, Thermal conductivity of SiC after heavy ions irradiation, Journal of Nuclear Materials, 396 (2010) 202-207.

[6] M. Ishimaru, I.T. Bae, A. Hirata, Y. Hirotsu, J.A. Valdez, K.E. Sickafus, Volume swelling of amorphous SiC during ion-beam irradiation, Phys Rev B, 72 (2005) 024116.

[7] W.J. Weber, L.M. Wang, N. Yu, The irradiation-induced crystalline-to-amorphous phase transition in alpha-SiC, Nuclear Instruments & Methods in Physics Research Section B-Beam Interactions with Materials and Atoms, 116 (1996) 322-326.

[8] E. Wendler, A. Heft, W. Wesch, Ion-beam induced damage and annealing behaviour in SiC, Nuclear Instruments & Methods in Physics Research Section B-Beam Interactions with Materials and Atoms, 141 (1998) 105-117.

[9] W. Bolse, Formation and development of disordered networks in Si-based ceramics under ion bombardment, Nuclear Instruments & Methods in Physics Research Section B-Beam Interactions with Materials and Atoms, 141 (1998) 133-139.

[10] W. Bolse, Amorphization and recrystallization of covalent tetrahedral networks, Nuclear Instruments & Methods in Physics Research Section B-Beam Interactions with Materials and Atoms, 148 (1999) 83-92.

[11] F. Gao, W.J. Weber, Atomic-scale simulation of 50 keV Si displacement cascades in beta-SiC, Physical Review B, 63 (2001) 054101.

[12] F. Gao, W.J. Weber, R. Devanathan, Defect production, multiple ion-solid interactions and amorphization in SiC, Nuclear Instruments & Methods in Physics Research Section B-Beam Interactions with Materials and Atoms, 191 (2002) 487-496.

[13] W.J. Weber, F. Gao, R. Devanathan, W. Jiang, C.M. Wang, Ion-beam induced defects and nanoscale amorphous clusters in silicon carbide, Nuclear Instruments & Methods in Physics Research Section B-Beam Interactions with Materials and Atoms, 216 (2004) 25-35.

[14] C. Jiang, M.J. Zheng, D. Morgan, I. Szlufarska, Amorphization Driven by Defect-Induced Mechanical Instability, Physical Review Letters, 111 (2013) 155501.

[15] F. Gao, W.J. Weber, Cascade overlap and amorphization in 3C-SiC: Defect accumulation, topological features, and disordering, Phys Rev B, 66 (2002) 024106.

[16] Y.W. Zhang, M. Ishimaru, T. Varga, T. Oda, C. Hardiman, H.Z. Xue, Y. Katoh, S. Shannon, W.J. Weber, Nanoscale engineering of radiation tolerant silicon carbide, Physical Chemistry Chemical Physics, 14 (2012) 13429-13436.

[17] L. Jamison, M.J. Zheng, S. Shannon, T. Allen, D. Morgan, I. Szlufarska, Experimental and ab initio study of enhanced resistance to amorphization of nanocrystalline silicon carbide under electron irradiation, Journal of Nuclear Materials, 445 (2014) 181-189.

[18] W. Jiang, H. Wang, I. Kim, Y. Zhang, W.J. Weber, Amorphization of nanocrystalline 3C-SiC irradiated with Si+ ions, J Mater Res, 25 (2010) 2341-2348.

[19] W. Jiang, H. Wang, I. Kim, I.T. Bae, G. Li, P. Nachimuthu, Z. Zhu, Y. Zhang, W.J. Weber, Response of nanocrystalline 3C silicon carbide to heavy-ion irradiation, Physical Review B, 80 (2009) 161301(R).

[20] W.L. Jiang, L. Jiao, H.Y. Wang, Transition from Irradiation-Induced Amorphization to Crystallization in Nanocrystalline Silicon Carbide, Journal of the American Ceramic Society, 94 (2011) 4127-4130.

[21] L.S. Jamision, K.; Shannon, S.; Szlufarska, I., Temperature and irradiation species dependence of radiation response of nanocrystalline sillicon carbide, J Mater Res, 29 (2014) 2871-2880.

[22] X.M. Bai, A.F. Voter, R.G. Hoagland, M. Nastasi, B.P. Uberuaga, Efficient Annealing of Radiation Damage Near Grain Boundaries via Interstitial Emission, Science, 327 (2010) 1631-1634.

[23] M. Ishimaru, Y.W. Zhang, S. Shannon, W.J. Weber, Origin of radiation tolerance in 3C-SiC with nanolayered planar defects, Applied Physics Letters, 103 (2013) 033104.

[24] L.L. Snead, S.J. Zinkle, J.C. Hay, M.C. Osborne, Amorphization of SiC under ion and neutron irradiation, Nuclear Instruments & Methods in Physics Research Section B-Beam Interactions with Materials and Atoms, 141 (1998) 123-132.

[25] N. Swaminathan, D. Morgan, I. Szlufarska, Role of recombination kinetics and grain size in radiation-induced amorphization, Physical Review B, 86 (2012) 214110.

[26] J.F. Ziegler, Srim-2003, Nuclear Instruments & Methods in Physics Research Section B-Beam Interactions with Materials and Atoms, 219 (2004) 1027-1036.

[27] J.M. Perlado, L. Malerba, A. Sanchez-Rubio, T.D. de la Rubia, Analysis of displacement cascades and threshold displacement energies in beta-sic, Journal of Nuclear Materials, 276 (2000) 235-242.

[28] R. Devanathan, W.J. Weber, T.D. de la Rubia, Computer simulation of a 10 keV Si displacement cascade in SiC, Nuclear Instruments & Methods in Physics Research Section B-Beam Interactions with Materials and Atoms, 141 (1998) 118-122.

[29] M.L. Miller, R.C. Ewing, Image Simulation of Partially Amorphous Materials, Ultramicroscopy, 48 (1993) 203-237.

[30] S. Kondo, Y. Katoh, L.L. Snead, Analysis of grain boundary sinks and interstitial diffusion in neutron-irradiated SiC, Physical Review B, 83 (2011) 075202.

[31] N. Swaminathan, P.J. Kamenski, D. Morgan, I. Szlufarska, Effects of grain size and grain boundaries on defect production in nanocrystalline 3C-SiC, Acta Mater., 58 (2010) 2843-2853.

[32] N. Swaminathan, M. Wojdyr, D.D. Morgan, I. Szlufarska, Radiation interaction with tilt grain boundaries in beta-SiC, Journal of Applied Physics, 111 (2012).

[33] M.J. Zheng, N. Swaminathan, D. Morgan, I. Szlufarska, Energy barriers for point-defect reactions in 3C-SiC, Physical Review B, 88 (2013) 054105.

[34] H.A. Atwater, W.L. Brown, Grain-Boundary Mediated Amorphization in Silicon during Ion Irradiation, Applied Physics Letters, 56 (1990) 30-32.

[35] N. Swaminathan, D. Morgan, I. Szlufarska, Ab initio based rate theory model of radiation induced amorphization in beta-SiC, Journal of Nuclear Materials, 414 (2011) 431-439.

[36] T.R. Waite, General Theory of Bimolecular Reaction Rates in Solids and Liquids, Journal of Chemical Physics, 28 (1958) 103-106.

[37] R. Devanathan, F. Gao, W.J. Weber, Amorphization of silicon carbide by carbon displacement, Applied Physics Letters, 84 (2004) 3909-3911.

3. Radiation-induced segregation near grain boundaries in silicon carbide

3.1 Introduction to radiation-induced serration

In chapter 2, the interactions between defect and grain boundaries (GB) in silicon carbide (SiC) at low temperature have been investigated. In order to use grain refinement to optimize the material's properties, it is important to obtain a thorough understanding of the defect-GB interactions at various temperature ranges. When the environment temperature is higher than the critical amorphization temperature (about 430 K), the diffusion and recombination of radiation-induced defects are fast enough that SiC can no longer be amorphized by irradiation [1,2]. Instead, radiation-induced segregation (RIS) may take place in regions near interfaces like GB, surfaces and dislocations. RIS was firstly discovered in Fe-18Cr-8Ni-1Si stainless steel in 1970s and then turned out be a commonly observed effect in variety of alloys after elevated temperature irradiation [3]. In general, RIS is due to the coupling between fluxes of radiation-induced defects and fluxes of alloy elements to defect sinks [4]. During irradiation, Frenkel pairs and defect clusters are generated by incident particles (neutron, ion, electrons) and randomly distributed throughout the material. Those defects that are mobile and can escape from defect reactions (e.g. recombination) tend to move to sinks. Since the motion of defect is caused by the motion of atoms, fluxes of atoms are associated with defect flux. Any preferential association of defects with a particular alloying element will result in a net flux of the alloying element to sinks [5]. RIS can cause either buildup or depletion of alloying elements in the vicinity of grain boundaries and surfaces, leading to concentration gradient in the initially homogenous alloy. Back diffusion due to the concentration gradient will balance the element flux and a quasi-steady state may be set up during the irradiation [6].

The segregation effect is one of the major concerns for nuclear structure materials, since RIS may alter the distribution of the alloy addition and substantially modify materials properties [3,4,7–10]. For example, Cr is added to austenitic Ni-based super alloy to provide corrosion resistance. Experiment results indicated that RIS causes Cr to be depleted near GB and surfaces, where metals are most susceptible to corrosion attack [9,10]. The GB Cr depletion is linked to intergranular stress corrosion cracking, which is called irradiation assisted stress corrosion cracking (IASCC) and poses a serious threat to the integrity of reactor core component and life extension of current reactor fleet [4]. The segregation of solute additions such as Si and Be in austenitic stainless steels and nickel binary alloys leads to a loss of swelling resistance of the alloy matrix, as Si and Be are particularly effective in inhibiting void formation [3,11].

A large number of experimental and theoretical studies have been focusing on understanding the mechanism for RIS. On the experimental side, RIS at GB is generally characterized by energy dispersive X-ray spectroscopy (EDS) in a scanning transmission electron microscope (STEM) [12,13]. Using this method, Field et al. have studied the effects of GB structure on the segregation process in Ferritic/Martensitic steels containing 9 wt.% Cr. The results show that enrichment of Cr at lath GBs increases as the misorientation angle increases, which is probably due to the higher sink efficiency of GB of higher angle [13]. Atom probe tomography (APT) is another efficient tool to obtain the three-dimensional distribution of segregated elements. Ni and Si enrichment and Cr depletion have been demonstrated at dislocation loops in 316 austenitic stainless steel based on APT analysis. The result is consistent with previous STEM/EDS observations, although the peak magnitude of the segregated elements are a little higher than those measured by STEM, which may result from a higher spatial resolution of APT [7]. On the theoretical side, rate theory models that solve coupled diffusion

equations of radiation-induced defects and alloy elements were initially developed by Johnson and Lam [5,14], and modified later by Grandjean [15] et al. to include the effects of local concentration on the diffusivities of the alloy species. The key parameters for these models are diffusivities of various defects and reaction coefficients for possible defect reactions (e.g. recombination). Given suitable input parameters, the rate theory model calculations can match the experimental RIS results very well. For example, experiments have showed the element segregation peak at GBs in Fe-20Cr-24Ni increases from 200 °C to 500 °C, which is just as the rate theory predicted [16]. Recently density functional theory (DFT) has been employed to calculate the model parameters [8,17]. Based on concentration-depended defect diffusivities in Ni-Cr alloy from DFT calculations, Barnard et al. showed that the interstitial flux strongly drives Cr enrichment, while the vacancy flux would lead to Cr depletion. The competition between these two fluxes results in a moderate Cr depletion observed in experiments [8].

Despite previous studies have provided important insights in RIS in metallic alloys, much less is known about RIS in ceramic materials. One possible reason is that the idea of using ceramics as cladding materials has been widely accepted only within in recent years. In addition, some technical difficulties delay the investigation progress of RIS in ceramics. For experimental measurement, due to the stronger absorption of lower energy X-ray by the detector window and the specimen itself, EDS only works for heavier elements (Z>10) so electron energy loss spectroscopy (EELS) is necessary to characterize the distribution of light elements like C or O [18]. In APT, a short (a few nanoseconds) voltage pulse is applied to the specimen to ionize the surface atoms. Therefore the inability of samples of low electrical conductivity to transmit the pulses limits the applications of APT to materials only with large enough electrical conductivity [19]. For theoretical analysis, the defect energy landscape is more complex in ceramics than that

in metallic alloys while detailed and accurate knowledge of the defect energy landscape is necessary to construct a reliable model for RIS in ceramics. As mentioned earlier, a throughout understanding of RIS is a critical step to apply grain engineering to optimize the properties of SiC. In addition, recent corrosion experiments have showed that GB in chemical vapor deposited (CVD)-SiC is preferentially dissolved in supercritical water [20,21]. Therefore the knowledge on segregation in SiC can provide basis for further studies on the corrosion process as well.

In this chapter, STEM/EELS have been applied to characterize the evolution of C concentration near GB in SiC at different irradiation temperature and dose. First, the experiment methods, including irradiation, STEM sample preparation and EELS experiment are briefly introduced. Second, the observed temperature-dependent RIS in SiC is discussed. In brief, the CVD-SiC sample shows an intrinsically C-depleted GB. In samples irradiated at 300 °C, the C-depleted region at GB goes away. However, in the sample irradiated at 600 °C, the C concentration at GB becomes even lower and depletion region becomes larger than the non-irradiated sample. This phenomenon has been explained by the rate theory model dealing with defect diffusion and reaction both in the bulk and along GB. Finally, the limitation of current study and possible future research directions are discussed.

3.2 Experiment methods

3.2.1 Sample preparation

The polycrystalline CVD 3C-SiC was sourced from Rohm & Hass with grain sizes ranging from 1 μm to 5 μm. 3.15 MeV C ion irradiation was applied with flux about 4.17×10^{12} ions/cm^{2}s, which corresponded to generating 1 dpa dose at the damage plateau region in 10 hours. One batch sample was irradiated at 300 °C and the other batch at 600 °C. The cross section samples for STEM/EELS analysis were made by attaching two irradiated surfaces face-

to-face using M Bond-610 and wedge polishing followed by ion milling on both sides with Fischione 1050 set at 2 kV for about 30 minutes. Since EELS was applied to measure the relative concentration of C, contamination (mostly hydrocarbon) on the sample surface must be cleaned before the experiment and well-controlled during the EELS acquisition. There are two possible sources of hydrocarbon. One is from the sample preparation process or storage. Hydrocarbon may be introduced during ion milling or by using M bond. The long time storage of samples may also lead to hydrocarbon accumulation on the sample surface, although the sample is stored in pumped desiccators. The contamination may also come from the STEM column, in which the sample holders are frequently switched, so inevitable leakage may cause hydrocarbon attach to the column internal surface. When a clean sample is inserted, the contamination may rapidly transfer from the wall to the sample surface. Based on experimental experiences, the surface contamination can be effectively removed by nano milling a small region of interest (usually 20 μm by 20μm) using Fischion 1040 at 900 V for 30 minutes on both sides of the sample, while the internal wall contamination can be removed by in-column plasma cleaning for 15 minutes. If the sample is contaminated, the brightness of bright field (BF) image in the region hit by the electron beam will decrease after certain amount of time. Therefore an effective criterion to examine whether the sample is clean enough is to focus the beam into a very small field of view (about 1nm by 1nm) for about 10 minutes. If the brightness of the region shows no obvious change, the sample and the STEM column is clean for the following EELS characterization. Fig. 3.1 shows BF image of a clean sample (a) and a contaminated sample (b) after focusing the electron beam for 10 minutes. The black center in Fig. 3.1(b) is introduced by the beam interaction with the surface hydrocarbon as this sample is heavily contaminated. All samples used in this study passed the cleanness test and are free from contamination.

In order to characterize RIS in SiC, we need measure local C concentration as a function of distance to GB. Therefore the electron beam has to be parallel to the GB plane (i.e. GB is edge-on), so the concentration information at different distance to GB is not overlapped. The GB can be tilted to the edge-on position. Usually, if the low index zone of one grain is tilted to be parallel to the electron beam, the GB is very close to edge-on. Fig. 3.2 shows the high resolution STEM image of a typical edge-on GB. The atomic columns or lattice fringes on both side of the grain can be seen clearly and the GB looks sharp. In total, four samples have been analyzed in this study. Two of them are non-irradiated samples. One is irradiated sample at 300 °C and dose is 0.8 dpa. The rest one is irradiated sample at 600 °C and dose is 0.9 dpa. One edge-on GB has identified on each sample, so in total four edge-on GBs have been analyzed.
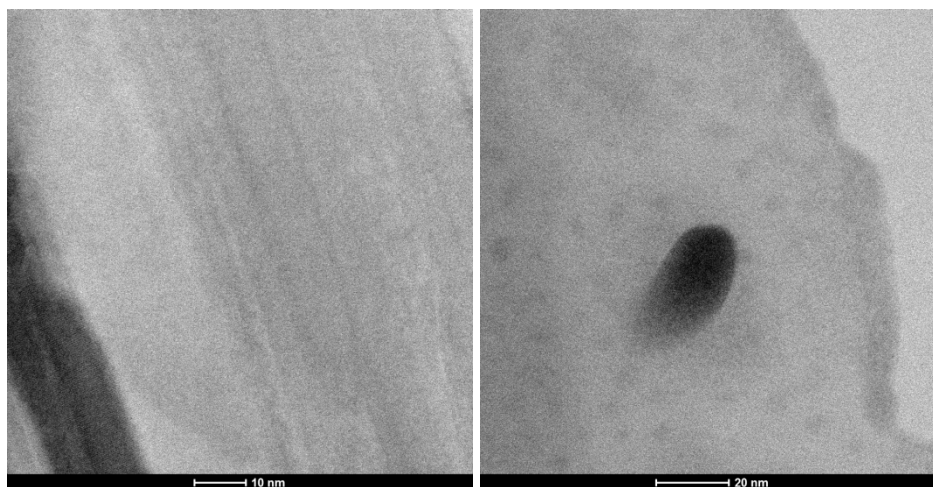
Figure 3.1 *BF image of a clean sample (a) and a contained sample (b) after focusing the electron beam into a small region for 10 minutes.*
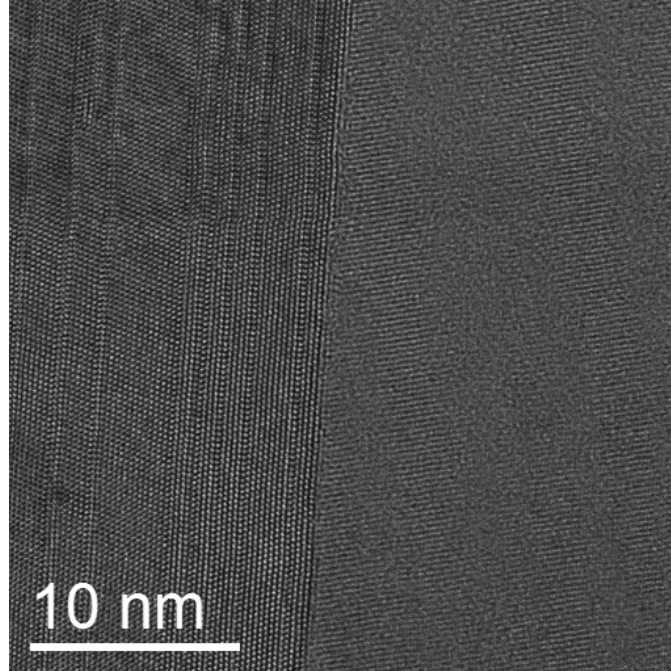
Figure 3.2 *High-resolution image of an edge-on GB*

3.2.2 EELS experiment and data processing

EELS measurements were performed using the Nino UltraSTEM operating at 60 kV at

Oak Ridge National Lab. One non-irradiated sample and one irradiated sample at 300 °C were

also analyzed using the FEI Titan operating at 200 kV at University of Wisconsin-Madison as

backup. In CVD-SiC, the average threshold displacement energy is 38 eV for Si and is 19 eV for

C [22]. In electron irradiation experiments, the maximum recoil energy transferred to an atom

(T_{max}) is given by the following equation [6]

$$T_{max} = \frac{2E(E+2m_0c^2)}{Mc^2} \tag{3.1}$$

Where E is the incident beam energy, m_0 is static electron mass, M is atom mass and c is speed of

light. Based on equation (3.1), under 60 kV electron beam T_{max} for Si is 4.9 eV, for C is 11.6 eV.

Both of the values are below their own threshold displacement energy. If the electron beam is

200 kV, T_{max} for Si is 19 eV. However T_{max} for C is 44 eV, which is larger the threshold energy

of C sublattice so some C Frenkel pairs may be generated by the 200 kV electron beam. However, our experiments found that the C concentration profile measured at 60 kV and 200 kV are almost identical, so the effect of beam energy can be neglected. The detailed comparison is provided latter in section 3.3. For 60 kV STEM, the convergence angle is 30 mrad and collection angle is 48 mrad. For 200 kV STEM, the convergence angle is 24.5 mrad and collection angle is 25.2 mrad.

Once an edge-on GB is identified, spectrum image was taken in a rectangular region (about 20 nm long and 6nm wide, shown as the white box in Fig. 3.3) that is perpendicular to the GB. In order to obtain the C local concentration as a function of distance to GB, the EELS signal from a narrow slot (shown in the shaded region in Fig. 3.3) is summed up. The local concentration is calculated based on the EELS counts in Si peak and C peak, while the distance of the narrow slot to GB is taken as the corresponding distance to GB. The width of the shaded slot is 0.5 nm for EELS taken using 200 kV STEM and less than 0.2 nm for 60 kV, so the spatial resolution of the C concentration profile is less than 0.5 nm.

Fig. 3.4 is a typical EELS obtained in the shaded region. Core loss peak of Si L edge (99 eV) and C K edge (284 eV) can be easily identified in the spectrum. The relative concentration of C atom can be calculated using the following equation [18]

$$C_{carbon} = \frac{N_C}{N_C + N_{Si}} = \frac{I_C \sigma_C}{I_C \sigma_C + I_{Si} \sigma_{Si}} \qquad (3.2)$$

Here C_{carbon} is the relative concentration; N_X represents the absolute atom number of element X in the same region; I_X is the integrated signal counts in the EELS core loss peak while σ_X is the ionization cross section of element X. The cross section for Si and C are from tabulated values based on Hatree-Slater model. As shown in equation 3.1, the uncertainty of relative C concentration C_{carbon} is determined by the uncertainties of integrated peak counts I_{Si} and I_C. As

the detection of inelastic scattered electron is a Poisson process, the peak counts should be high so the uncertainty of C_{carbon} can get small enough. According to calculations based on equations from Ref. [23], if the $I_C > 4.5 \times 10^8$, the theoretical uncertainty of C_{carbon} is less than one percent. All the spectrums in this study have a larger integrated C peak counts than 4.5×10^8. The integrated window is 176 eV-226 eV for Si peak and 324 eV-364 eV for C peak, in order to avoid the fine structures of the EELS where the ionization cross sections are not very accurate. As mentioned earlier, only one edge-on GB was identified in each sample. For each GB, more than five spectrum images were taken in nearby region to make sure the results were repeatable and representative. Spectrum images were also collected in regions at least 20 nm away from GB and the local C concentration in these regions were used as reference values. As the non-irradiated CVD-SiC is stoichiometric and highly pure, the C concentration should be 50% everywhere in the grain interior. Therefore we take the standard deviation of a series of C concentrations measured in the grain as the uncertainty of the measured C concentration near the GB.
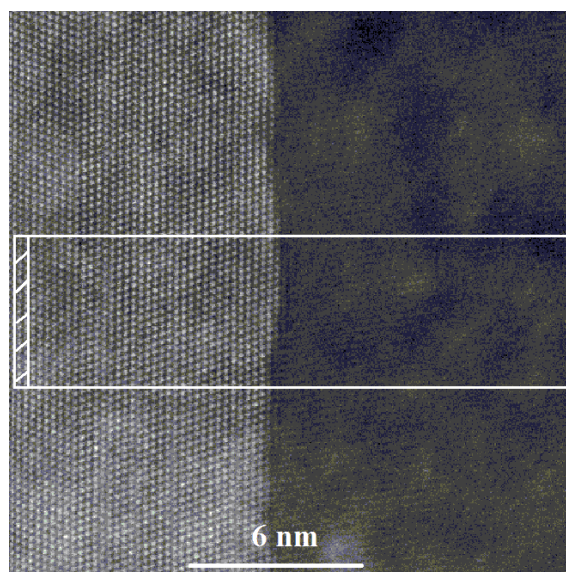
Figure 3.3 High angle annular dark field image of GB. White rectangular box is the region where EELS is taken and shaded slot represent where one local C concentration value is calculated.
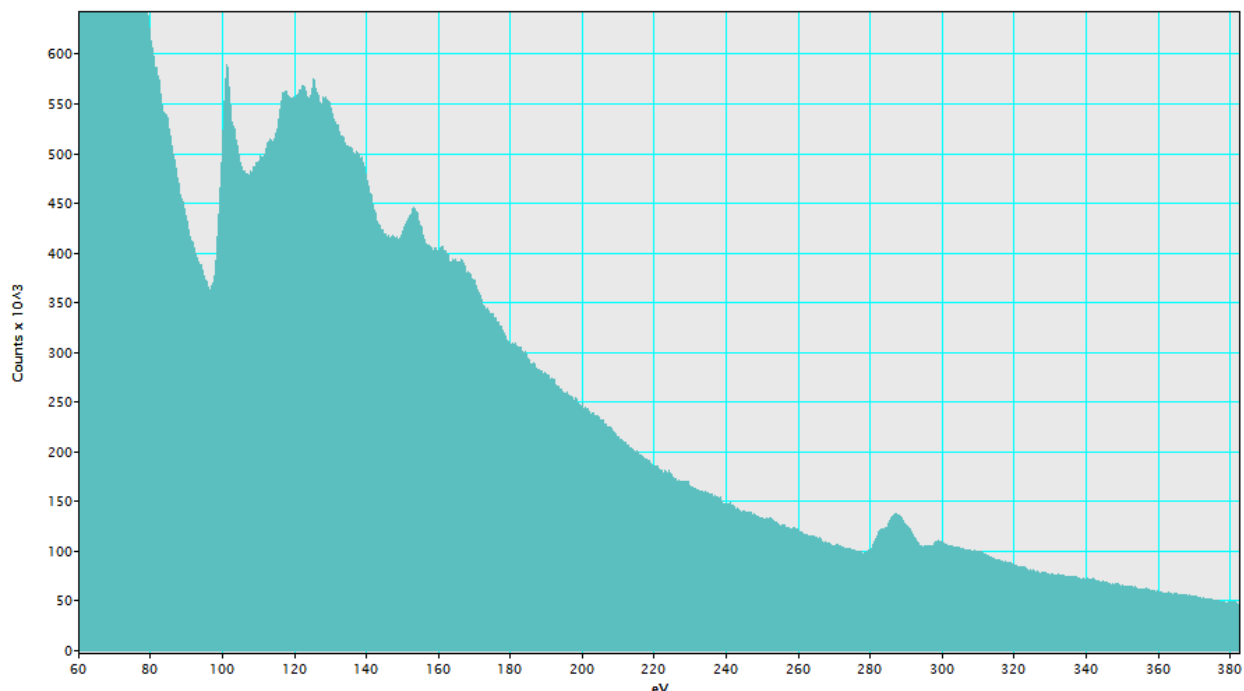
Figure 3.4 Typical SiC EELS from the shaded region in Fig. 3.3. Si L edge is at 99 eV and C K edge is at 284eV

3.3 Evolution of GB composition as a function of irradiation temperature

Fig. 3.5 shows the obtained C relative concentration profile in the non-irradiated SiC samples from both 200 kV and 60 kV EELS measurement. As mentioned earlier, although 200 kV electron beam may produce certain amount of C Frenkel pairs, this effect is negligible according to the profiles measured using both electron beams. Fig. 3.5(a) and Fig. 3.5(b) have very similar C concentration profile, showing that C is depleted right at the GBs. The minimum C concentration is around 45% and the depletion zone is around 1nm. As a comparison, Fig. 3.6 shows the C concentration in the grain interior and it is around 50%. It is worth noting that Fig. 3.5 only shows the relative C concentration, so it is not clear whether the GB is Si enriched or C

depleted. The absolute EELS peak counts in the shaded region as a function of distance to GB are also plotted in Fig. 3.7. Both absolute counts of Si peak and C peak decrease as it gets closer to GB, which indicates the atomic density at GB is lower than that in the grain interior. The ratio of counts at GB over counts in the grain interior for C is $2.40\times10^4/2.80\times10^4$=85.7%, while the value for Si is $9.55\times10^4/1.00\times10^5$=95.5%. Therefore the results clearly show that C is depleted in the non-irradiated CVD-SiC. The depletion might be a result of the chemical vapor deposition process. To the best of our knowledge, the intrinsic C depletion at GB has not been reported in previous literatures.
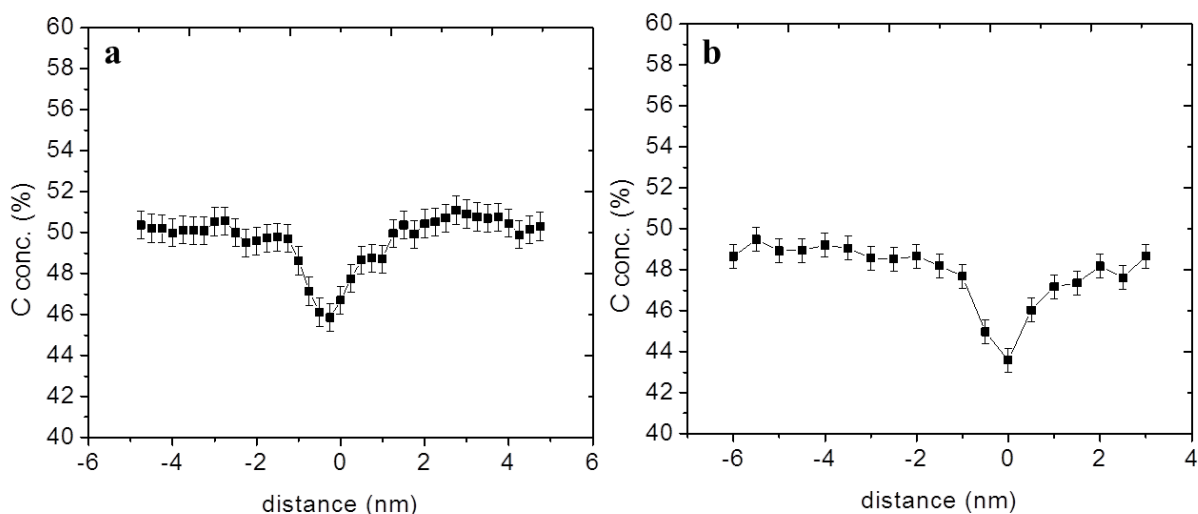
Figure 3.5 *local relative C concentration as a distance to GB in non-irradiated CVD-SiC sample. (a) is from 60 kV EELS measurement and (b)is from 200 kV EELS measurement*
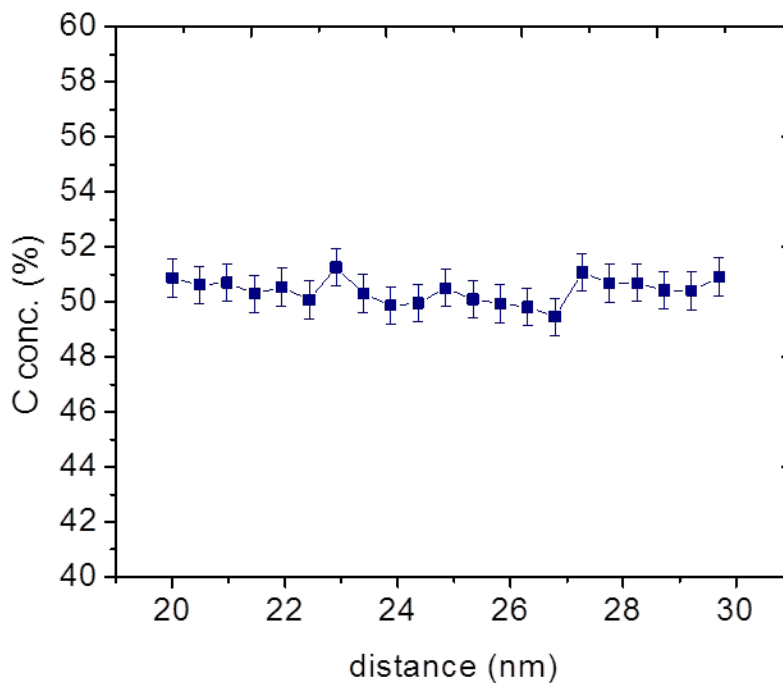
Figure 3.6 local relative C concentration in grain interior in non-irradiated CVD-SiC sample.
(a) is from 60 kV EELS measurement and (b)is from 200 kV EELS measurement
(x-axis is the distance to GB)

Position (nm)   Position (nm)
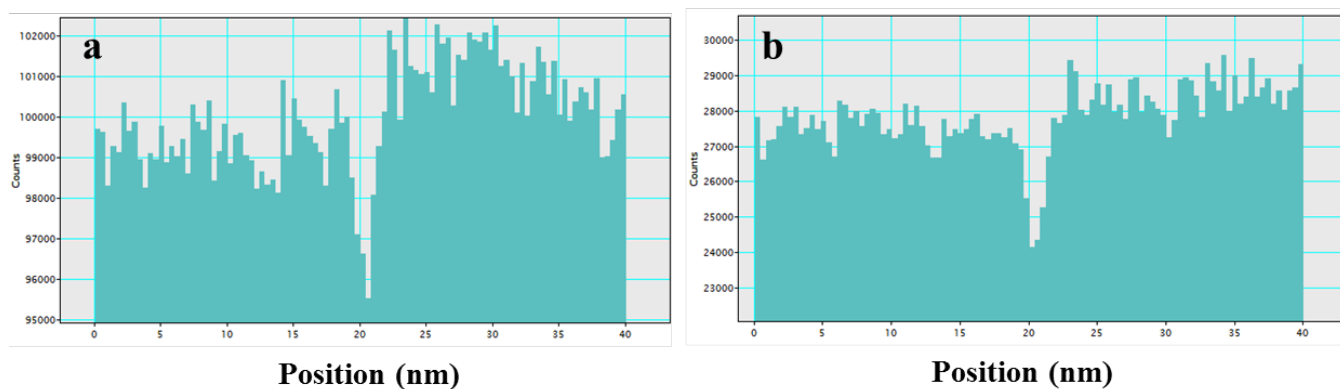
Figure 3.7 absolute counts of (a) Si L peaks and (b) C K peaks in the shaded region as a
function of position. GB is in the middle (around 20 nm)

The C concentration profiles evolve as the sample undergoes irradiation at different temperature. Fig. 3.8 shows a typical C concentration profile in the irradiated sample at 300 °C. No C depletion zone can be found. However, when the sample is irradiated at 600 °C, the C

depletion zone appears again. As shown in Fig. 3.9, the minimum C concentration at GB can be

as low as 32% and the depletion zone width is about 5 nm, which is much larger than that of

non-irradiated samples.
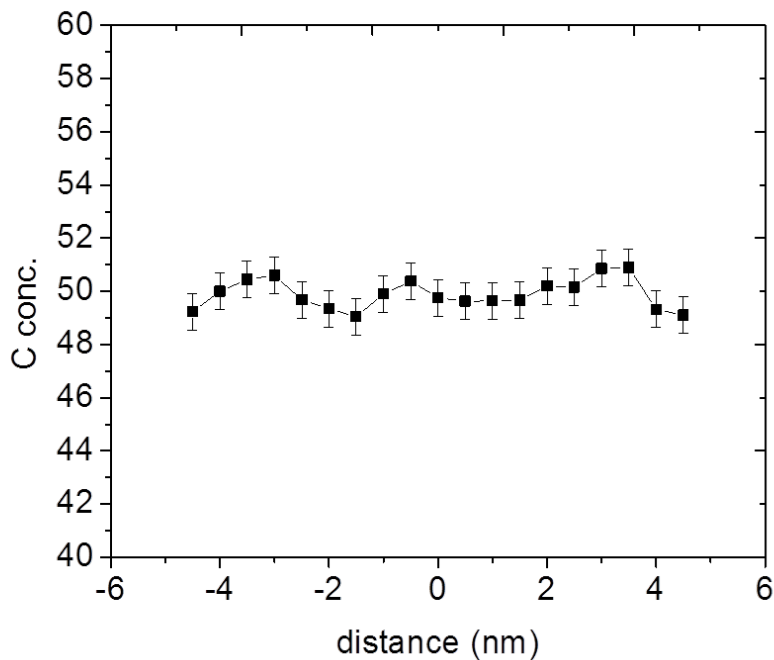
Figure 3.8 *local C concentration profile near GB in the 0.9 dpa irradiated sample at 300 °C*
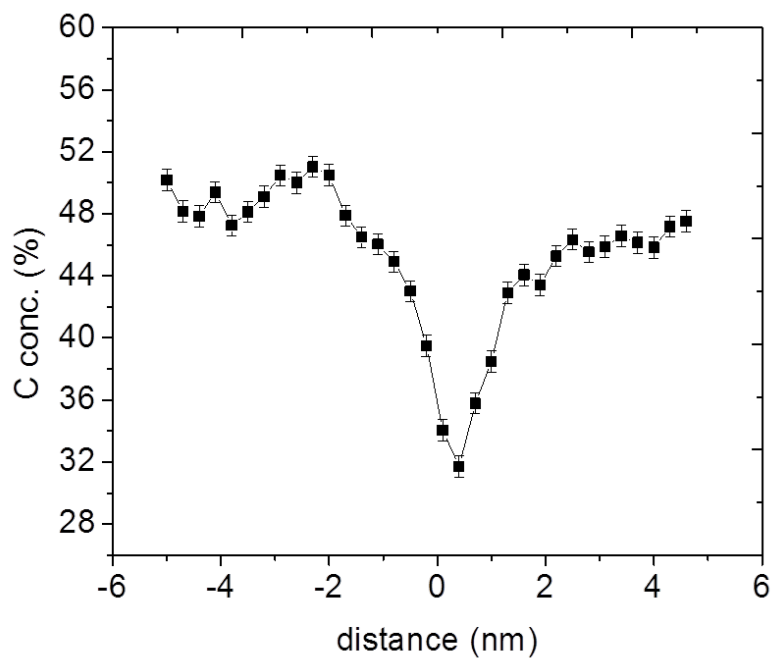
Figure 3.9 *local C concentration profile near GB in the 0.8 dpa irradiated sample at 600 °C (attention the y scale is 28%-60%, not like 40-60% in other concentration profiles)*

According to the experiment results, it seems the intrinsic C depletion at GB disappear after irradiation at 300 °C and then the RIS introduces even large C depletion after irradiation at 600 °C. There is one concern that since the C ion was used as irradiation specie, the implanted C may change GB chemistry. However, the following estimation demonstrates that the number of implanted C is very small when compared to the original C in the sample so this effect is negligible. During the 10 hours irradiation, the total incident C fluence is 1.5×10^{17} ions/cm^2. At 300 °C, the average mean square displacement for C interstitials in SiC is about 319.27 μm [24], so it is reasonable to assume all the implanted C reside in the 1cm×1cm×319.27 μm region. Assuming the SiC grain is cubic with side length equals to 2.5 μm and GB width is 1nm, the total GB volume in the 1cm×1cm×319.27 μm region is 3.83×10^7μm^3. If all the implanted C atoms are concentrated in the GB, the extra C will only be about 8.1% percent of the original number of C atoms in the GB. This amount of C will change the relative C concentration about 1.8%, which is clearly not able to remove the original C depletion. In addition, it is probably true that substantial amount of incident C will not concentrate in the GB region. For irradiation at 600 °C, as the C mean square displacement becomes much higher than 300°C so the effect of incident C is even less. Therefore it is clear that the evolution of C concentration profile is not caused by the implanted C. As shown in Ref. [13], the GB structure may also affect the RIS, so will the different C concentration is due to different GB structures in different samples. Electron beam diffraction has been applied to analyze all the four GBs used in this study. It turned out be that all the GBs are regular high angle GBs (with both tilt and twist), so GB structure does not play a role here.

3.4 Rate theory model for defect kinetics near and at grain boundaries

In chapter 2, a rate-theory model solving defect migration and reaction in grain interiors has been developed and interstitial starvation mechanism has been demonstrated. Due to the net C flux to GBs, the immobile vacancy accumulates and drives the region near GB into amorphous. It is reasonable to expect that the net C flux may also change the local C concentration at GB. A simple diffusion-generation model is developed to estimate the effect of the C flux on the GB C concentration

$$\frac{\partial C(t,x)}{\partial t} = D\nabla C(t,x) + F(t) + G \qquad (3.3)$$

Here $C(t,x)$ is the C interstitial (C_i) concentration along the GB. D is the interstitial diffusivity. $F(t)$ is the external source of C_i, i.e. the C flux to GB due to the interstitial starvation mechanism and G is generation rate of C_i due to ion irradiation (internal source). In current model, we have three major assumptions. First, only C_i flux to GB is considered as the external source. As shown in chapter 2, the low reaction barrier for Si Frenkel pair leads to a fast recombination and the Si flux to GB is much lower than C flux. Second, we assume the defect reaction barriers on GB are similar to those in grain interior. Therefore the fast recombination of Si Frenkel pair would not alter local composition too much and only C is included in current model. Third, based on ref. [25], we assume the defect generation rate at GB is the same as in grain interior. Here $G=2.22\times10^{-6}$ /second. The detailed calculations of G can be found in equation 2.3 of Chapter 2. We set $C(t=0,x)=0$ as initial condition and the initial C concentration is set as 46%. $C(t,x=0)=0$ and $C(t,x=L)=0$ are set as boundary conditions. L=500 nm is the side length of GB. The boundary condition means that there are perfect sinks (such as triple junctions or surfaces) on both sides of GBs

One important parameter for solving the equation is the diffusivity of C interstitial along GB. Effective self-diffusivities of C in CVD-SiC on GB and in grain have been measured by tracing ^{14}C isotope [26]. By fitting the measured diffusivity to Arrhenius equation, we can get the effective migration barrier, which is actually the sum of formation energy and migration energy of C_i. According to ref [26], effect migration barrier is 4.44 eV at GB and 6.31 eV in the grain. Based on DFT calculation, we know the migration energy of C_i in the bulk is 0.67 eV [24]. Based on molecular dynamics simulation, Ci formation energy difference in the bulk and at the GB can be calculated and it is about 2.91 eV. Using all the information, the migration barrier for C_i at GB are estimated as 1.71 eV. This number is consistent with our previous molecular dynamics calculations on Ci diffusion along low angle tile boundaries.

With all these assumptions and parameters, the evolution of C_i at GB is solved and corresponding C concentration are calculated. Fig. 3.10 shows the calculated C concentration at GB after irradiated at 300 °C (0.8 dpa) and 600 °C (0.9 dpa). The model predicts that GB becomes C enriched (75%) at 300 °C and C depleted (37%) at 600 °C. The C concentration at different temperature is determined by two competing processes, i.e. the C_i flux from grain to GB and the diffusion of C_i along GB to stronger skins like triple junctions and surfaces, which are assumed as perfect defect sinks in our model. When temperature is low, the C_i diffusion along GB is slow so the C_i flux will be accumulated at GB and make the originally C-depleted GB become C-enriched. When temperature is high enough and C_i diffusion along GB is activated, the extra C from the flux, as well as the generated C_i are moving to sinks on both side of GB, leading to an even lower C concentration at GB.
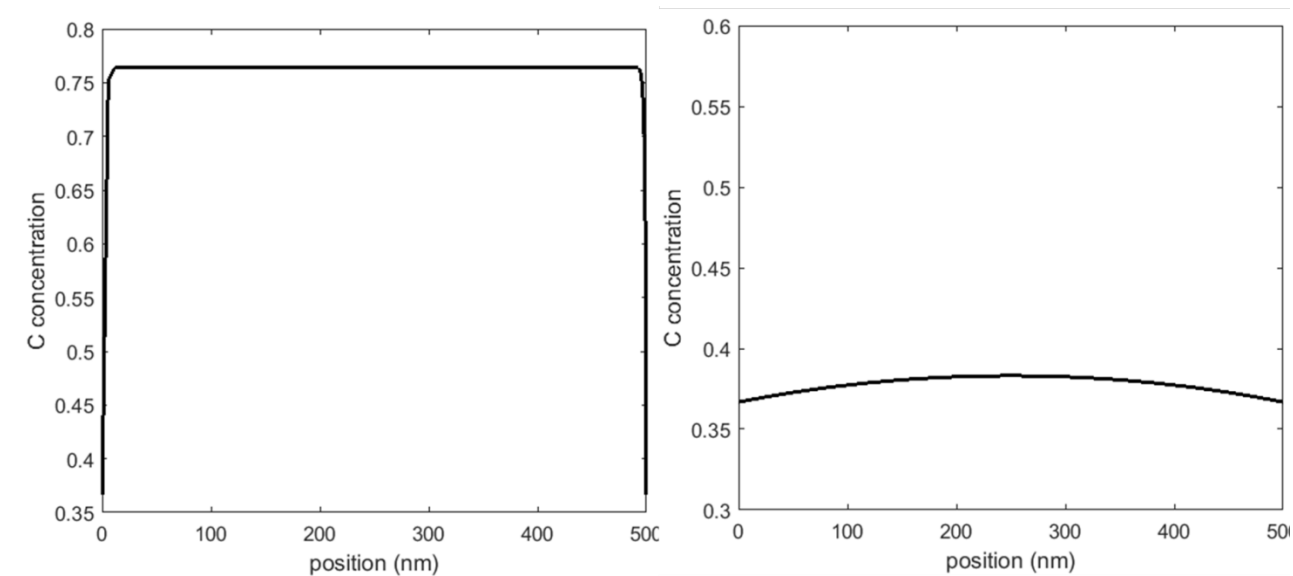
Figure 3.10 *Calculated C concentration profile at GB in samples irradiated at (a) 300 ℃ and (b) 600 ℃ assuming without C_i clustering effect in the grain*

Although the general trend of RIS in the calculation is consistent with experiments, the calculated C concentration at 300 °C is much higher than measured GB concentration at the same irradiation condition (around 50%). One possible source for the discrepancy may come from the flux. For calculating the flux, we assume all the C interstitials in the grain tend to migrate to GB. In fact, both experiment and simulation studies suggest that a large fraction of C interstitials tend to form small interstitial clusters and the mobility of the cluster is also very low [27,28]. The cluster formation may substantially decrease the flux. To test the possible influence of the clustering on the C concentration profile at GB, we used one tenth of the original flux value and reran the model. Fig. 3.11 shows the new C concentration profiles at GB. The C concentration at GB is around 50% in 300 °C irradiated sample and around 37% in 600 °C sample, which matches the experiment result relatively well. The calculation results suggest that to quantitatively model the RIS at GB, more accurate information on C_i clustering in the grain interior is necessary.
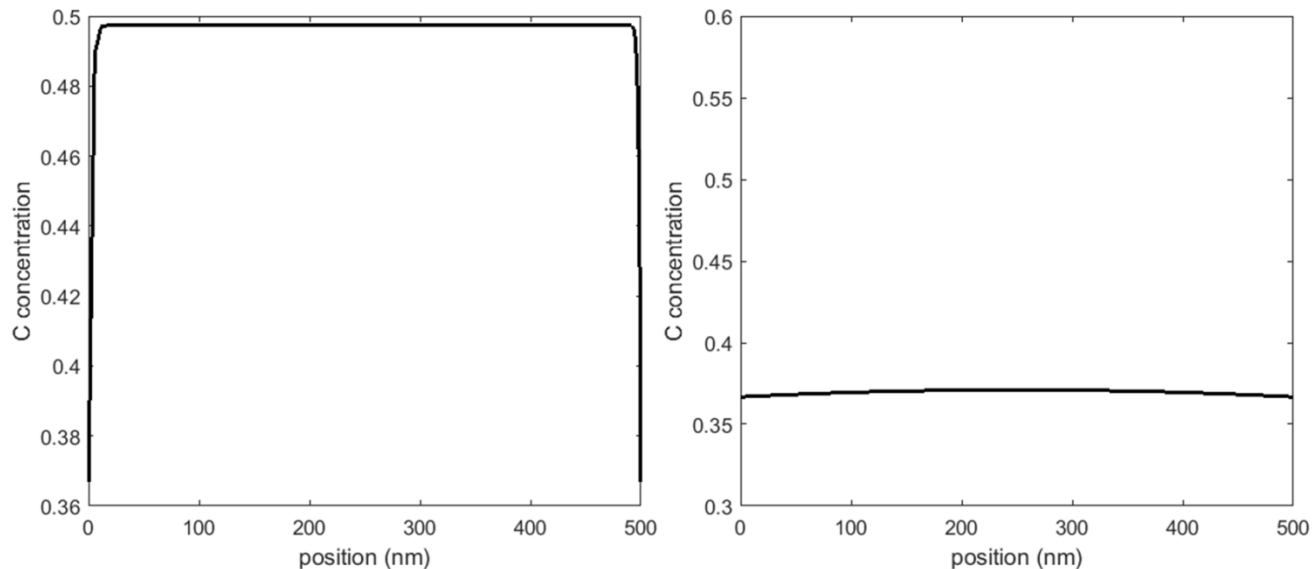
Figure 3.11 *Calculated C concentration profile at GB in samples irradiated at (a) 300 °C and (b) 600 °C assuming with C_i clustering effect in the grain*

3.5 Discussion and conclusion

In this chapter, RIS in irradiated SiC has been studied using STEM/EEL. Results showed that when temperature is low and the C_i diffusion along GB is slow, the C flux from the grain will lead to C enrichment at GB, while when temperature is high enough and the C_i diffusion at GB is activated, the diffusion of C_i to strong sinks on both sides of GB may causes the GB become C depleted. To the best of our knowledge, this is the first time that RIS of constitution elements in ceramic materials is reported. Since the final C concentration profile is a result of a series of synergetic processes (including defect reaction and migration) both in the grain and at GB, characterizing RIS will provide an efficient benchmark to test our current knowledge on defect kinetics in SiC. We also found that CVD-SiC is intrinsically C-depleted. As CVD-SiC has been widely used in various studies and GB can play important roles in determining the materials properties like resistance to corrosion and irradiation, it is worth exploring the effects of a C-depleted GB on these properties in the future.

Bibliography

[1]   L. Jamison, K. Sridharan, S. Shannon, I. Szlufarska, J. Mater. Res. 29 (2014) 2871.

[2]   L.L. Snead, T. Nozawa, Y. Katoh, T.-S. Byun, S. Kondo, D.A. Petti, J. Nucl. Mater. 371 (2007) 329.

[3]   P.R. Okamoto, L.E. Rehn, J. Nucl. Mater. 83 (1979) 2.

[4]   G.S. Was, J.P. Wharry, B. Frisbie, B.D. Wirth, D. Morgan, J.D. Tucker, T.R. Allen, J. Nucl. Mater. 411 (2011) 41.

[5]   H. Wiedersich, P.R. Okamoto, N.Q. Lam, J. Nucl. Mater. 83 (1979) 98.

[6]   G.S. Was, Fundamentals of Radiation Materials Science: Metals and Alloys, Springer, New York, 2007.

[7]   A. Etienne, B. Radiguet, N.J. Cunningham, G.R. Odette, P. Pareige, J. Nucl. Mater. 406 (2010) 244.

[8]   L. Barnard, J.D. Tucker, S. Choudhury, T.R. Allen, D. Morgan, J. Nucl. Mater. 425 (2012) 8.

[9]   S.M. Bruemmer, G.S. Was, J. Nucl. Mater. 216 (1994) 348.

[10]   J.. Busby, G.. Was, E.. Kenik, J. Nucl. Mater. 302 (2002) 20.

[11]   L.E. Rehn, P.R. Okamoto, H. Wiedersich, J. Nucl. Mater. 80 (1979) 172.

[12]   Z. Lu, R.G. Faulkner, G. Was, B.D. Wirth, Scr. Mater. 58 (2008) 878.

[13]   K.G. Field, L.M. Barnard, C.M. Parish, J.T. Busby, D. Morgan, T.R. Allen, J. Nucl. Mater. 435 (2013) 172.

[14]   R.A. Johnson, N.Q. Lam, Phys. Rev. B 13 (1976) 4364.

[15]   Y. Grandjean, P. Bellon, G. Martin, Phys. Rev. B 50 (1994) 4228.

[16]   D.L. Damcott, T.R. Allen, G.S. Was, J. Nucl. Mater. 225 (1995) 97.

[17] S. Choudhury, L. Barnard, J.D. Tucker, T.R. Allen, B.D. Wirth, M. Asta, D. Morgan, J. Nucl. Mater. 411 (2011) 1.

[18] R. Egerton, Electron Energy-Loss Spectroscopy in the Electron Microscope, Springer Science & Business Media, 2011.

[19] K. Stiller, L. Viskari, G. Sundell, F. Liu, M. Thuvander, H.-O. Andrén, D.J. Larson, T. Prosa, D. Reinhard, Oxid. Met. 79 (2012) 227.

[20] J.Y. Park, I.H. Kim, Y. Il Jung, H.G. Kim, D.J. Park, W.J. Kim, J. Nucl. Mater. 443 (2013) 603.

[21] T. Allen, M. Lance, H. Meyer, L. Walker, 318 (2007) 315.

[22] C. Jiang, M.J. Zheng, D. Morgan, I. Szlufarska, Phys. Rev. Lett. 111 (2013) 1.

[23] R.F. Egerton, R. McLeod, F. Wang, M. Malac, Ultramicroscopy 110 (2010) 991.

[24] N. Swaminathan, D. Morgan, I. Szlufarska, Phys. Rev. B - Condens. Matter Mater. Phys. 86 (2012) 1.

[25] N. Swaminathan, P.J. Kamenski, D. Morgan, I. Szlufarska, Acta Mater. 58 (2010) 2843.

[26] M.H. Hon, R.F. Davis, J. Mater. Sci. 14 (1979) 2411.

[27] C. Jiang, D. Morgan, I. Szlufarska, Acta Mater. 62 (2014) 162.

[28] Y. Katoh, N. Hashimoto, S. Kondo, L.L. Snead, a. Kohyama, J. Nucl. Mater. 351 (2006) 228.

4. Effects of surface strain on oxygen adsorption on Zr surfaces

4.1 Current understanding of oxygen adsorption on Zr surface

Zirconium alloys have been widely used as cladding materials for water-cooled reactor because of the low thermal neutron capture cross section and a reasonable corrosion resistance of these materials. However, corrosion is still one of the major reasons for the degradation of Zr alloys during service [1]. Consequently, understanding the oxidation mechanism of zirconium is of great theoretical and technological interest. Investigating the adsorption of oxygen on zirconium surface is the first step towards understanding of initial oxidation kinetics and it is therefore not surprising that a number of studies have been focused on this topic. For example Wang and co-authors [2-4] carried out low-energy electron diffraction (LEED) study on Zr (0001) surface and proposed a so-called double-layer adsorption model. In this model, when the oxygen coverage is 0.5 monolayer (ML) or 1ML, half of the oxygen atoms will occupy the octahedral sites between the first and the second Zr layer while the other half will reside on the octahedral sites between the second and third layer. However, when oxygen coverage increases to 2 ML, it becomes more favorable for half of the O atoms to occupy the surface face-centered cubic sites and the rest to reside on the tetrahedral sites between the first and the second metal layer just above the 2nd Zr layer. On the simulation side, density functional theory (DFT) calculation of Yamamoto *et al.* [5] found that energetically the most favorable sites on Zr(0001) surface are the octahedral sites between the second and the third Zr layer. These calculations were performed with local density approximation (LDA). Interestingly, DFT calculation by two other groups [6, 7] based on the generalized gradient approximation (GGA) suggested that it is the surface face-centered cubic sites that are energetically more stable. The authors of Ref. [7] also proposed a multiple-layer adsorption model. According to this model the most stable

configuration is the one in which O atoms occupy surface face-centered cubic sites and alternate octahedral sites between Zr layers at the same time. The arrangement of O adsorbates in this case is driven by interactions between these atoms, which are repulsive and therefore the atoms prefer to stay as far as possible from each other.

The above studies have provided many key insights into the adsorption process of oxygen on Zr surface, but one important aspect that has not be addressed yet is the effect of stress and strain on the oxygen adsorption. It is known that as the oxide scale grows laterally, a dense zirconia layer is formed on the metal surface [1]. This oxide film, which consists of metastable tetragonal phase and stable monoclinic phase of zirconia [8], acts as a protective layer for zirconium against further corrosion [9, 10]. Due to the lattice mismatch, large planar stress is built up at the metal/oxide interface. The stress is compressive for oxide and tensile for zirconium [9, 11, 12]. This stress (or equivalently strain) is believed to stabilize the metastable tetragonal oxide (t-ZrO_2), modify the chemical reactivity of the interface and thus has a significant impact on the oxidation process [10, 11]. There have been many studies focusing on the strain effect on diffusivity of oxygen ions in Zr-O systems. For example, Barriocanal *et al.* found that the ionic conductivity of yttria stabilized zirconia (YSZ) ultrathin films is enhanced by eight orders of magnitude when the YSZ films are coherently "strained" between SrTiO3 layers at room temperature [13]. Kushima *et al.* performed DFT and Monte Carlo simulations of YSZ with up to 8% tensile strain and found the maximum enhancement in diffusivity was 6.8×10^3 at strain of 4% and 400 K [14]. DFT calculations of Hirschfeld *et al.* have shown that the migration barrier for oxygen ions in cubic ZrO_2 initially increases with compressive strain (up to 9%) and then decreases at high compressive strains (up to 15%) [15]. An increase in migration barriers for compressive strains up to 5% in tetragonal ZrO_2 has also been found in a study based on

empirical potentials and temperature accelerated dynamics [16]. The same author found that for the tensile conditions, migration barrier decreases with up to 1%, but then increases at larger strain. However, the effects of surface strain on oxygen adsorption on zirconium surface have not yet been considered. Here, we report DFT calculations of this effect for the Zr (0001) surface and we demonstrate how strain effect couples to oxygen coverage. We consider compressive and tensile strains up to 6.6%. Tensile strain is expected due to the lattice mismatch between the metal and the oxide, whereas residual compressive strain can be present due to defects and due to stresses exerted on Zr in engineering applications. It is important to point out that under larger compressive strains the hcp Zr will transform to other phases (see section 2) and consideration of the hcp phase in 5.0% ~ 6.6% strain is not physical. However, as we show later in this paper, there is a merit to extending calculations to these large strains because they help elucidate the physical origins of the trends and phenomena observed at smaller strain.

4.2 Simulation methods

DFT calculations are performed with the projected augmented wave (PAW) [17] method and using the Vienna *Ab Initio* Simulation Package (VASP) [18, 19]. GGA is adopted to describe electron exchange and correlation. It is known that LDA shows over-binding for chemical reactions at surfaces, and this effect is largely corrected by GGA [20]. The cut-off energy is 400 eV for plane wave set. During the calculation, atoms are fully relaxed until all forces acting on ions are lower than 0.01 eV/Å. The lattice constants for pure hcp Zr are a=3.233 Å and c=5.181 Å, which we found by fully relaxing the bulk Zr supercell. The calculated lattice constants agree well with previous experiment [21] and DFT calculations [22]. The Zr (0001) surface is modeled by a periodic slab that consists of nine Zr layers separated by a vacuum region, which has a thickness equivalent to that of seven bulk Zr layers (18.134 Å). All the atoms are allowed to

move except the three Zr layers at the bottom. To obtain different oxygen coverages, (2×2), (3×3) and (4×4) surface cells are adopted in the simulation. Here the notation (n×n) means the surface lattice vectors are n-multiples of the basis vectors of the bulk unit cell along the truncated surface. For (2×2), (3×3) and (4×4) surface cells, wave functions are expanded at Γ point in Brillouin zone (BZ) by 9×9×1, 7×7×1, 5×5×1 Monkhorst-Pack k point-meshes, respectively. We also increased the number of Zr layers and number of k-point to make sure that our calculations are converged with current settings.

The geometries of different binding sites for oxygen are shown in Fig. 4.1. We adopt the same notations as in Ref [7]. SFCC means surface face-centered cubic sites. SHCP refers to surface hexagonal close-packed sites. Octaij represents the octahedral sites between i^{th} and j^{th} Zr layer. To avoid artificial dipole moments due to oxygen adsorption on one side of Zr slab in the calculations, dipole corrections were introduced using the IDIPOL tag in VASP [23].

The binding energy E_b of oxygen atom is defined as

$$E_b(\theta) = \frac{E_{total}^{slab}(\theta) - E_{total}^{Zr\ slab}}{N_{oxygen}} - \frac{1}{2}E_{O_2} \qquad (4.1)$$

where θ is the oxygen coverage, defined as the ratio of the number of adsorbed oxygen atoms to the number of Zr atoms in the surface layer. $E_{total}^{slab}(\theta)$ and $E_{total}^{Zr\ slab}$ are the total energies per unit cell of the Zr slab with and without adsorbed oxygen, respectively. N_{oxygen} is the total number of adsorbed oxygen atoms and E_{O_2} is the reference energy of oxygen molecule calculated from DFT. To calculate E_{O_2}, an oxygen dimer was fully relaxed in a cubic box of vacuum with 10 Å side length. The final E_{O_2} energy is -8.76 eV.
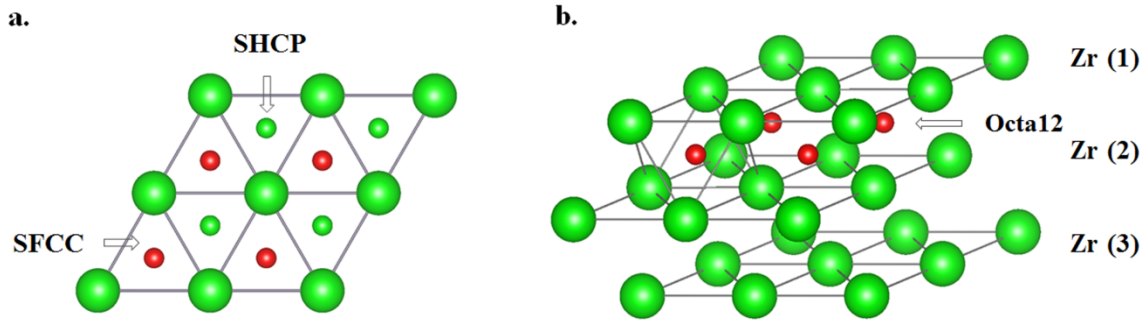
Figure 4.1. *Illustration of different binding sites. (a) Top view of (3×3) supercell. Large green circles represent Zr atoms within the 1ˢᵗ (surface) layer; small red circles represent SFCC oxygen; small green circles represent SHCP oxygen atoms. Zr atoms in the 2ⁿᵈ layer are directly underneath SHCP so they are invisible in this figure. SFCC or SHCP oxygen atoms form an overlayer, which is 2.59 Å (half c) above the Zr surface. (b) Side view of the (3×3) supercell with three Zr layers and Octa12 oxygen atoms. Octahedral sites are located at the center of an octahedron formed by its six nearest Zr neighbors*

In the simulation, biaxial strain is defined as

$$\varepsilon = \ln(\frac{x'}{x}) = \ln(\frac{y'}{y}) \qquad (4.2)$$

where x and y represent the dimensions of the unit cell without strain, and x' and y' are the corresponding dimensions under strained conditions. Both, compressive (defined as negative) and tensile (defined as positive) biaxial strains were applied to the supercell. It should be noted that hcp zirconium metal would transform to other phases under high temperature/pressure conditions. For pressures larger than 5.6 GPa, the hcp (P6₃/mmc) phase is no longer stable and it adopts ω (P6/mmm) phase [24]. Based on the elastic constants of the Zr hcp crystal [22], this stress corresponds to about 5.0% biaxial strain, which is smaller than the maximum strain of 6.6% applied in our simulation. Consequently, only calculations with strains up to 5.0% should be viewed as providing results that can be observed experimentally. All important relative stability changes of different adsorption structures in our calculation occurred within this strain

range. Larger strains in this study are considered to provide insights into the physical origins of the observed phenomena.

The energy calculated from DFT methods corresponds to zero temperature, while the normal operation temperature for zirconium cladding tubes in nuclear reactors is about 300-360 °C [1]. To include the temperature effects, we add a vibrational free energy (G_{vib}) term to the zero-temperature *ab initio* energy in Eq. (1). We assume the vibrational terms of the Zr slab do not change significantly upon insertion of oxygen atoms, and therefore these terms are mostly cancelled when calculating the binding energy. As a result, the main contribution to vibrational free energy comes from oxygen, which changes from the O_2 gas phase to isolated O ions in the Zr solid. Following references [25, 26], the binding energy at temperature T is calculated as

$$E_b(\theta, T) = \frac{E_{total}^{slab}(\theta) - E_{total}^{Zr\ slab}}{N_{oxygen}} - \frac{1}{2}(E_{O_2} + \Delta G_{vib}(O_2, T)) \tag{4.3}$$

Here, we choose the reference temperature $T = 633.15$ K (360 °C) and obtain $\Delta G_{vib}(O_2, T) = -0.92\ eV$. In this notation more negative binding energy indicates a stronger binding.

4.3 Competing effects of surface strain and adsorbate interactions

4.3.1 Analysis on single layer adsorption model

Previous DFT calculations demonstrated that tetrahedral sites between Zr layers are less energetically favorable than octahedral sites [5-7]. Therefore, we mainly focus on the strain effects on the binding energy of octahedral, SFCC and SHCP sites. The oxygen binding energy of different adsorption sites under different strain conditions are summarized in Table 4.1 and Fig. 4.2. At zero strain, the relative stability of different adsorption sites is consistent with previous calculations with GGA [6, 7]. According to Fig. 4.2, E_b becomes more negative, which

means a stronger binding, as the strain changes from compressive to tensile. This trend can be justified based on geometric consideration, as the tensile strain increases the free volume between Zr atoms and provides more space for an interstitial oxygen atom. The opposite is true under compressive strain and therefore it is not surprising that oxygen is less stable under such conditions. However, in terms of the relative stability of specific adsorption sites, there is something more interesting happening when the Zr slab is compressed. The increase of binding energy (to less negative values and therefore to lower stability) is more pronounced for surface sites (SFCC and SHCP) than for bulk sites (Octa23 and Octa34), eventually leading to surface sites becoming less stable at about $\varepsilon=-4.2\%$. This trend is surprising because the spacing between Zr atoms will decrease as compressive strain applied. Since on the surface, O atoms have more freedom to shift toward or away from the surface, one would expect that the effect of compressive strain on surface sites would be smaller than in the bulk where O atoms are confined in all three spatial directions. It is the opposite trend to what we observe in our simulations.
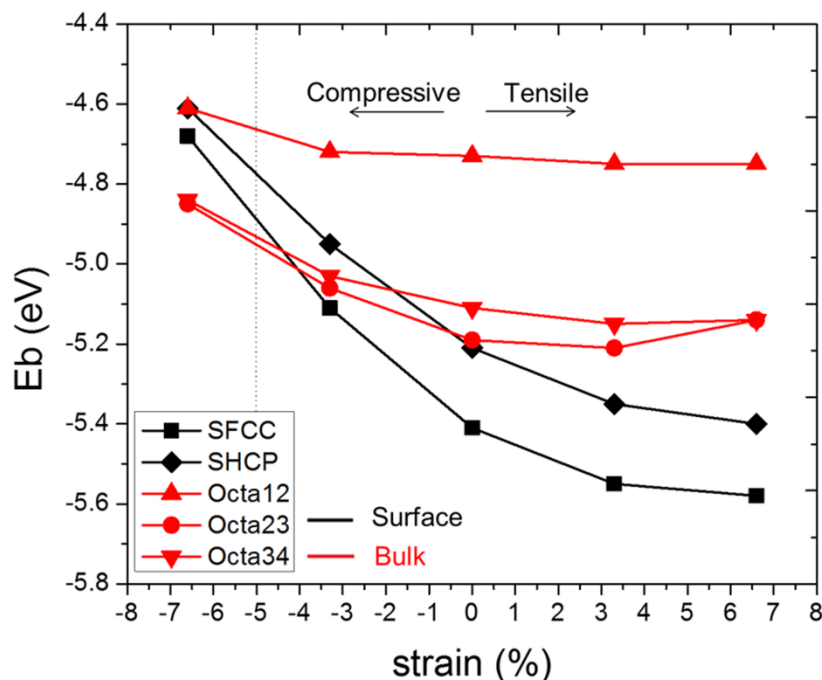
Figure 4.2. *Oxygen binding energy of different binding sites as a function of strain under θ =1 ML surface coverage. The dotted vertical line at -5.0% strain indicates a possible phase transition from hcp to ω phase of Zr.*

Table 4.1 *Oxygen binding energy of different binding sites as a function of strain under θ =1 ML oxygen coverage*

Strain	SFCC	SHCP	Octa12	Octa23	Octa34
-6.6%	-4.68	-4.61	-4.61	-4.85	-4.84
-3.3%	-5.11	-4.95	-4.72	-5.06	-5.03
0.0%	-5.41	-5.21	-4.73	-5.19	-5.11
3.3%	-5.55	-5.35	-4.75	-5.21	-5.15
6.6%	-5.58	-5.40	-4.75	-5.14	-5.14

We hypothesize that the possible origin of the larger stability of bulk sites under compressive strain is interaction between oxygen atoms, which may be different in the bulk and on the surface of the Zr metal. To test this hypothesis, we calculated E_b for different coverage θ for SFCC and Octa23 sites, which we choose as the representatives of adsorption sites on the surface and in the bulk, respectively. The results are summarized in Table 4.2 and Fig. 4.3. As

the data shows, oxygen binding energy decreases as coverage θ changes from high to low, which is consistent with the fact that the interaction between the oxygen adsorbates is repulsive and demonstrates that this interaction plays an important role in adsorption. By comparing binding energies at the same strain, it is clear that the effect of surface coverage on E_b weakens as the coverage becomes small. This effect eventually becomes negligible, as we find binding energies for θ=1/9 ML and θ=1/16 ML to be within 0.05 eV of each other, for both SFCC and Octa23 sites. We can therefore assume that oxygen interaction can be neglected at θ=1/16 ML and only the pure geometric effect of strain on oxygen absorption is left. As shown in Fig. 4.3 by the dashed lines for SFCC and Octa23 sites, under this condition, SFCC (surface) sites would always be more stable than bulk sites, even when under a large compressive strain. In addition, if we calculate $\Delta E = E_b(\varepsilon = -6.6\%) - E_b(\varepsilon = 0.0\%)$ as a measure for the sensitivity to compressive strain at θ=1/16 ML, we obtain that $\Delta E = 0.39$ eV for Octa23, which is bigger than $\Delta E = 0.21$ eV for SFCC. This result implies that Octa23 (bulk) sites are more sensitive to compressive strain than SFCC (surface) site, which is consistent with the intuitive picture that surface sites provide more free volume for O adsorbates than bulk under the same compressive strain and therefore O should be more stable at the surface.

Figure 4.3. *Oxygen binding energy of SFCC (square) and Octa23 (circle) sites with different oxygen coverage θ. The dotted vertical line at -5.0% strain corresponds to a possible phase transition from hcp to ω phase of Zr.*

Based on the above calculations, the change of E_b under general strain conditions can be attributed to two dominant factors: surface strain and adsorbates interactions. When coverage of oxygen is high and large compressive strain is applied, oxygen-oxygen interaction dominates and changes the order of stability of different adsorption sites. On the other hand, when θ is low and oxygen-oxygen interaction could be neglected, E_b will be only affected by the geometry and the availability of free volume for O within the Zr structure.

Since surface sites and bulk sites exhibit different responses to a biaxial strain, it is instructive to discuss in more detail trends observed for the two kinds of adsorption sites. For Octa23 (bulk sites), at low coverage (θ=1/9 ML), E_b increases notably when under compressive strain, but remains relatively constant under tensile conditions. The behavior under tensile

conditions can be understood again by considering free volume available for O interstitials. As tensile strain increases, more interstitial space will be available for oxygen. However, at a certain strain interstitial space between Zr atoms will be sufficiently large for oxygen interstitials so that increasing this space further by strain will no longer have a significant effect on stabilizing the oxygen adsorbates. At an intermediate coverage (θ=1/4 ML), the E_b curve overlaps with the curve of θ=1/9 ML as the strain changes from -6.6% to 3.3%. This trend means that oxygen interactions do not play an important role until the absolute value of the compressive strain ε is larger than 3.3%. At high coverage (θ=1 ML), E_b is always about 0.4 eV larger than E_b at low coverage at the same strain. It implies that adsorbates interactions appears and becomes the dominant contribution at tensile conditions.

For SFCC (surface sites) at low coverage (θ=1/9 ML), E_b decreases almost linearly from strain of -6.6% to +6.6%. As the oxygen coverage increases to θ=1/4 ML, unlike the bulk sites, oxygen interaction begins to have finite values at the lowest compressive strain considered in our study, which is shown by the deviation of E_b curve of θ=1/4 ML from the one of θ=1/9 ML in Fig. 4.3. This onset of the contributions from the O − O interactions occurs earlier than for Octa23, where compressive strain of ε=-3.3% was required to observe a similar effect. At high coverage (θ=1 ML), oxygen interactions appear even under tensile conditions, which is similar to the case of Octa23.

As discussed in preceding paragraphs, when coverage is lower than 1/9 ML, the relation between the binding energy and the strain is entirely dominated by geometric effects (i.e., the availability of free volume). Consequently, we can estimate the contribution from interaction energy E_{O-O} between oxygen atoms to the binding energy, by subtracting E_b at θ=1/16 ML from E_b at a higher oxygen coverage. We also measured the distance between oxygen atoms, d_{O-O},

under different coverage conditions. d_{O-O} are the same (within 0.001 Å) for SFCC and Octa23 when strain and coverage are equal. Therefore, we can plot O-O interaction energy of SFCC and Octa23 sites as a function of O-O distance (see Fig. 4.4). As expected for repulsive interactions, the oxygen interaction energy increases as oxygen distance decreases. In addition, E_{O-O} for SFCC increases much faster than that of Octa23. Again, this analysis shows that oxygen interactions have a larger effect on the adsorption process on surface sites than bulk site, especially when coverage is high. To demonstrate that the aforementioned phenomena and analysis are general and applicable to other binding sites, we also calculate E_b of SHCP (surface) and Octa34 (bulk) for coverage ranging from $\theta=1/4$ ML to 1 ML and with strain within the $\pm 6.6\%$ range. As shown in Fig. 4.5, the results have the same trends as those observed for SFCC vs. Octa23 (Fig. 4.3).
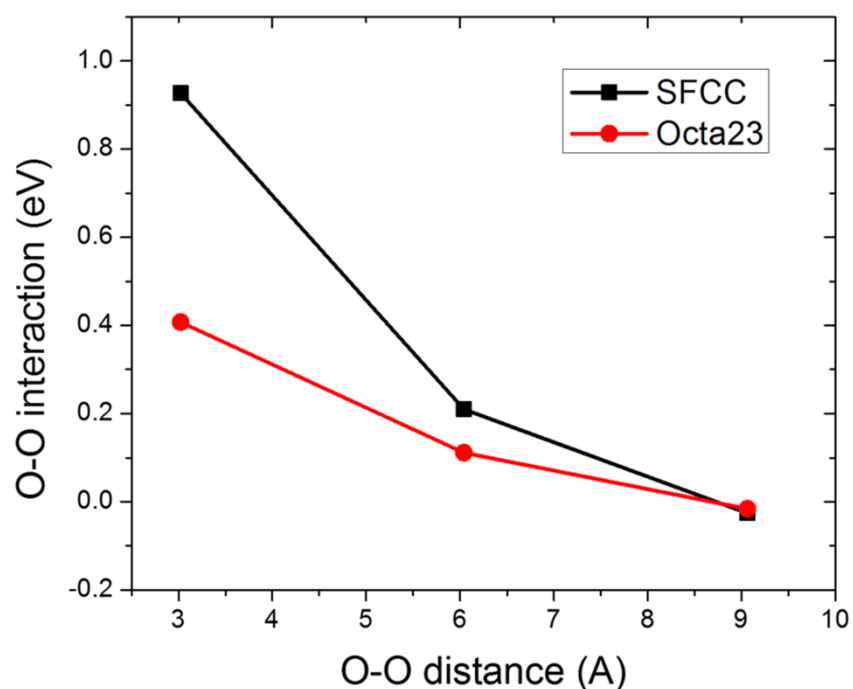
Figure 4.4*. Interaction energy (eV) of oxygen adsorbates as a function of oxygen distance for SFCC (square) sites and Octa23 (circle) sites. The O-O distance of 9.06 Å, 6.04 Å and 3.02 Å corresponds to oxygen coverage of 1/9 ML, 1/4 ML and 1 ML respectively at strain -6.6%.*

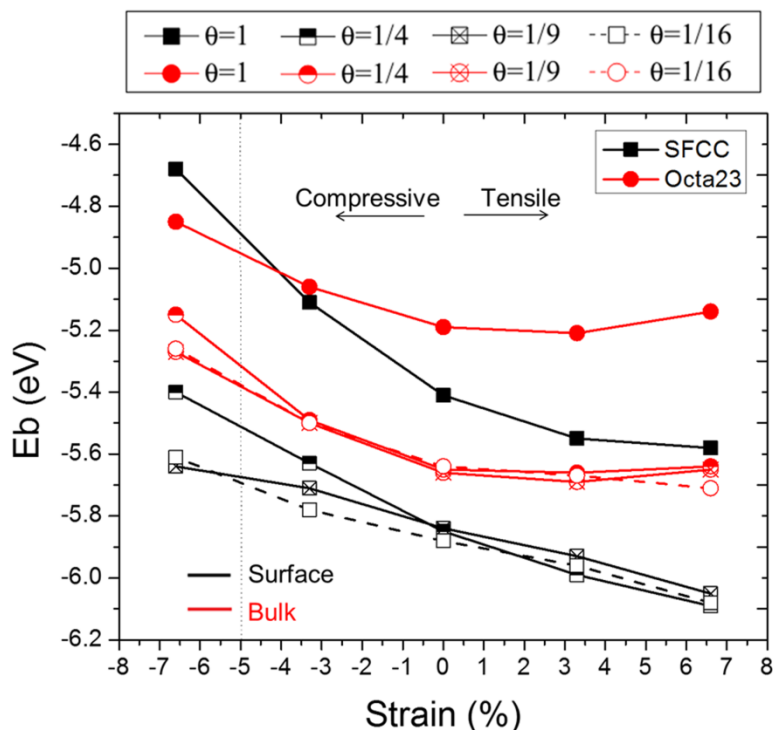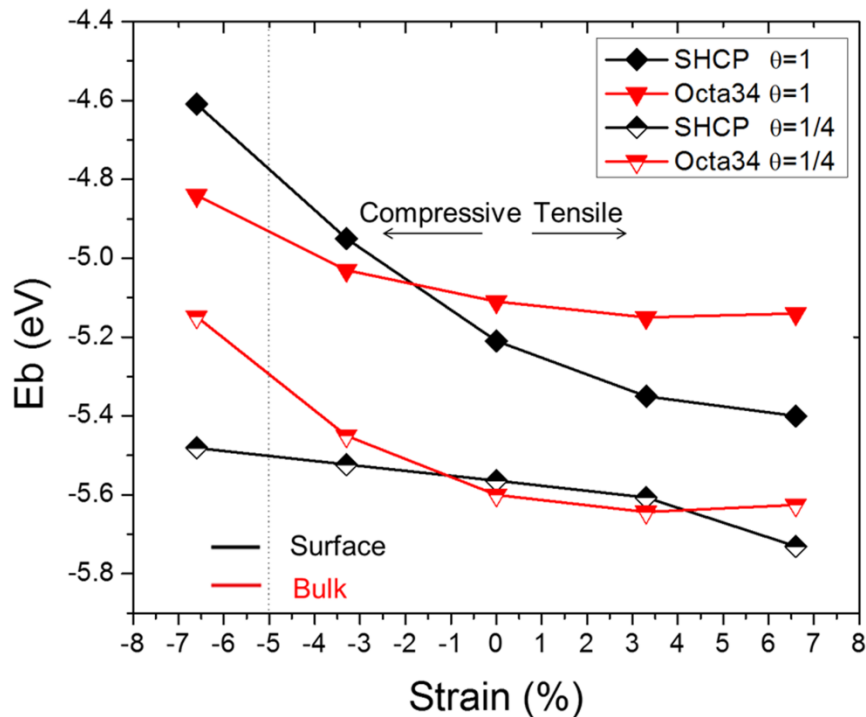***Figure 4.5*** *Oxygen binding energy of SHCP (diamond) and Octa23 (inverted triangle) sites with different oxygen coverage θ. The dotted vertical line at -5.0% strain corresponds to a possible phase transition from hcp to ω phase of Zr.*

It is interesting to ask why oxygen interaction is larger for the surface than for the bulk. The reason might be the different electronic properties of oxygen in these two configurations. For surface adsorption sites (SFCC and SHCP), each oxygen atom has three nearest Zr neighbors and the negative charge around O is partially screened. However, for oxygen atoms on bulks sites, such as Octa23, each oxygen atom is located in the center of the octahedron formed by six nearest zirconium neighbors. As a result, one can expect that in the bulk oxygen charge is more effectively screened by the surrounding metal and the interactions between oxygen adsorbates are therefore weaker than on the surface. A similar difference in screening effects between surface and bulk sites was also reported in (Ga,Mn)As system [27].

It is instructive to consider the impact of surface strain on the early stages of zirconium oxidation. The early oxidation process can be divided into three successive steps. First, oxygen molecules dissociate from the gas phase and bind as monoatomic oxygen to the zirconium surface. Subsequently, as the coverage of oxygen increases, some oxygen ions diffuse as interstitials deeper into the zirconium layers, and finally nucleation of new oxide phases takes places in the near surface region of the Zr metal. In the first stage, since binding energy becomes more negative (indicating stronger adsorption) as the strain changes from compressive to tensile, therefore adsorption of oxygen to zirconium surface would be accelerated under tension and decelerated under compression. The diffusion stage depends on both thermodynamic (i.e., the difference in binding energies) and kinetic (i.e., migration energies) factors. For conditions of large compressive strain and high oxygen coverage, due to the interaction between oxygen adsorbates, surface sites become less stable than bulk sites. This phenomenon provides a strong thermodynamic driving force for oxygen ions to migrate deeper into zirconium. For tensile conditions, surface sites become more stable than bulk sites, so that the thermodynamic driving force for oxygen incorporation is reduced. However, since strain is also likely to affect migration barriers of oxygen in Zr, kinetic effects need to be considered before definitive conclusions can be reached regarding strain effects on oxygen incorporation into Zr. The oxide nucleation stage of Zr oxidation depends on the free energies of the different oxide phases, on the energies of oxide/Zr interface and on the amount of strain introduced into the Zr lattice upon nucleation and the effects of biaxial strain in Zr on these properties remain unknown.

4.3.2 Analysis on multi-layer adsorption model

As discussed in Section 1, both single-layer adsorption model (SLAM) and multiple-layer adsorption model (MLAM) have been proposed in literature. In the latter model, oxygen atoms

can occupy adsorption sites in different layers at the same time, instead of residing in one monolayer. Given the important role of oxygen interactions on adsorption, it is not surprising that oxygen atoms prefer to stay away far from each other and be distributed among different Zr layers. One can ask if this trend will change when Zr is under strain, as considered in our study. Here, we address this question by investigating different structures of MLAM when oxygen coverage is equivalent to 2.0 ML and under compression. We use (2×2) surface cell so 2.0 ML means eight absorbed oxygen atoms. The results are shown in Fig. 4.6. Eight different adsorption structures (SFCC+Octa23, Octa23+Octa45 etc.) were considered. In each structure, oxygen atoms are distributed among the different layers as evenly as possible. For example, SFCC+Octa23+Octa45+Octa67 means that oxygen atoms occupy these four kinds of adsorption sites and there are two oxygen atoms in each layer. Different arrangement of oxygen atoms among possible adsorption sites was tested and the oxygen binding energy of the most stable configuration in each adsorption structure was reported here.

We compare predictions of our simulations to existing experiments. Specifically, the authors of Ref. [4] reported the results of LEED experiments applied to investigate the oxygen adsorption structure for θ=2.0 ML. In these experiments, the diffraction intensity – incident electron energy curve of Zr (0001) surface with 2 ML oxygen was recorded and compared to curves calculated theoretically for thirty plausible adsorption structures. The agreement was quantified using the so-called R_p factor. The lowest value of R_p factor (which means the best match for the experiment data) was found for the structure of SFCC+Tetra12_a2 (tetragonal sites between the first and the second metal layers just above the 2nd Zr layer). This conclusion is seemingly contradictory to our finding that the lowest-energy adsorption site is SFCC+Octa23+Octa45+Octa67. To understand the apparent discrepancy, we calculated the

oxygen binding energy of all three structures from Ref. [4] that had R_p factor lower than 0.400, including the SFCC_Tetra12_a2 structure (see open symbols in Fig. 4.6). At zero strain, the SFCC+Tetra12_a2 has the lowest binding energy among the three structures, which shows that our calculation is consistent with the LEED results. However, the energy of this structure is higher than the energies of the other O arrangements considered in our study and also shown in Fig. 4.6. This is because the authors of Ref. [4] focused on possible adsorption structures that put O atoms into adjacent adsorption layers (such as SFCC+Tetra12_a2, SFCC+Octa12, SFCC+Octa12+Octa23). If, on the other hand, one entire layer of adsorption sites is left empty, as for example in SFCC+Octa23, the distance between O atoms along the direction perpendicular to the surface is increased. Such arrangement reduces the repulsion between oxygen adsorbates and leads to a lower E_b, as shown in Fig. 4.6. Of course, one should keep in mind that the binding energy only indicates the relative thermodynamic stability between different adsorption structures. Kinetically, the migration barrier for oxygen diffusing across Zr layers might be too high, so that oxygen adsorbates may still prefer to stay in the first two adsorption layers (such as SFCC+Tetra12_a2) when the coverage is $\theta=2.0$ ML.
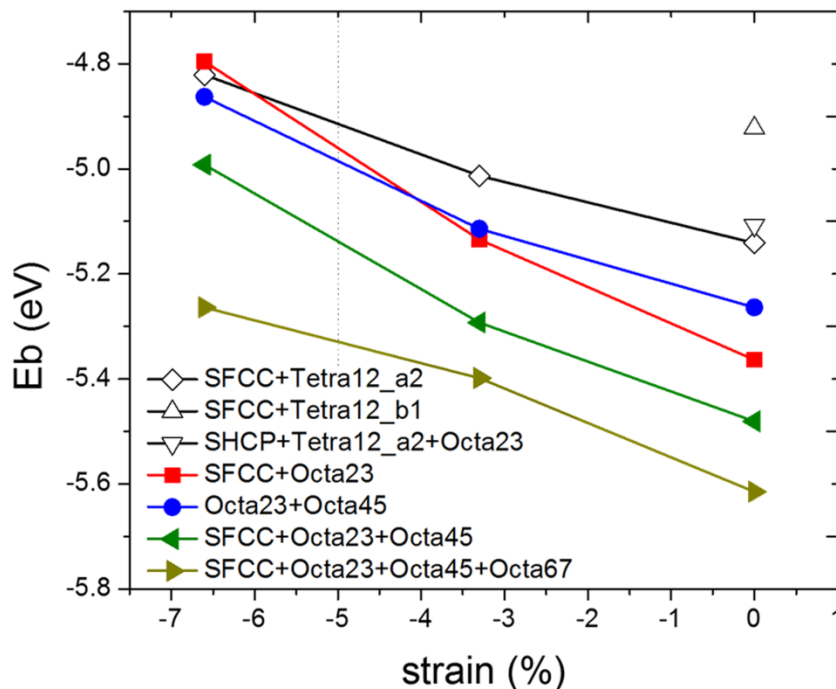
Figure 4.6 *Oxygen binding energy E_b of selected MLAM configurations under compressive and zero strain conditions when oxygen coverage is θ=2.0 ML. The dotted vertical line at -5.0% strain corresponds to a possible phase transition from hcp to ω phase of Zr.*

Similarly as for the SLAM, in MLAM oxygen binding energy is more negative (oxygen becomes more stable) at zero strain than that at compressive strain. We also observe some additional changes in the relative stability between different adsorption sites when a large compressive strain is applied. When ε=0%, surface and near-surface sites (SFCC+Octa23) are more stable than the sites that are away from the surface and deeper in the bulk (Octa23+Octa45). This order changes as compressive strain is applied, which again can be explained by different electron screening for surface and bulk sites (see section 3.2). All of these trends are qualitatively the same as those found by us for the SLAM model discussed earlier. In general, our results show that at any strain condition, the further separated the oxygen ions are from each other within the Zr metal, the more stable the structure will be. Consequently, at the

early stage of oxidation, as more and more oxygen are adsorbed on the Zr surface, some of them will be incorporated into deeper Zr layers.

4.4 Discussion and Conclusion

Ab initio calculation was performed to investigate the oxygen adsorption on strained Zr (0001) surface. Both geometric effects and adsorbate interactions are shown to have important contributions to the changes of oxygen binding energy with strain. At very low coverage of oxygen, bulk sites are more sensitive to surface strain than surface sites. However, when oxygen coverage is high and oxygen interactions become dominant, surface sites become less favorable as binding sites than bulk and therefore compressive strain provides a thermodynamic driving force for oxygen to diffuse into deeper Zr layers. Multi-layer and single-layer adsorption models show similar qualitative trends with strain and these trends can be explained by the same physics.

Bibliography

[1] B. Cox, J. Nucl. Mater. 336 (2005) 331-368.

[2] Y.M. Wang, Y.S. Li, K.A.R. Mitchell, Surf. Sci. 343 (1995) L1167-L1173.

[3] Y.M. Wang, Y.S. Li, K.A.R. Mitchell, Surf. Sci. 342 (1995) 272-280.

[4] Y.M. Wang, Y.S. Li, K.A.R. Mitchell, Surf. Sci. 380 (1997) 540-547.

[5] M. Yamamoto, C.T. Chan, K.M. Ho, S. Naito, Phys. Rev. B 54 (1996) 14111-14120.

[6] G. Jomard, A. Pasturel, Appl. Surf. Sci. 177 (2001) 230-237.

[7] F.H. Wang, S.Y. Liu, J.X. Shang, Y.S. Zhou, Z.Y. Li, J.L. Yang, Surf. Sci. 602 (2008) 2212-2216.

[8] A. Yilmazbayhan, E. Breval, A.T. Motta, R.J. Comstock, J. Nucl. Mater. 349 (2006) 265-281.

[9] M.G. Glavicic, J.A. Szpunar, Y.P. Lin, J. Nucl. Mater. 245 (1997) 147-151.

[10] A.P. Zhilyaev, J.A. Szpunar, J. Nucl. Mater. 264 (1999) 327-332.

[11] H.L. Li, M.G. Glavicic, J.A. Szpunar, Mater. Sci. Eng. A-Struct. Mater. Prop. Microstruct. Process. 366 (2004) 164-174.

[12] H. El Kadiri, Z.N. Utegulov, M. Khafizov, M. Asle Zaeem, M. Mamivand, A.L. Oppedal, K. Enakoutsa, M. Cherkaoui, R.H. Craham, A. Arockiasamy, Acta Mater. 61 (2013) 3923-3935.

[13] J. Garcia-Barriocanal, A. Rivera-Calzada, M. Varela, Z. Sefrioui, E. Iborra, C. Leon, S.J. Pennycook, J. Santamaria, Science 321 (2008) 676-680.

[14] A. Kushima, B. Yildiz, J. Mater. Chem. 20 (2010) 4809-4819.

[15] J.A. Hirschfeld, H. Lustfeld, Phys. Rev. B 84 (2011) 224308.

[16] X.-M. Bai, Computer Studies of Oxygen and Zirconium diffusion in Tetragonal ZrO2, in: Computer Simulation of Radiation Effects in Solids (COSIRES), Santa Fe, New Mexico, 2012.

[17] P.E. Blochl, Phys. Rev. B 50 (1994) 17953-17979.

[18] G. Kresse, J. Furthmuller, Phys. Rev. B 54 (1996) 11169-11186.

[19] G. Kresse, J. Furthmuller, Comp. Mater. Sci 6 (1996) 15-50.

[20] A. Gross, Theoretical surface science : a microscopic perspective, Springer, Berlin ; New York, (2003) pp. 40-43.

[21] A.I. Kolesnikov, A.M. Balagurov, I.O. Bashkin, A.V. Belushkin, E.G. Ponyatovsky, M. Prager, J. Phys. Condens. Mat. 6 (1994) 8977-8988.

[22] B.T. Wang, P. Zhang, H.Y. Liu, W.D. Li, P. Zhang, J. Appl. Phys. 109 (2011) 063514.

[23] L. Bengtsson, Phys. Rev. B 59 (1999) 12301-12304.

[24] D.A. Young, Phase diagrams of the elements, University of California Press, Berkeley, 1991, pp. 170-172.

[25] Y.L. Lee, J. Kleis, J. Rossmeisl, D. Morgan, Phys. Rev. B 80 (2009) 224101.

[26] Y.L. Lee, D. Morgan, Phys. Chem. Chem. Phys. 14 (2012) 290-302.

[27] J. Fujii, M. Sperl, S. Ueda, K. Kobayashi, Y. Yamashita, M. Kobata, P. Torelli, F. Borgatti, M. Utz, C.S. Fadley, A.X. Gray, G. Monaco, C.H. Back, G. van der Laan, G. Panaccione, Phys. Rev. Lett. 107 (2011) 187203.

5. Continuum model for hydrogen pickup through oxide/metal interface

5.1 Introduction to hydrogen pickup and motivation for a predictive model

During the operation of the Zr cladded fuels, hydrogen generated by the water and Zr corrosion reactions permeates through the protective Zr oxide layers, diffuses and accumulates in Zr metal, potentially reaching or surpassing the hydrogen solubility limit in the Zr alloy [1]. This process is called hydrogen (H) pickup and it can lead to the formation of brittle hydrides that can significantly reduce the ductility of Zr alloys [2]. Therefore H pickup is one of the major issues potentially limiting the reliability and durability of cladding materials, especially under high burnups and accident conditions, such as loss-of-cooling accidents and reactivity-initiated accidents [3].

It is usually proposed that H pickup proceeds in three steps [4,5]. First, H_2O molecules adsorbed at the oxide/water interface react with anion oxygen vacancies to leave protons (H^+) on the oxide surface. Second, some of the protons are discharged by electrons migrating from the oxide/metal interface and become H adsorbates (H_{ad}). Subsequently the H_{ad} atom either reacts to form H_2 to be released as hydrogen gas or H_{ad} is absorbed into the oxide. The absorbed hydrogen atoms, possibly along with protons, migrate through the barrier oxide layer and reach the Zr metal surface. Third, due to the H concentration gradient, hydrogen diffuses into Zr metal and at high enough hydrogen concentrations hydride precipitates out. Many studies have focused on understanding the transport of hydrogen through the barrier oxide layer, as this transport is often regarded as the rate-limiting step for H pickup [5–7]. A number of factors, including oxide morphology, alloy additive elements and local stress, play important roles in the transport process. It is widely accepted that the Zr oxide scale has a double-layered structure led by the transition during the oxidation process (or oxide "break-away") [8]. The outer layer is formed by

porous oxide with cracks that provide fast ingress routes for hydrogen, while the inner layer consists of dense oxide and it is usually regarded as a diffusion barrier [8]. Recent TEM analysis found a suboxide (Zr_3O) region existing at the metal/oxide interface in some Zr alloys [9]. According to density functional theory (DFT) calculations, the hydrogen migration energy in the suboxide is higher than that in pure Zr, so this suboxide layer may also slow down the H pickup rate and contribute to the diffusion barrier [10]. Using *in-situ* nuclear reaction analysis, Une *et al.* measured the deuterium concentration depth profile in oxide layers of Zr alloys corroded in D_2O steam [7]. The result shows a nearly flat concentration profile in the outside layer followed by a steeply decreasing concentration in the inner layer, which agrees well with the anticipated higher diffusivity in the porous oxide and lower diffusivity in the dense oxide. Besides oxide morphology, additive elements (e.g., Fe, Cr, Cu, Nb, Sn and Ni) in different Zr alloys have substantial effects on the H pickup fraction. These elements may either behave like trapping sites and directly decrease the hydrogen diffusivity in the oxide [11,12], or they may form second phase precipitates (SPP) that have been hypothesized to be a preferred path for hydrogen migration or a source for formation of pores or cracks [13–15]. Due to lattice mismatch between Zr oxide and metal, high compressive stress is generated in the oxide near interface [16,17]. Raman spectroscopy measurement revealed that the stress varies cyclically and can be as large as several GPa [7]. DFT calculations found that under 1GPa compressive stress hydrogen diffusion coefficient in tetragonal ZrO_2 is only about 60% of the coefficient without stress at 600 K [12]. It is worth noting that there are also literatures arguing that the diffusion of hydrogen through the barrier oxide layer is not the rate-limiting step [18,19]. Evidence from the chemical exchange experiments [14] and TEM analysis [20] suggests that micro pores/cracks exist even in the dense oxide layer. It is suspected that hydrogen can penetrate up to the oxide/metal interface via these

flaws and the hydrogen cathodic reactions at the Zr metal surface is the rate-controlling process for H pickup. One technical difficulty to justify this hypothesis is that the observed crystallite boundary cracks or pores could also be formed during the sample preparations [8]. Therefore it is still debatable on which process is the rate-limiting for H pickup.

Previous studies have provided a number of insights into the detailed mechanism of H pickup and acquired a large body of data under various corrosion conditions. However, few theoretical models have been developed that take advantage of the accumulated knowledge to describe the overall H pickup process quantitatively. In particular, the accuracy for predicting H pickup has not been assessed for even what might be considered the simplest model, which is one that assumes only a rate limiting process of diffusion in the oxide barrier layer. In this chapter we have therefore developed and assessed such a model. This type of a model is important as a baseline for more complex models that invoke additional phenomena, e.g., rate limiting surface reaction processes, SPP, crack and pore formation, strain effects, etc. Using up-to-date diffusivity and oxidation measurements, H pickup fractions (f_H) in six different alloys (Zry-2, GNF-Ziron, VB, Zry-4, ZIRLO and Zr-2.5Nb) were calculated using the model and compared with the experimentally measured f_H [7,21]. Here f_H is defined as the fraction of hydrogen absorbed by the Zr metal to the total hydrogen generated during corrosion. f_H has been widely used for comparing resistances of various Zr alloys to the H uptake under different corrosion conditions (e.g., temperature, corrosion solution) [7,21]. The alloys are chosen to include all alloys and data available in the literature of which we are aware and for which the necessary data on H diffusivity, time-depended weight gain, and f_H needed by the model for comparing reason are simultaneously available. In this study, corrosions in 360 °C pure water (for Zry-4, ZIRLO and Zr-2.5Nb), 400 °C steam and 290 °C LiOH-containing water (for Zry-2,

GNF-Ziron and VB) were analyzed. In Ref. [21], the samples of Zry-4 and ZIRLO were processed in both sheet and tube form in order to test whether the sample geometry could affect the H pickup fraction. These data are also included and compared in this chapter. Previous investigations have confirmed that the H pickup rate is significantly accelerated by the LiOH addition to water environment [22]. Further TEM analysis discovered that extended networks of degraded grain boundaries were formed from the oxide surface to near the metal/oxide interface, probably due to the preferential dissolution of zirconia in LiOH solution [7]. Therefore the H pickup process is controlled by dissociation reaction rate of H_2O at the front of the degraded grain boundaries, rather than the hydrogen diffusion process. Including the LiOH case aims at showing the limitation of current model and indicating possible improvement for future work.

5.2 Development of continuum model

In our model, hydrogen diffusion through the dense barrier oxide layer is taken as the rate-limiting step for H pickup [5–7]. The hydrogen diffusion follows equation

$$\frac{\partial C_H^{ZrO_2}}{\partial t} = D_H \frac{\partial^2 C_H^{ZrO_2}}{\partial x^2}, \left(0 \leq x \leq L_b(t)\right) \tag{5.1}$$

Here $C_H^{ZrO_2}$ is the hydrogen concentration in the barrier oxide layer and D_H is the hydrogen diffusion coefficient. As mentioned earlier, alloy additives have substantial effects on the H diffusivity in Zr oxides so it is not surprising that the measured D_H for different Zr alloys can vary significantly. Even for one Zr alloy, the reported D_H has a relatively large variation (for Zry-2 and Zr-2.5Nb, the variation can be as large as 2-3 orders of magnitude). In the calculation, we choose the D_H for a specific Zr alloy that is closest to the averaged D_H among all the Zr alloys. The chosen D_H of the six Zr alloys being studied here, under three corrosion conditions, are summarized in Table 5.1 [11,23–26]. The effect of different D_H values on the final calculated H pickup fraction is analyzed in the result and discussion section.

In equation (5.1), $L_b(t)$ is the time-dependent thickness of the barrier oxide layer. In order to solve the model, this value must accessible at all times as an analytical function since Eq. (1) must be evaluated at many time steps during the numerical solution. Therefore, we need fit an analytical form for $L_b(t)$. It is difficult to directly measure the oxide thickness during the corrosion process as periodically some part of the alloy specimen must be taken out of the autoclave and studied, typically by electron microscopy. Instead, weight gain (wg, in mg/dm^2) of the specimen as a function of corrosion time is usually reported in literature [18,19,21]. The weight gain can be related to the oxide thickness based on the overall corrosion reaction $Zr + 2H_2O \rightarrow ZrO_2 + 2H_2$, and the assumptions that the weight gain arises only from the added oxygen, the contribution from H adsorption is negligible, and the oxide has a uniform thickness. With these assumptions, the time-dependent oxide thickness $L(t)$ (including the protective barrier oxide layer $L_b(t)$ and the non-protective, porous layer) can be calculated using the following equation

$$L(t) = \frac{m_{ZrO_2}}{m_{O_2}} \frac{wg(t)}{\rho_{ZrO_2}} \tag{5.2}$$

where m_X is the molar mass of chemical X and ρ_{ZrO2} is the zirconia density (5.68 g/cm^3). For diffusion controlled growth, the oxidation kinetics follows a power law yielding[27,28]

$$wg(t) = Kt^q \tag{5.3}$$

By fitting a series of wgs measured at certain times before the oxidation transition [7,21] using the power law, the parameters K and q in equation (5.4) are obtained for all six alloys being studied here under steam or water corrosion, then the $L(t)$ before the transition can be calculated. For the corrosion in LiOH-containing water, as the surface reaction is the controlling process, the wg vs. time follows a simple linear relationship so q is set equal to one and only K is fitted. The fitted coefficients are summarized in Table 5.1. K has in the same unit as wg (mg/dm^2) and q is a

numerical factor corresponding to time in days. More specifically, the data for fitting K and q for Zry-2, VB and GNF-Ziron are from ref. [7], for Zry-2, ZIRLO and Zr-2.5Nb are from ref. [21]. As mentioned earlier, the protective barrier oxide layer thickness ($L_b(t)$) is not the only contribution of the entire oxide layer thickness $L(t)$. To determine L_b, nuclear reaction analysis was used to measure the deuterium concentration profiles in the oxide layer of Zry-2, GNF-Ziron and VB corroded in 400 °C D_2O steam before the transition [11]. In the concentration profile, the region of a flat deuterium concentration is regarded as corresponding to the porous layer and the region of a decreasing concentration is regarded as being due to the dense and protective oxide layer [7,11]. A large number of theoretical and experimental analyses suggests that the oxide undergoes a transition during growth when the barrier oxide layer stops growing, and porous oxide with significant cracks and pores starts to form, and consequently the dense oxide has a maximum thickness L_{bm} [7–9,29,30]. Therefore it is assumed here that during the initial phase of the oxidation, the barrier oxide layer grows with a constant thickness fraction (η) of the entire oxide layer, but that after the maximum thickness is reached, only porous oxide continues growing., The constant η is equal to the ratio of barrier to total oxide thickness at a given time. This assumption is consistent with the fact that a thicker oxide layer is usually associated with a better resistance to oxidation and H pickup [31]. With all these assumptions, we get $L_b(t)=\eta L(t)$ when L_b is smaller than L_{bm} and $L_b(t)=L_{bm}=\eta L(t_{transition})$ afterwards, i.e., $L_b(t) = \min(\eta L(t), \eta L(t_{transition}))$. Here $t_{transition}$ is the time when the oxidation transition happens, which is taken from experiment and indicated by the sudden increase of the oxidation rate shown in the weight gain-time curve [7,21]. The values of L_{bm} and η for Zry-2, GNF-Ziron and VB from Ref. [7] are listed in Table 5.1. For Zry-4, ZIRLO and Zr-2.5Nb, the values of L_{bm} and η are not reported and only the entire oxide thickness at the transition has been calculated in Ref. [21].

Here a simple assumption is made that the fractions η for these three alloys are equal to the average value of 0.57 of the other three Zr alloys in Ref. [7]. The calculated L_{bm} for Zry-4, ZIRLO and Zr-2.5Nb are also listed in Table 5.1. For corrosion in LiOH, it has been demonstrated that the dense oxide layer is very thin or even does not form at all [7,11]. However, with the goal of comparing with the steam corrosion results, here we use the entire oxide layer thickness $L(t)$ for the H diffusion calculation. The failure of our model to explain the LiOH data both supports the model by showing it fails for systems where it does not include the correct physics and supports the hypothesis that little or no dense oxide exists in the LiOH system.

In order to solve equation (5.1), boundary conditions at the H_2O/oxide interface ($x=0$) and oxide/metal interface ($x=L_b(t)$) must be set. As the hydrogen diffusion is assumed to be the rate-limiting step, the hydrogen chemical potentials (μ_H) on both sides of each interface are treated as equal. Under the equilibrium condition across the interface, the boundary conditions are

$$C_H^{ZrO_2}(x = 0, t) = C_{H,1atm}^{ZrO_2}\sqrt{p_{H_2}} \tag{5.4}$$

$$C_H^{ZrO_2}(x = L_d, t) = \frac{\rho_{ZrO_2}}{\rho_{Zr}} C_H^{Zr}(t) \tag{5.5}$$

where $C_{H,1atm}^{ZrO_2}$ is the hydrogen solubility in zirconia at standard atmospheric pressure and p_{H_2} is the H_2 partial pressure just outside the oxide. All concentrations in this work are given as a mole fraction of the host unless stated otherwise. The equation (5.4) simply follows the classic Sievert's law and both equations (5.4) and (5.5) assume ideal-mixing behavior of the dissolved hydrogen in ZrO_2 and Zr, respectively. According to Ref. [32], $C_{H,1atm}^{ZrO_2}$ (unit: mol H/mol ZrO_2) equals to 2.78×10^{-4} at 400 °C, 3.80×10^{-4} at 360 °C and 7.29×10^{-4} at 290 °C. Currently no experimental data about the time-dependent p_{H_2} is available, so we hypothesize that the H_2 partial pressure is a single constant during the corrosion reactions for all Zr alloys corroded by

steam or pure water. The value of p_{H_2} is fitted by minimizing the sum of the squares of the calculation error (defined as difference between the calculated f_H and the measured f_H). The fitted p_{H_2} value is equal to 2.75×10^6 atm. It is worth mentioning that the p_{H_2} is only an effective pressure that represents the activity of the H for entering the oxide, and increasing or decreasing the p_{H_2} value only makes the total calculation errors larger, but does not change the trend of the calculated f_H on which our conclusions are based. Similar fitting has been performed for corrosion in LiOH and the fitted p_{H_2} equals to 2.54×10^7 atm. In equation (5), C_H^{Zr} is the time-dependent hydrogen concentration in Zr alloy, which can be calculated using the equation

$$C_H^{Zr}(t) = C_{H,0}^{Zr} + \frac{\rho_{Zr}}{d \times \rho_{ZrO_2}} \int_0^t D \left. \frac{\partial C_H^{ZrO_2}}{\partial x} \right|_{x=L_b} dt \tag{5.6}$$

where d is the thickness of the Zr cladding, which is 600 μm for Zry-2, GNF-Ziron and VB [7], and 800 μm for the remaining three alloys according to the real sample size [21]. The first term in equation (5.6) is the intrinsic initial hydrogen concentration in the alloy and the second term represents the accumulated hydrogen due to the H flux from oxide into metal. Equation (5.6) assumes that no hydride precipitation occurs, which is consistent with the concentrations obtained as a result of calculations based on our model. Based on Ref. [11,21], $C_{H,0}^{Zr}$ is 9 weight ppm for both Zry-2 and VB, 6 weight ppm for GNF-Ziron and about 12.5 ppm for the remaining three alloys. For initial conditions, we take $C_H^{ZrO_2} = C_{H,1atm}^{ZrO_2} \sqrt{p_{H_2}}$ for $x=0$ and $C_H^{ZrO_2} = \frac{\rho_{ZrO_2}}{\rho_{Zr}} C_{H,0}^{Zr}$ for $0 < x \leq L_b$, which equations fulfill the equilibrium condition for hydrogen chemical potentials at the water/oxide and oxide/alloy interface, respectively. With the boundary and initial conditions, the time evolution of the hydrogen concentration profile in zirconia is solved using the standard finite difference method implemented by us in Matlab. Based on the obtained hydrogen concentration in Zr, the H pickup fraction is calculated using the following equation

$$f_H^{cal}(t) = \frac{[c_H^{Zr}(t) - c_H^{Zr}(t=0)]}{wg_{exp}(t)} \times \frac{d\rho_{ZrO_2}m_{O_2}}{m_{ZrO_2}} \tag{5.7}$$

Here $wg_{exp}(t)$ is the experimentally measured weight gain at time t. Note that oxide pickup fraction in equation (5.7) is always measured with respect to an experimentally measured weight gain. The power law expression in equation (5.4) for the weight gain is not used in equation. (5.7) and is only used to estimate the barrier layer thickness in equation (5.2). The time-depended f_H calculated by our model is then compared with the experimentally measured f_H values at the same point in time during the oxidation process. In the experiments, first the H concentrations is measured in the Zr alloys at a certain corrosion time by either the vacuum hot extraction method or cold neutron prompt gamma activation analysis. Subsequently the H concentrations are converted into the H pickup fractions with the weight gain measured at the same time during the corrosion process [7,21].

Table 5.1 Input parameters for solving hydrogen diffusion in Zr oxide layer

	alloy	D (m^2/s)	K (mg/dm^2)	q	L_{bm} (μm)	η
360°C	Zry-4	4.49×10^{-19}[24]	8.61	0.29	1.2	0.57
water	ZIRLO	$4.49 \times 10^{-19*}$	6.02	0.41	1.7	057
	Zr-2.5 Nb	1.81×10^{-19}[26]	7.15	0.38	2.0	0.57
steam at	Zry-2	3.37×10^{-18}[23]	9.58	0.39	0.9	0.60
400 °C	GNF-Ziron	2.16×10^{-18}[11]	12.10	0.31	0.9	0.53
	VB	8.90×10^{-19}[11]	8.36	0.38	0.8	0.57
LiOH at	Zry-2	1.50×10^{-17}[25]	16.26	1.00	1.4	1.00
290 °C	GNF-Ziron	1.08×10^{-17}[25]	17.81	1.00	1.4	1.00
	VB	1.19×10^{-17}[25]	18.71	1.00	1.4	1.00

Note: no reliable data for H diffusivity in ZIRLO oxide is available that we could find so the H diffusivity in Zry-4 oxide is used for ZIRLO because of similarities in composition (Zry-4: 1.45 Sn-0.2 Fe-0.1 Cr, ZIRLO: 1.0 Nb-1.0 Sn-0.1 Fe.)

5.3 Comparison between simulated and experimentally observed H pickup ration
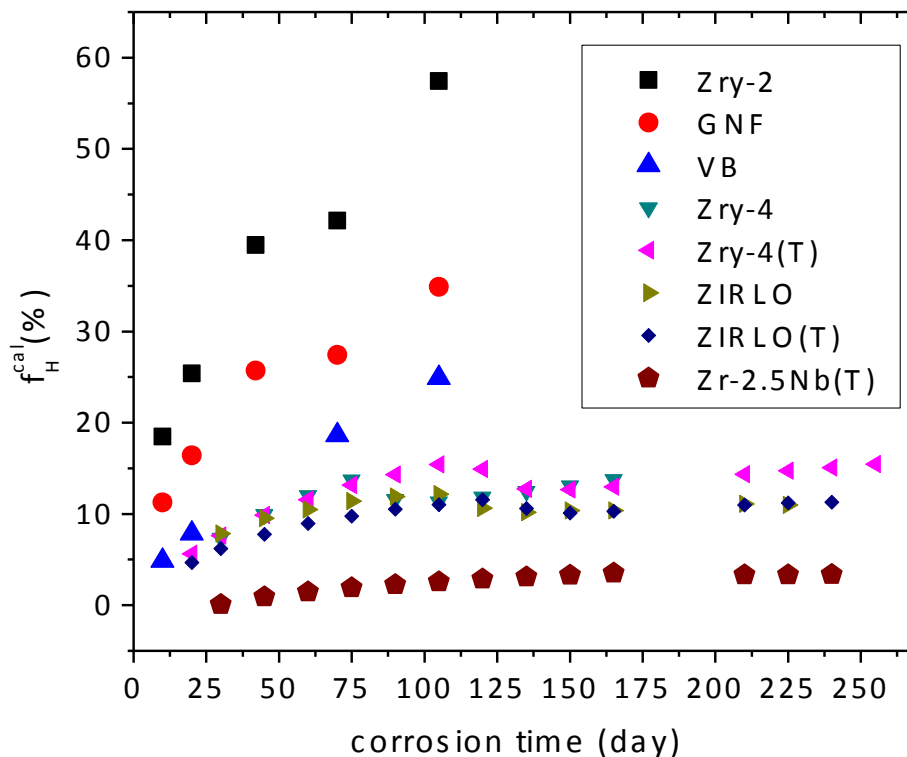
Figure 5.1 *Calculated f_H vs. time under steam/water corrosion conditions. The letter (T) after the Zr alloy name means that the data was obtained from the tube sample, otherwise the data was obtained from sheet sample.*

Fig 5.1 shows the calculated time-dependent H pickup fractions of all Zr alloys corroded in 400 °C steam or 360 °C water. In general, the pickup fractions increase with the corrosion time, which trend agrees with the experimental observations. One exception is that for Zry-4 and ZIRLO, the f_H has a slight but sharp decrease during the transition time (90 days for Zry-4 sheet, 120 days for ZIRLO sheet and 135 days for both Zry-4 tube and ZIRLO tube samples) and f_H values for these alloys resume increasing afterwards. The sudden decrease is due to the fact that the oxidation rate, as well as the H generation rate, is suddenly accelerated at the oxidation transition. The same effect of the oxidation transition has also been observed in the experimentally measured H pickup fractions for these alloys, although the decrease is not as

obvious as in the model and only a plateau of f_H appears around the oxide "break-away" time [21]. For Zry-2, GNF-Ziron, VB and Zr-2.5Nb, the increase of oxidation rate at the transition is not that pronounced so no similar f_H decrease is shown in the calculations, and no decrease or plateau of f_H was observed experimentally [7,21]. To directly compare the calculated H pickup fractions to the experimentally measured values at the same corrosion time and conditions, the calculated fraction f_H^{cal} vs. the experimentally measured fraction f_H^{exp} are plotted in Fig, 5.2a. The first letter in the symbol name represents different alloys and the number is the corrosion time in days. The letter with prime symbol means the sample is in tube form, otherwise it is in sheet form. Since the data points of for Zry-4, ZIRLO and Zr-2.5Nb are concentrated in the low f_H corner, that region (marked by dotted line) is magnified in Figure 5.2b. According to Figure 5.2a and 5.2b, most of the data points are relatively close to the $f_H^{cal}=f_H^{exp}$ (dashed) line, which would correspond to a perfect agreement of the modeling predictions with experimental values. Given the uncertainties in the experimental measurements and therefore in input parameters, as well as the various simplifying assumptions in the model, the agreement between the calculated H pickup fractions and the experimental values is relatively good.
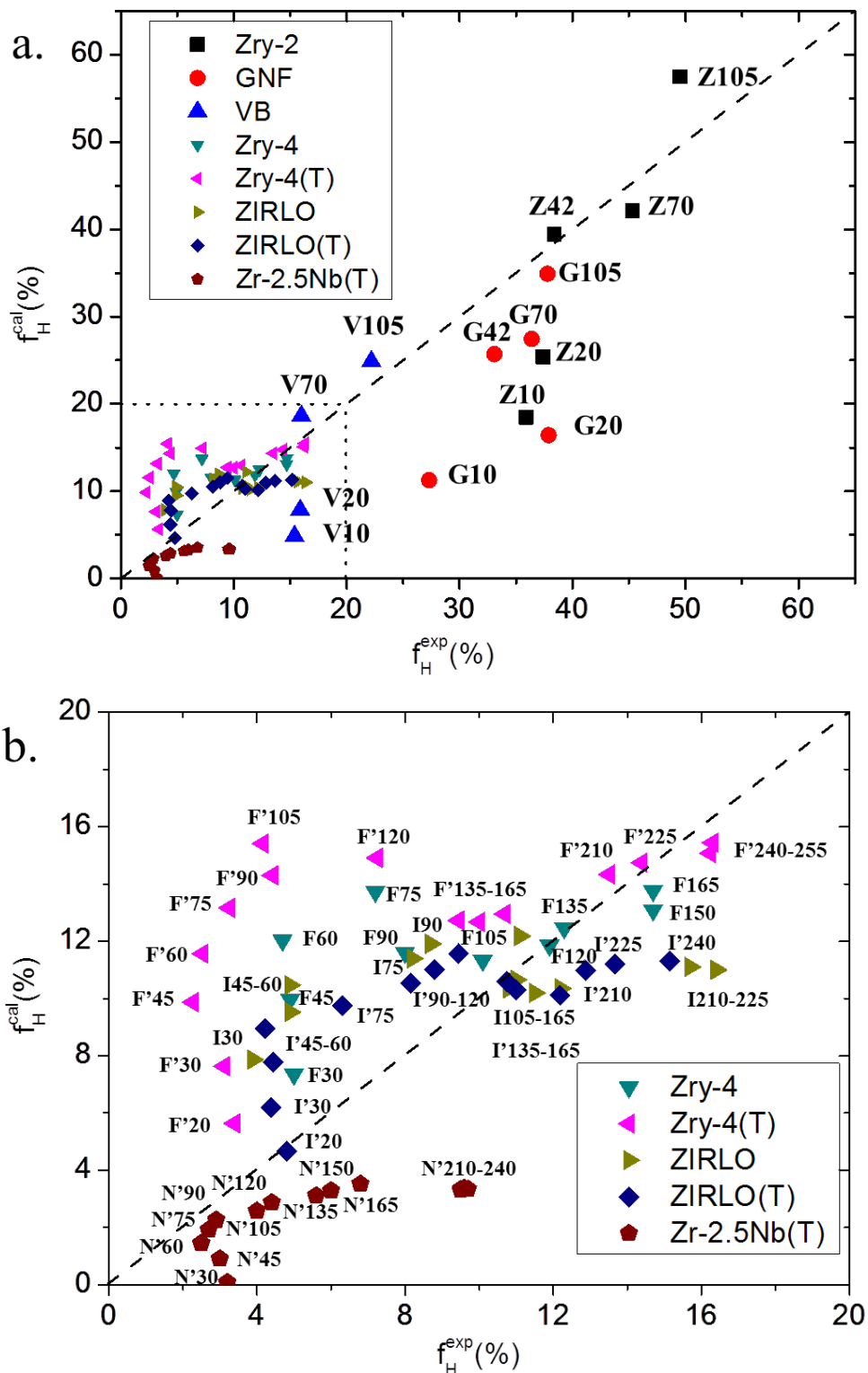
Figure 5.2 *(a) Comparison between the f_H calculated by our model and f_H measured experimentally under steam/water corrosion. For the name of each data point, the first letter represents the type of the Zr alloy and the number is the corrosion time in days. Z, G, and V*

stand for Zry-2, GNF-Ziron and VB, respectively. The dashed line indicates the condition that calculated f_H is equal to the experimentally measured f_H. (b) Magnification of the left-bottom corner of Figure 5.2a. F, I, and N stand for Zry-4, ZIRLO and Zr-2.5Nb respectively. The letter with prime symbol indicates that the sample is in tube form. The experimentally measured f_H values of Zry-2, GNF-Ziron and VB are from ref. [7] and the values of Zry-4, ZIRLO and Zr-2.5Nb are from ref. [21] .

Some of previous studies suggest that at least part of hydrogen that migrate through the oxide layer is charged [21,33], so it is necessary to consider the effect of electric filed from other charged particles on the H pick up process. To address this concern, we assumed all the migrating H is charged and calculated the maximum possible H flux due to electric filed and the compared this flux to the flux due to concentration gradient at the same time. The electric-field induced H flux can be calculated based on steady state Nernst-Planck equation shown below

$$F_{elec} = D_H \frac{C_H^{ZrO_2}(x,t)q_H E(x,t)}{k_B T} \tag{5.8}$$

Here q_H is the charge of H ion (+1 unit charge), k_B is Boltzmann constant and T is corrosion temperature. E represents the electric filed across the Zr oxide film and is calculated by the following equation

$$E = \rho j = \rho \frac{q_O N_A}{M_O} \frac{dwg(t)}{dt} \tag{5.9}$$

The ρ is the electrical resistivity of oxide (MΩ•cm) and j is the oxidation current density (A/cm^2). According to previous studies, ρ varies as oxidation goes on and different Zr oxide may show quite different values (the range is from $2 - 140$ MΩ•cm) [34,35]. In order to estimate the maximum possible influence of the electric field on the H pickup, the maximum ρ (140 MΩ•cm) among all the reported values is chosen in our calculation. The oxidation current density j is proportional to the oxidation rate. As mentioned earlier, *wg(t)* is the time-depended weight gain

of the Zr specimen measured experimentally during the corrosion. If the contribution of absorbed H to the weight gain is neglected, then *dwg(t)/dt* is the oxidation rate (in mg/dm^2•s). q_o is the electric charge of oxygen ion (+2 unit charge), N_A is Avogadro's constant and *Mo* is molar mass of oxygen ion. However, our calculation shows that the electric field contribution to the H flux is negligible compared to concentration gradient since the oxidation current density is very low. The detailed results will be discussed latter.

Based on equation (5.8) and (5.9), the time-depended electric field-introduced H fluxes, F_{elec} for all Zr alloys were calculated. Compering to the H flux from concentration gradient, F_{elec} has a negligible effect on the H pickup. As the weight gain follows the power law shown in equation (5.3) with exponent *q* less than 1, the oxidation current density *j* which is proportional to the time derivative of weight gain, decreases quickly with time. For example, *j* in Zry-4 oxide is 6.08×10^{-4} A/cm^2 at 1 mins after corrosion starts and quickly decreases to 3.48×10^{-6} A/cm^2 at 1 day and 6.80×10^{-7} A/cm^2 at 10 days. The corresponding electric field-induced H flux is 1.95×10^{11} /cm2 s at 1 min, 3.36×10^{11} /cm2 s at 1 day and 6.45×10^{10} /cm2 s at 10 days,. As comparison, the corresponding H flux from concentration gradient is 2.13×10^{2} /cm2 s at 10 min, 2.05×10^{12} /cm2 s at 1 day and 1.06×10^{12} /cm2 s at 10 days. For these calculations we are using the maximum resistivity measured during the entire oxidation process. In fact, the initial resistance for Zry-4 in the first few days are probably less than 5 MΩ•cm [35]. Therefore it is reasonable to ignore the electric effect, especially we care about the H pickup during a long time scale (in 1 day to a hundred days for the corrosion experiment).

5.4 Limitation of current model and future improvement

Although the current model can give a relatively good quantitative agreement between simulation and experiments, a careful examination of the distribution of the data points can

reveal a few systematic discrepancies between the experimental and calculated f_H. First, as shown in Figure 5.2a, for Zry-2 and VB f_H^{cal} is lower than f_H^{exp} for short corrosion times but higher than f_H^{exp} for the long corrosion times. In other words, the slopes of f_H with time are steeper in the model than in the experiments. A similar error in the slope of f_H with time can be seen in Figure 5.2a for GNF-Ziron. However, in contrast to the values for Zry-2 and VB, all the values for GNF-Ziron are generally lower in the calculation than the experiments. In fact, data for this alloy shows a very large slope in the experiments, yielding essentially the same f_H at 20 and 105 days. This trend suggests that hydrogen diffusion through the thickening oxide may not dominate H pickup in this system, or that we have not estimated the transition time correctly. Second, as shown in Figure 5.2b, the calculated H pickup fractions are somewhat higher than experimental values for most data points of Zry-4 and ZIRLO (both sheet and tube samples), whereas somewhat lower for Zr-2.5Nb. Third, current model cannot explain some time-depended features of H pickup fractions. For example, some experiments show a sudden increase in H pickup fractions right before the oxide breaks-away and certain Zr alloys show periodic features of H pickup during the cycle of oxidation, breaks-away and oxidation again [35].

Several possible reasons may contribute to all of these above discrepancies. First is the uncertainty in the measured H diffusion coefficients in various Zr alloy oxides. As summarized in Table 5.1, the D_H values adopted in our calculations is between 1.0×10^{-18} m^2/s and 1.0×10^{-19} m^2/s (at T=360 °C) under water/steam corrosion, since this range is located in the middle of the H diffusion coefficients reported in literature. A summary of H diffusion coefficient in various Zr alloy oxides can be found in the appendix table, which is adapted from Table 3 in Ref. [11] with one new H diffusion coefficient obtained recently [36]. However, as mentioned earlier, there is a wide variation in the reported D_H values even for the same Zr alloy. For example,

according to Ref. [26], $D_H = 1.81 \times 10^{-19}$ m^2/s for Zr-2.5Nb at 360 °C, whereas in Ref.[37] D_H is as large as 1.13×10^{-17} m^2/s. This large difference may be caused by the use of different techniques for measuring H concentration, details of sample preparations and methods for deriving the diffusion coefficient. It also suggests that there are large uncertainties in these experiments. If the D_H for Zr-2.5Nb is increased by a factor of five, the calculated H pickup fractions are increased about eight times, provided all the other parameters are not changed. In addition, in our model a fixed D_H is applied for calculating f_H in the entire H pickup process. This fixed D_H is usually derived by fitting the H concentration profiles measured after certain period of time using nuclear reaction analysis or secondary ion mass spectrometry [26,38,39]. Therefore the obtained D_H is actually "averaged effective" diffusivity, while the real diffusivity in different regions of the oxide barrier layer or at different times may not be necessarily the same. For example, as mentioned in the introduction, the compressive stress in the oxide decreases the H diffusivity substantially. It is possible that during the initial oxidation, the stress in the thin oxide layer is still small so that the real H diffusivity is actually larger than the effective value, which would lead to a higher H pickup rate at short corrosion times. Secondly, the calculated H pickup fraction has a relatively strong dependence on the maximum dense oxide thickness (L_{bm}). For example, decreasing the L_{bm} from 0.9 μm to 0.8 μm of GNF-Ziron would increase the pickup fraction at 105 days from 34.9% to about 39.3%. In experiment, the value of L_{bm} is estimated by analyzing H concentration profiles from nuclear reaction analysis [7,11]. The relatively low spatial accuracy of the method may introduce some errors to the thickness value. In addition, kinetic information of the dense oxide growth is not captured in this measurement and the growth of the dense oxide may not necessarily follow the same kinetics of the weight gain. Finally, due to the difficulty in measuring effective H partial pressure during the corrosion test, a

constant H partial pressure p_{H_2} is used for the f_H calculation. As the rate of corrosion reaction changes during the H pickup process, it is quite possible that p_{H_2} also varies with time.

For the sake of comparison, in Figure 5.3 we plot the calculated H pick up fraction f_H^{cal} as a function of the experimentally measured fraction f_H^{exp}, but this time for LiOH water corrosion experiments. As expected, most calculated H pickup fractions are far from the experimental values, which demonstrates that when diffusion through the dense oxide is not a rate limiting process, our model does not predict accurate f_H values. The failure of the model when applied to the LiOH systems (where other physical phenomena are expected to affect H transport) supports the assertion that the model captures real physics when it successfully matches experimental data in the steam/water corroded materials. In addition, the success of the model for the steam/water corroded systems further supports the notion that the dense oxide plays a dominant role in controlling f_H in those measurements.
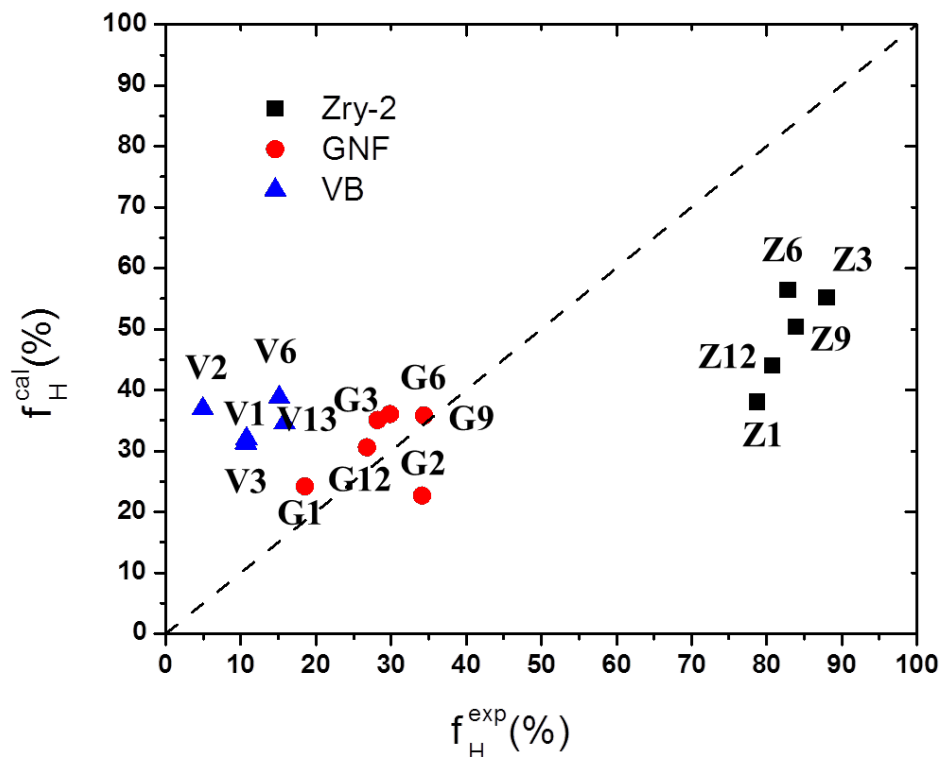
Figure 5.3 *Comparison between the f_H calculated by our model and f_H measured experimentally in 290 °C LiOH water. For the name of each data point, the first letter represents the type of the Zr alloy and the number is the corrosion time in days. The dashed line indicates the condition where the calculated f_H is equal to the experimentally measured f_H.*

5.5 Conclusions

A continuum model for calculating the time-dependent H pickup fractions in different Zr alloys has been developed in this chapter. To the best of our knowledge, all available experimental data that simultaneously measures time-depended H pickup fractions and weight gain for Zr alloys of available H diffusivities in Zr oxide have been collected and compared with the H pickup fractions calculated using our model. It has been shown that the model's predictions match qualitatively with the experimental values of steam and water corrosion, which supports the hypothesis that hydrogen diffusion through the dense oxide barrier layer is the rate-limiting process for H pickup. It is also shown that the model breaks down when attempting to predict f_H in LiOH containing water corrosion, providing further evidence for the absence of dense oxide in the LiOH environment and supporting the model through demonstrating that it fails when expected. This model offers a starting framework for developing more sophisticated models in the future when more accurate parameters (e.g., H diffusivity and solubility, oxide barrier layer thickness, and H_2 partial pressure) are available, and for incorporating more factors that may play an important role in H transport (such as water dissociation on oxide surface).

Appendix

Appendix table 5.1 *Summary of H diffusion coefficient in oxide of different Zr alloys*
(NRA is nuclear reaction analysis, GRA is gas release analysis and SIMS is second ion mass
spectroscopy analysis)

Zr alloy	Diffusion prefactor (m^2/s)	Activation Energy (kJ/mol)	Investigator	Method
Zry-2	2.76×10^{-9}	114.84	Khatamian [23]	NRA
Zry-2	1.30×10^{-13}	81.1	Kunz [40]	GRA
Zry-2	4.00×10^{-17}	30.1	Austin [41]	GRA
GNF-Ziron	4.50×10^{-17}	17	Takagi [11]	NRA
VB	8.9×10^{-19} at 673K	-	Une [7]	NRA
Zry-4	2×10^{-21} (300K); 6×10^{-19} (673K)	-	Hatano [24]	SIMS
Zr-2.5 Nb	8.09×10^{-18}	20	McIntyre [26]	SIMS
Zr-2.5 Nb	3.05×10^{-13}	53.7	Khatamian [39]	NRA
Zr-2.5 Nb	1.15×10^{-10}	71.6	Khatamian [37]	NRA
Zr-2.5Nb	2.7×10^{-19} (523K); 6.5×10^{-19} (573K)	-	Une [36]	NRA
Zr-2.5Nb	1×10^{-18} (573 K)	-	Elmoselhi [26]	SIMS
Zr-20Nb	2.60×10^{-6}	149.92	Khatamian [23]	NRA
Zr-20Nb	1.64×10^{-8}	118.7	Urbanic [42]	NRA
Zr-15Nb	1.99×10^{-10}	89.46	Khatamian [23]	NRA
Zr	1.13×10^{-12}	81.1	Khatamian [39]	NRA

Bibliography

[1]   Videm K. Nucl Eng Des 1972;21:200.

[2]   Motta AT, Chen LQ. Jom 2012;64:1403.

[3]   Zinkle SJ, Was GS. Acta Mater 2013;61:735.

[4]   Cox B. Adv Corros Sci Technol 1976:173.

[5]   Veshchunov MS, Berdyshev AV. J Nucl Mater 1998;255:250.

[6]   Grosse M, Steinbrueck M, Lehmann E, Vontobel P. Oxid Met 2008;70:149.

[7]   Une K, Sakamoto K, Aomi M, Matsunaga J, Etoh Y, Takagi I, Miyamura S, Kobayashi T, Ito K, Barberis P, Dean SW. Hydrogen Absorption Mechanism of Zirconium Alloys Based on Characterization of Oxide Layer, in:. Zircon. Nucl. Ind. 16th Int. Symp. ASTM STP 1529, vol. 8. 2011.

[8]   Cox B. J Nucl Mater 2005;336:331.

[9]   Ni N, Hudson D, Wei J, Wang P, Lozano-Perez S, Smith GDW, Sykes JM, Yardley SS, Moore KL, Lyon S, Cottis R, Preuss M, Grovenor CRM. Acta Mater 2012;60:7132.

[10]   Glazoff M V., Tokuhiro A, Rashkeev SN, Sabharwall P. J Nucl Mater 2014;444:65.

[11]   Takagi I, Une K, Miyamura S, Kobayashi T. J Nucl Mater 2011;419:339.

[12]   Muta H, Etoh Y, Ohishi Y, Kurosaki K, Yamanaka S. J Nucl Sci Technol 2012;49:544.

[13]   Yao MY, Zhou BX, Li Q, Liu WQ, Chu YL. J Nucl Mater 2006;350:195.

[14]   Cox B. J Nucl Mater 1999;264:283.

[15]   Hatano Y, Isobe K, Hitaka R, Sugisaki M. J Nucl Sci Technol 1996;33:944.

[16]   Wang X, Khafizov M, Szlufarska I. J Nucl Mater 2014;445:1.

[17]   Bai X-M, Zhang Y, Tonks MR. Phys Chem Chem Phys 2013;15:19438.

[18]   Cox B, Wong Y-M. J Nucl Mater 1999;270:134.

[19]   Garzarolli F, Cox B, Rudling P, Barberis P, Dean SW. Optimization of Zry-2 for High
       Burnups, in:. Zircon. Nucl. Ind. 16th Int. Symp. ASTM STP 1529, vol. 7. 2011.

[20]   Ni N, Lozano-Perez S, Jenkins ML, English C, Smith GDW, Sykes JM, Grovenor CRM.
       Scr Mater 2010;62:564.

[21]   Couet A, Motta AT, Comstock RJ. J Nucl Mater 2014;451:1.

[22]   Müller S, Lanzani L. J Nucl Mater 2013;439:251.

[23]   Khatamian D. J Alloys Compd 1997;253-254:471.

[24]   Hatano Y, Hitaka R, Sugisaki M, Hayashi M. J Radioanal Nucl Chem 1999;239:445.

[25]   Une K, Takagi I, Sawada K, Miyamura S, Aomi M. Prog Nucl Energy 2012;57:93.

[26]   McIntyre NS, Davidson RD, Weisener CG, Warr BD, Elmoselhi MB. Surf Interface Anal
       1991;17:757.

[27]   Motta AT, Gomes da Silva MJ, Yilmazbayhan A, Comstock RJ, Cai Z, Lai B, Limback
       M, Kammenzind B, Dean SW. Microstructural Characterization of Oxides Formed on
       Model Zr Alloys Using Synchrotron Radiation, in:. Zircon. Nucl. Ind. 15th Int. Symp.
       ASTM STP 1505, vol. 5. ASTM International; 2009.

[28]   Porte HA, Schnizlein JG, Vogel RC, Fischer DF. J Electrochem Soc 1960;107:506.

[29]   Vermaak N, Parry G, Estevez R, Bréchet Y. Acta Mater 2013;61:4374.

[30]   de Gabory B, Motta AT, Wang K. J Nucl Mater 2015;456:272.

[31]   Yilmazbayhan A, Motta AT, Comstock RJ, Sabol GP, Lai B, Cai Z. J Nucl Mater 2004;324:6.

[32]   Park K, Olander DR. J Am Ceram Soc 1991;74:72.

[33]   K. Baur, Garzarolli F, Ruhmann H, Sell H-J. Zircon Nucl Ind Twelfth Int Symp 2000:836.

[34]   Schefold J, Lincot D, Ambard A, Kerrec O. J Electrochem Soc 2003;150:B451.

[35]   Couet A. Hydrogen Pickup Mechanism of Zirconium Alloys. The Pennsylvania State University, 2014.

[36]   Une K, Sakamoto K, Takagi I, Sawada K, Watanabe H, Aomi M. J Nucl Mater 2013;439:84.

[37]   Khatamian D. Zeitschrift für Phys Chemie 1993;181:435.

[38]   Grosse M, van den Berg M, Goulet C, Lehmann E, Schillinger B. Nucl Instruments Methods Phys Res Sect A Accel Spectrometers, Detect Assoc Equip 2011;651:253.

[39]   Khatamian D, Manchester FD. J Nucl Mater 1989;166:300.

[40]   Kunz W, Münzel H, Kunz U, Therefore GU. J Nucl Mater 1985;136:6.

[41]   Austin JH, Elleman TS. J Nucl Mater 1974;51:321.

[42]   Urbanic VF, Chan PK, Khatamian D, Woo OTT. Growth and Characterization of Oxide Films on Zirconium-Niobium Alloys, in:. Zircon. Nucl. Ind. 10th Int. Symp. STP 1245, vol. 1245. 1994.

6. Summary and future work

In this thesis, I have combined both advanced transmission electron microscopy and multiscale materials simulation to investigate the effects of interfaces on the degradation process of nuclear cladding materials. Two important aspects of the cladding materials degradation, i.e. radiation-induced degradation and corrosion-induced degradation are covered in this study separately in model materials. In silicon carbide (SiC), the effects of grain boundaries (GB) on the radiation-induced amorphization at low irradiation temperature and the radiation-induced segregation at elevated temperature have been investigated. In zirconium (Zr) and Zr alloys, the initial oxidation process at the metal surface and hydrogen pickup process through the water/oxide/metal interface has been studied. Our studies show that the cross validation between the advanced microscopy and multiscale simulations is an invaluable tool to understand the defect-interface interactions starting from atomic level.

Evolution of amorphous domains in SiC with 1 MeV Kr^{2+} irradiation is investigated using high-resolution transmission electron microscopy and simulations. An unusual morphology of highly curved crystalline/amorphous boundaries is observed in the images, which is identified as a result of cascade overlap and reproduced by a coarse-grained model informed by atomistic simulations. The comparison between local amorphization fractions near GB and within grain interiors provides experimental evidence for the interstitial starvation mechanism in SiC for the first time. As a competing effect to defect sinks, interstitial starvation increases the rate of local amorphization near GB and reduces the radiation resistance of nanocrystalline silicon carbide. One interesting question that has not been addressed is the time evolution of the crystalline/amorphous phase boundaries at different irradiation doses, since only one sample with 50% does to amorphization has been analyzed in this thesis. The morphologies of amorphous

domains in more samples with different amorphization fractions can be analyzed using HRTEM and compared to the predictions of the course-grained model. This comparison could provide important clues to understand the kinetics during the entire radiation-induced amorphization process. Another interesting topic is to observe the initial stage of amorphization process using *in situ* HRTEM, which may provide an access to direct observing the process of lattice distortion, defect accumulation and crystalline-amorphous transition.

The relative C composition profiles near GB in both C^{2+} irradiated chemical vapor deposited (CVD) SiC and non-irradiated CVD SiC are measured using electron energy loss spectroscopy (EELS). The relative C composition at GB has been found intrinsically lower than 50% in CVD SiC and the minimum C concentration is around 46%. This non-stoichiometric GB may help explain the phenomenon that GB in CVD SiC is preferentially dissolved in supercritical water. The EELS analyses in irradiated samples show that GB experiences a C enrichment at low irradiation temperature (300 °C) and a C depletion at high irradiation temperature (600 °C). According to the rate theory calculations, GB plays different roles at different temperature. When the irradiation temperature is low and the diffusion of C interstitials along GB is slow, GB act as defect sinks of the net C interstitial flux and C concentration at GB increases from 46% (in the non-irradiated sample) to about 50% at 300 °C after 1 dpa irradiation. However, when the irradiation temperature is high enough and the C interstitials at GB get mobile, GB becomes a channel for C defects to diffuse to stronger sinks on the ends of GB like triple junctions or surfaces. The evolutions of C concentration profile near GB at different irradiation condition (such as temperature, dose) are the results of a series of synergetic defect migration and reaction processes happening both in the grain interiors and at GB. It is worth noting that current studies only use SiC samples irradiated with ions. However in the reactor

condition, the irradiation particles are mostly neutrons, which have zero charge and relatively lower dose rate compared to ion irradiation. It is helpful to analyze the C composition profiles near GB in neutron irradiated samples (at similar dose and temperature) to test whether the irradiation species and dose rate can play important roles during the segregation process.

Effect of surface strain on oxygen adsorption on Zr (0001) surface is investigated by density functional theory (DFT) calculations. It is demonstrated that both surface strain and interactions between oxygen adsorbates influence the adsorption process. Oxygen binding to zirconium becomes stronger as the strain changes from compressive to tensile. When oxygen coverage is low and the oxygen interactions are negligible, surface face-centered cubic site is the most stable site for O adsorbates. At high coverage and under compression, octahedral site between second and third Zr layers becomes most favorable because positive charge screening weakens the interactions between O adsorbates. Calculations with both single-layer adsorption model and multiple-layer adsorption model demonstrate that compressive strain at the Zr/oxide interface will provide a thermodynamic driving force for oxygen to incorporate from the surface into the bulk of Zr, while binding oxygen to Zr surface will be easier when tensile strain is applied.

A continuum model for calculating the time-dependent hydrogen pickup fractions in Zr alloys under steam and pressured water conditions has been developed in this thesis. Using only one fitting parameter, the hydrogen gas partial pressure at the oxide surface, a relatively good agreement is obtained between the predicted and previously measured hydrogen pickup fractions. The results support the hypothesis that hydrogen diffusion through the barrier oxide layer is the rate-limiting step for H pickup. Due to the lack of accurate models for oxidation kinetics right before the oxide "breakaway" and during the periodic oxidation process in the long

term, our H pickup model cannot accurately predict the instantaneous increase of H pickup fractions right before the oxide "breakaway" and the periodic features of H pickup fractions across different oxidation periods. In addition, other mechanisms that may affect the H pickup process (e.g. H reaction at oxide surface, pores and cracks formation and surface strain) are not included. However, the model developed in this thesis provides a baseline and more complicated effects can be incorporated in future studies.